

This dissertation is submitted to Charles Sturt University for the Bachelor of
Science (Honours)

Relations between the quantum eigenvalue m , binding energy, central mass and
the transition rates of charged particles held in gravitational eigenstates in non-
relativistic regions of deep gravitational wells.

Mitchell Bonham. Student Number: 11585035

Prior qualifications:

Bachelor of Science, Charles Sturt University, 2019.

Bachelor of Applied Science (Physiotherapy), University of Sydney, 2007.

Dissertation submitted: October 2020

Contents

Statement of authorship & readiness for examination	10
Acknowledgements:	11
Statement of ethics approval:	12
Journal identification and rationale:.....	13
Paper 1: Relations between the quantum eigenvalue m and transition rates of charged particles held in gravitational eigenstates in non-relativistic regions of deep gravitational wells	15
1.1) Abstract	15
1.2) Introduction:.....	16
1.3) Methods:	18
1.3.1) Mathematical theory – Formulation of a Schrödinger Equation for weak gravity:	18
1.3.2) Avoiding relativistic regions of gravity around the central mass M :.....	20
1.3.3) Mathematical Theory – State to state transition probability:.....	21
1.3.4) Mathematical Theory – State lifetimes:.....	22
1.3.5) State to state transition rates as a function of Δm and m_i :.....	23
1.3.6) State to state transition rates as a function of p_i for all Δm decay channels:	23
1.3.7) State lifetimes:	24
1.4) Results:.....	24
1.4.1) Results for state to state transition rates as a function of Δm and m_i :	24
1.4.2) Results for state to state transition rates as a function of p_i for all Δm decay channels:.....	38
1.4.3) Results for state lifetimes:	52
1.5) Discussion:	56
1.5.1) Implications:	60
1.6) References.....	61
Paper 2: Relations between binding energy, central mass and transition rates of charged particles held in gravitational eigenstates in non-relativistic regions of deep gravitational wells.	64
2.1) Abstract:.....	64
2.2) Introduction:	65
2.3) Methods:	69
2.3.1) Mathematical theory –Schrödinger Equation for weak gravity:.....	69
2.3.2) Mathematical Theory – State to state transition rate:	71
2.3.3) State to state transition rate as a function of central mass:	72
2.3.4) Avoiding relativistic regions of gravity around the central mass M :.....	73
2.4) Results:	74
2.5) Discussion:.....	89

2.5.1) Conclusion:.....	93
2.6) References.....	94
Appendix A: Guidelines for Authors of Gravitation and Cosmology	97
Appendix B: Extended Literature review.....	99
B.1 – Introduction and background:	99
B.1.1 – The Λ CDM cosmological model:	99
B.2 – Current observational evidence suggesting the existence of DM:	100
B2.1 – Rotation curves of galaxies:	100
B2.2 – Gravitational lensing:	101
B2.2.1 – Strong lensing:	101
B2.2.2 – Weak lensing:.....	102
B2.2.3 – Microlensing:	102
B2.3 – Galaxy and cluster collisions:.....	103
B2.4 – Cosmic microwave background (CMB) and the Lyman-alpha forest constrain parameters of Λ CDM:	103
2.5 – Predicted structure of the universe from Λ CDM N-body simulations:	104
B3 – Dark matter particle candidates:.....	105
B3.1 – The neutrino and the sterile neutrino:.....	105
B3.2 – Massive astrophysical compact halo objects (MACHOs):.....	106
3.3 – Primordial black holes (PBHs):	106
B3.4 – Weakly interacting massive particles (WIMPs):.....	106
B3.4.1 – Experimental attempts to find WIMPs:	107
B3.5 – Super heavy particles:	108
B4 – Challenges to Λ CDM:	108
B4.1 – Proposed solutions to issues with Λ CDM:.....	109
B5 – Alternative theories of gravity. Modified Newtonian Dynamics Model (MOND) and its relativistic extension, Tensor-Vector-Scalar gravity (TeVeS):.....	109
B6 – The quantum dark matter (QDM) hypothesis:	111
B6.1 – Experimental proof of gravitational eigenstates:.....	111
B6.2 – Foundations of QDM mathematical theory:.....	112
B6.3 – The radial equation and its general solution:.....	112
B6.4 – General and approximate solutions for state to state transition categories in figure 2.1 .	113
B6.4.1 – Transition category $B \rightarrow A$:	113
B6.4.2 – Transition category $C \rightarrow A$:	114
B6.3.3 – Transition category $D \rightarrow A$:	114
B6.5 – The effect of the radial eigenfunction components of the overlap integral on eigenstructure shape:.....	116

B6.6 – Overlap integral values and the zeros of the radial eigenfunctions:	118
B6.7 – The effect of the angular components of the overlap integral on eigenfunction shape: ..	119
B6.8 – Physical properties of gravitational eigenstates and QDM:	120
B6.9 – Speculated formation of the DM halo and Big Bang Nucleosynthesis (BBN):	122
B6.10 – Observations which support or refute the QDM hypothesis:	123
B6.11 – Identified gaps in the theoretical framework for QDM:	124
B7 – Conclusion:	124
Appendix C: Extended Methods for paper 1	126
C1 – Additional justification of choice of methods and data analysis:	126
C2 – Development of computer programs:	126
C3 – Exact values and computer programs/packages used for each state to state transition rate calculated in section 1.4.1:	127
C3.1 – State to State Decay Rates for $\Delta p = -5$:	127
C3.2 – State to State Decay Rates for $\Delta p = -2$:	128
C3.3 – State to State Decay Rates for $\Delta p = 0$:	130
C4 – Exact values and computer programs/packages used for each state to state transition rate calculated in section 1.4.2:	130
C4.1 – State to State Decay Rates for $\Delta p = -2$:	131
C4.2 – State to State Decay Rates for $\Delta p = -1$:	131
C4.3 – State to State Decay Rates for $\Delta p = 0$:	132
C5 – Computer programs used for the evaluation of state lifetimes in section 1.3.7:	132
Appendix D: Extended Methods for paper 2	133
D1 – Additional justification of choice of methods and data analysis:	133
D2 – Development of computer programs:	133
D3 – Exact values and computer programs/packages used for each state to state transition rate calculated in section 2.3.3:	133
D3.1 – State to State Decay Rates for $p_i = 3$:	134
D3.2 – State to State Decay Rates for $p_i = 10$:	136
D3.3 – State to State Decay Rates for $p_i = 25$:	138
D3.4 – State to State Decay Rates for $p_i = 50$:	140
D3.5 – State to State Decay Rates for $p_i = 75$:	142
D3.6 – State to State Decay Rates for $p_i = 100$:	144
Appendix E: Newtonian (Mathematica Package)	147
Appendix F: Mathematica program for methods in section 1.3.6	152
Appendix G: Mathematica program for methods in section 1.3.5	154
Appendix H: Mathematica program for methods in section 1.3.7	156
Appendix I: NewtonianModified (Mathematica package)	158

Appendix J: Mathematica program for methods in section 2.3.3	162
Appendix K: Examples of python code used for data analysis	165
K1 – Importation of data from text file.....	165
K2 – Sample code for results in section 1.4.1	167
K3 – Sample code for results in section 1.4.2.....	169
K4 – Sample code for results in section 1.4.3.....	172
K5 – Sample code for results in section 2.4.....	173
K5.1 – Sample code for state to state transition rate as a function of central mass	173
K5.2 – Sample code for gradients as a function of p_i	176
Appendix L: References included in sections outside of paper 1 and paper 2	179

Table of figures

Fig. 1.4.1. State to state transitions rate $A_{i,f}$ as a function of $l_i - m_i$ and Δm for $n_i = 150$, $p_i = 6$, $\Delta p = -2$ and $l_i = 144$. (a) $\Delta l = 1$. (b) $\Delta l = -1$.	25
Fig. 1.4.2. State to state transitions rates $A_{i,f}$ as a function of $q_i (\equiv l_i - m_i)$ and Δm for $n_i = 150$, $p_i = 6$, $\Delta p = 0$, $l_i = 144$ and $\Delta l = -1$.	27
Fig. 1.4.3. State to state transitions rates $A_{i,f}$ as a function of $q_i (\equiv l_i - m_i)$ and Δm for $n_i = 150$, $p_i = 6$, $\Delta p = -2$, $l_i = 144$ and $\Delta l = -1$.	28
Fig. 1.4.4. State to state transitions rates $A_{i,f}$ as a function of $q_i (\equiv l_i - m_i)$ and Δm for $n_i = 150$, $p_i = 6$, $\Delta p = -2$, $l_i = 144$ and $\Delta l = 1$.	29
Fig. 1.4.5. State to state transitions rates $A_{i,f}$ as a function of $q_i (\equiv l_i - m_i)$ and Δm for $n_i = 150$, $p_i = 6$, $\Delta p = -5$, $l_i = 144$ and $\Delta l = -1$.	29
Fig. 1.4.6. State to state transitions rates $A_{i,f}$ as a function of $q_i (\equiv l_i - m_i)$ and Δm for $n_i = 150$, $p_i = 6$, $\Delta p = -5$, $l_i = 144$ and $\Delta l = 1$.	30
Fig. 1.4.7. State to state transitions rates $A_{i,f}$ as a function of $q_i (\equiv l_i - m_i)$ and Δm for $n_i = 150$, $p_i = 120$, $\Delta p = 0$, $l_i = 30$ and $\Delta l = -1$.	31
Fig. 1.4.8. State to state transitions rates $A_{i,f}$ as a function of $q_i (\equiv l_i - m_i)$ and Δm for $n_i = 150$, $p_i = 120$, $\Delta p = -2$, $l_i = 30$ and $\Delta l = -1$.	31
Fig. 1.4.9. State to state transitions rates $A_{i,f}$ as a function of $l_i - m_i$ and Δm for $n_i = 150$, $p_i = 120$, $\Delta p = -2$, $l_i = 30$ and $\Delta l = 1$.	32
Fig. 1.4.10. State to state transitions rates $A_{i,f}$ as a function of $l_i - m_i$ and Δm for $n_i = 150$, $p_i = 120$, $\Delta p = -5$, $l_i = 30$ and $\Delta l = -1$.	32
Fig. 1.4.11. State to state transitions rates $A_{i,f}$ as a function of $l_i - m_i$ and Δm for $n_i = 150$, $p_i = 120$, $\Delta p = -5$, $l_i = 30$ and $\Delta l = 1$.	33
Fig. 1.4.12. Percentage error in estimating the sum of the state to state transition rates of all Δm decay channels by using the state to state transition rate for the $\Delta m = 0$ decay channel multiplied by three, plotted as a function of m_i / l_i .	37
Fig. 1.4.13. State to state transitions rates $A_{i,f}$ as a function of p_i with $n = 5, 10, 15, \dots, 100$ for $m_i = 0$, $\Delta p = 0$, $\Delta m = 0$ and $\Delta l = -1$.	38
Fig. 1.4.14. State to state transitions rates $A_{i,f}$ as a function of initial p_i for $n = 5, 10, 15, \dots, 100$ for $m_i = 0$, $\Delta p = 0$, $\Delta m = \pm 1$ and $\Delta l = -1$.	39
Fig. 1.4.15. Overestimation in state to state transition rates $A_{i,f}$ through using $\Delta m = 0$ to approximate the case where $\Delta m = \pm 1$ for $n = 5, 10, 15, \dots, 100$, $\Delta l = -1$ and $\Delta p = 0$.	40
Fig. 1.4.16. State to state transition rates $A_{i,f}$ for $\Delta m = 0$ expressed as a percentage of state to state transition rates $A_{i,f}$ for $\Delta m = \pm 1$ where $n = 5, 10, 15, \dots, 100$, $\Delta l = -1$ and $\Delta p = 0$.	41
Fig. 1.4.17. State to state transitions rates $A_{i,f}$ as a function of p_i with $n = 5, 10, 15, \dots, 100$ for $m_i = 0$, $\Delta p = -1$, $\Delta m = 0$ and $\Delta l = -1$.	42
Fig. 1.4.18. State to state transitions rates $A_{i,f}$ as a function of p_i with $n = 5, 10, 15, \dots, 100$ for $m_i = 0$, $\Delta p = -1$, $\Delta m = \pm 1$ and $\Delta l = -1$.	43
Fig. 1.4.19. Overestimation in state to state transition rates $A_{i,f}$ through using $\Delta m = 0$ to approximate the case where $\Delta m = \pm 1$ for $n = 5, 10, 15, \dots, 100$, $\Delta l = -1$ and $\Delta p = -1$.	44
Fig. 1.4.20. State to state transition rates $A_{i,f}$ for $\Delta m = 0$ expressed as a percentage of state to state transition rates $A_{i,f}$ for $\Delta m = \pm 1$ where $n = 5, 10, 15, \dots, 100$, $\Delta l = -1$ and $\Delta p = -1$.	45
Fig. 1.4.21. State to state transitions rates $A_{i,f}$ as a function of p_i with $n = 5, 10, 15, \dots, 100$ for $m_i = 0$, $\Delta p = -2$, $\Delta m = 0$ and $\Delta l = -1$.	46
Fig. 1.4.22. State to state transitions rates $A_{i,f}$ as a function of p_i with $n = 5, 10, 15, \dots, 100$ for $m_i = 0$, $\Delta p = -2$, $\Delta m = \pm 1$ and $\Delta l = -1$.	47

Fig. 1.4.23. Overestimation in state to state transition rates $A_{i,f}$ through using $\Delta m = 0$ to approximate the case where $\Delta m = \pm 1$ for $n = 5, 10, 15, \dots, 100$, $\Delta l = -1$ and $\Delta p = -1$	48
Fig. 1.4.24. State to state transition rates $A_{i,f}$ for $\Delta m = 0$ expressed as a percentage of state to state transition rates $A_{i,f}$ for $\Delta m = \pm 1$ where $n = 5, 10, 15, \dots, 100$, $\Delta l = -1$ and $\Delta p = -1$	48
Fig. 1.4.25. State to state transitions rates $A_{i,f}$ as a function of p_i with $n = 5, 10, 15, \dots, 100$ for $m_i = 0$, $\Delta p = -2$, $\Delta m = 0$ and $\Delta l = 1$	49
Fig. 1.4.26. State to state transitions rates $A_{i,f}$ as a function of p_i with $n = 5, 10, 15, \dots, 100$ for $m_i = 0$, $\Delta p = -2$, $\Delta m = \pm 1$ and $\Delta l = 1$	50
Fig. 1.4.27. Overestimation in state to state transition rates $A_{i,f}$ through using $\Delta m = 0$ to approximate the case where $\Delta m = \pm 1$ for $n = 5, 10, 15, \dots, 100$, $\Delta l = 1$ and $\Delta p = -2$	51
Fig. 1.4.28. State to state transition rates $A_{i,f}$ for $\Delta m = 0$ expressed as a percentage of state to state transition rates $A_{i,f}$ for $\Delta m = \pm 1$ where $n = 5, 10, 15, \dots, 100$, $\Delta l = 1$ and $\Delta p = -2$	52
Fig. 1.4.29. State lifetimes for $n = 15, 20, 25, \dots, 100$ as a function of p . (a) Lifetimes estimated by only using the $\Delta m = 0$ decay channel. (b) Lifetimes found by considering all Δm decay channels.	53
Fig. 1.4.30. Scatter plot of estimated state lifetime (using $\Delta m = 0$ decay channel) as a percentage of actual state lifetime, plotted as a function of l	54
Fig. 1.4.31. Log-log plot of state lifetimes for $n = 15, 20, 25, \dots, 100$ as a function of l . (a) Lifetimes estimated by only using the $\Delta m = 0$ decay channel. (b) Lifetimes found by considering all Δm decay channels.	55
Fig. 2.1. Schematic representing the high n -, l -, m -valued stationary states, drawn to emphasize the parameter $p \equiv n - l$. Each solid circle on the diagram represents $2l + 1$ z-projection substates (Ernest, 2009a, p. 4).	67
Fig. 2.2. Log-log plot of state to state transition rate $A_{i,f}$ as a function of central mass with $\Delta p = 0$, $\Delta l = -1$ and $\Delta m = 0$. (a) State binding energy is -172 eV for $p_i = 3, 10, 25, 50, 75$ and 100. (b) State binding energy is -344 eV for $p_i = 3, 10, 50$ and 100.	74
Fig. 2.3. Log-log plot of state to state transition rate $A_{i,f}$ as a function of central mass with $\Delta p = -1$, $\Delta l = -1$ and $\Delta m = 0$. (a) State binding energy is -172 eV for $p_i = 3, 10, 25, 50, 75$ and 100. (b) State binding energy is -344 eV for $p_i = 3, 10, 50$, and 100.	76
Fig. 2.4. Log-log plot of state to state transition rate $A_{i,f}$ as a function of central mass for $\Delta p = -2$, $\Delta l = 1$ and $\Delta m = 0$. (a) State binding energy is -172 eV for $p_i = 3, 10, 25, 50, 75$ and 100. (b) State binding energy is -344 eV for $p_i = 3, 10, 50$, and 100.	77
Fig. 2.5. Log-log plot of state to state transition rate $A_{i,f}$ as a function of central mass for $\Delta p = -2$, $\Delta l = -1$ and $\Delta m = 0$. (a) State binding energy is -172 eV for $p_i = 3, 10, 25, 50, 75$ and 100. (b) State binding energy is -344 eV for $p_i = 3, 10, 50$, and 100.	78
Fig. 2.6. Log-log plot of state to state transition rate $A_{i,f}$ as a function of central mass for $p_i = 10, 25, 50, 75$ and 100. Here the binding energy is -172 eV with $\Delta p = -3$ and $\Delta m = 0$. (a) $\Delta l = 1$. (b) $\Delta l = -1$... 79	79
Fig. 2.7. Log-log plot of state to state transition rate $A_{i,f}$ as a function of central mass for $p_i = 10, 25, 50, 75$ and 100. Here the binding energy is -172 eV with $\Delta p = -4$ and $\Delta m = 0$. (a) $\Delta l = 1$. (b) $\Delta l = -1$... 80	80
Fig. 2.8. Log-log plot of state to state transition rate $A_{i,f}$ as a function of central mass for $p_i = 10, 25, 50, 75$ and 100. Here the binding energy is -172 eV with $\Delta p = -5$ and $\Delta m = 0$. (a) $\Delta l = 1$. (b) $\Delta l = -1$... 81	81
Fig. 2.9. Log-log plot of state to state transition rate $A_{i,f}$ as a function of central mass for binding energy of -172 eV, $p_i = 3$, $m_i = 0$ and $\Delta m = -1, 0, 1$. (a) $\Delta p = 0$, $\Delta l = -1$. (b) $\Delta p = -1$, $\Delta l = -1$. (c) $\Delta p = -2$, $\Delta l = 1$. (d) $\Delta p = -2$, $\Delta l = -1$	83
Fig. 2.10. Gradient of the log-log relationship between state to state transition rate and central mass, plotted as a function of central mass with $\Delta l = -1$. (a) Binding energy of -172 eV, $\Delta p = 0$. (b) Binding energy of -344 eV, $\Delta p = 0$. (c) Binding energy of -172 eV, $\Delta p = -1$. (d) Binding energy of -344 eV, $\Delta p = -1$. (e) Binding energy of -172 eV, $\Delta p = -2$. (f) Binding energy of -172 eV, $\Delta p = -2$	84

- Fig. 2.11. Gradient of the log-log relationship between state to state transition rate and central mass, plotted as a function of central mass for binding energy of -172 eV with $\Delta l = -1$. (a) $\Delta p = -3$. (b) $\Delta p = -4$ (c) $\Delta p = -5$ 85
- Fig. 2.12. Gradient of the log-log relationship between state to state transition rate and central mass, plotted as a function of central mass with $\Delta l = 1$. (a) Binding energy of -172 eV, $\Delta p = -2$. (b) Binding energy of -344 eV, $\Delta p = -2$. (c) Binding energy of -172 eV, $\Delta p = -3$. (d) Binding energy of -172 eV, $\Delta p = -4$. (e) Binding energy of -172 eV, $\Delta p = -5$ 87
- Fig. 2.13. Gradient of the log-log relationship between state to state transition rate and central mass, plotted as a function of central mass for binding energy -172 eV, $\Delta m = 0$ or ± 1 and $p_i = 3$. (a) $\Delta p = -0$, $\Delta l = -1$. (b) $\Delta p = -1$, $\Delta l = -1$ (c) $\Delta p = -2$, $\Delta l = 1$. (d) $\Delta p = -2$, $\Delta l = -1$ 88

List of Tables

Table 1.4.1:.....	34
Table 1.4.2:.....	36

Statement of authorship & readiness for examination

I, the student, hereby declare that this submission is my own work and that, to the best of my knowledge and belief, it contains no material previously published or written by another person nor material which to a substantial extent has been accepted for the award of any other degree or diploma at Charles Sturt University or any other educational institution, except where due acknowledgment is made in the thesis.

Any contribution made to the research by colleagues with whom I have worked at Charles Sturt University or elsewhere during my candidature is fully acknowledged.

I, the student, confirm that my principal supervisor agrees that this dissertation is ready for examination.

Student's name: Mitchell James Bonham

Date: 15/10/2020

Acknowledgements:

I would like to acknowledge and extend my deepest gratitude to my principal supervisor Dr Matthew Collins and my co-supervisor Dr Allan Ernest. Allan has been extremely generous with his time and was always available to help whenever I was confused or lost in the research process. Allan's patient guidance has been instrumental to my understanding of the complex theory of Quantum Dark Matter. Matthew has provided sound oversight in the production of this dissertation and I have been most appreciative of his ability to guide hard decisions which naturally arise during research. Matthew and Allan complemented each other with their personal knowledge, ideas, and intuitions. I am truly thankful for the time both have invested in supervising me and I will miss my regular meetings with them.

I would also like to acknowledge the help provided by fellow student Timothy Heap who assisted in ensuring the unique data output from Mathematica was properly imported to Python for analysis.

The academic scholarship provided by Charles Sturt University has been a blessing. It has allowed me to study fulltime despite financial commitments implicit in having a young family and during the mayhem of the COVID-19 pandemic. I am grateful for Charles Sturt University's progressive and flexible approach to study, without which I would have been unable to pursue my career change ambitions.

Statement of ethics approval:

No ethics was required in the production of this research as it did not involve any human or animal participants.

Journal identification and rationale:

Gravitation and Cosmology (GC) has been selected as the most appropriate journal for the dissemination of the two publishable articles contained within this dissertation. GC is an international peer reviewed journal which is published in collaboration with the Russian Gravitational Society. GC covers a range of topics including theoretical and experimental gravity, relativistic astrophysics and cosmology, related mathematical methods and fundamental physical constants.

This dissertation contains a theoretical exploration of the behaviour of charged particles held in gravitational eigenstates in non-relativistic regions of deep gravitational wells. This research relates to the GC focus topic of theoretical gravity and astrophysics generally.

Indeed, papers on gravitational eigenstates have previously been published in GC. Ernest and Collins (2012) is the first publication in GC directly exploring gravitational eigenstates.

Whinray and Ernest (2018) is another relevant paper published in GC which was produced from a Charles Sturt University honours study looking at the empirical trends of state to state transition rates and lifetimes of gravitational eigenstates. The first paper in this dissertation directly extends and supports the work by Whinray and Ernest (2018) by exploring the effect of the quantum eigenvalue m on gravitational eigenstates. The second paper in this dissertation relies on the findings of the first paper and further extends the knowledge of gravitational eigenstates, and hence it is sensible to publish the second paper in GC as well.

The word limit provided by GC is reasonable for the scope of the papers here, with a character limit of ~40,000, equating to word limit of ~8,000. GC also reports an impact rating of 0.880 in 2019. This suggests the competitiveness of the journal does not preclude the likely publication of research produced in a small-scale honours project. Please see

Appendix A for GC guidelines for Authors. Further details of GC can also be viewed by clicking on the following url:

<https://www.springer.com/journal/12267/submission-guidelines>

Paper 1: Relations between the quantum eigenvalue m and transition rates of charged particles held in gravitational eigenstates in non-relativistic regions of deep gravitational wells

1.1) Abstract

This paper continues an ongoing investigation into the theoretical behaviour of charged particles held in gravitational eigenstates in non-relativistic regions of deep gravitational wells. Previous theoretical studies have shown gravitational eigenstates in deep gravitational wells can exhibit extremely small interaction cross sections and lifetimes which exceed the age of the universe as a result of the composition of the eigenspectrum of their wave functions. Gravitational eigenstates could provide a source of dark matter without the need to resort to exotic particles or exotic physics. However, the development of the theory of gravitational eigenstates is challenging due to the extreme scale of quantum eigenvalues involved. Recent research has sought empirical trends for state to state transition rates and lifetimes of gravitational eigenstates to extrapolate computationally practical calculations to galactic scales. Whilst support was found for decreasing interaction cross sections for increasing quantum eigenvalues n and l , the initial quantum eigenvalue m_i was set to 0 and only the $\Delta m = 0$ decay channel was assessed [1]. This paper explores how different values of m_i and Δm affect state to state transition rates and state lifetimes. It is demonstrated that the sum of all possible Δm decay channels is constant for all m_i . Estimates of how well the decay channel $\Delta m = 0$ approximates the state to state transition rate of the $\Delta m = -1$ and $\Delta m = 1$ decay channels for various m_i is provided. It was found that the $\Delta m = 0$ decay channel represents the greatest state to state transition rate when $m_i = 0$. This paper supports previous research [1] and shows that a maximum constraint on state to state transition rate for $m_i = 0$ can be achieved through only evaluating the $\Delta m = 0$ decay channel.

Abstract Length: 20 lines (maximum allowed is 20 lines)

Character count of article: 36 484 (maximum allowed is 40 000)

1.2) Introduction:

Compelling observational evidence for the existence of dark matter includes flat rotation curves of galaxies [2], gravitational lensing studies [3] and galaxy and cluster collisions leading to decoupling of baryonic and dark matter material [4]. However, after over 30 years of concentrated effort, and a rapid improvement in analysis techniques and detector technology, no observational evidence has clearly established the existence of a dark matter particle required for the leading cosmological model, Lambda Cold Dark Matter [5, 6]. Alternative theories of gravity such as Modified Newtonian Dynamics Model [7] and its relativistic extension, Tensor-Vector-Scalar gravity, have also failed to explain all the observational evidence for dark matter [8]. Therefore, continued speculation about the nature of dark matter is warranted.

Similar to Rydberg atoms, it has been shown that charged particles held in gravitational eigenstates in deep gravitational wells with high n and relatively high l quantum eigenvalues display theoretical properties consistent with the evidence for dark matter. This set of gravitational eigenstates are referred to as “quantum dark matter” (QDM). QDM is novel in its potential to account for the origin of dark matter using only known particles and known physics [1, 9-11]

The study of gravitational eigenstates in physical systems where gravity becomes a particle's dominant binding energy requires the application of quantum theory beyond customary dimensions. There is no known formal limitation to quantum theory based on the size of the phenomena and evidence of macroscopic applications exist. Superluminal connection of entangled particles over 10km [12], quantum superposition of macroscopically distinct

magnetic flux states [13] and Bose-Einstein condensates [14] are just some of the demonstrable macroscopic quantum phenomena.

The theoretical study of QDM faces many technical mathematical challenges. Quantum mechanics applied to a system as large as a galaxy is beyond current computer technology. Indeed, despite experimental evidence of gravitational eigenstates [15], theoretical investigation of their properties remains incomplete.

Ernest [10, 11] developed solutions to angular and radial overlap integrals to simplify the study of transition rates and interactive properties of gravitational eigenstates. However, the solutions to the overlap integrals still involve summations that quickly become computationally impractical at the scale of relevant gravitational systems. Ernest [10, 11] also developed approximations for gravitational eigenstate functions with high n and relatively high l quantum eigenvalues.

Studies into empirical trends of state to state transition rates and lifetimes of gravitational eigenstates have also been performed. Whinray and Ernest [1] found the empirical relationship for state lifetimes τ could be expressed as $\tau \propto n^3 l^\beta$ where $\beta = 2.009 \pm 0.004$. Whinray and Ernest [1] also studied state to state transition rate as a function of p , defined as $p \equiv n - l$. However, in order to reduce computation time, the initial (m_i) and final (m_f) value of the gravitational z projection sublevel was set to zero and thus only the $\Delta m = 0$ decay channel was explored. How well this research approximates or constrains eigenstates with different m_i quantum eigenvalues and Δm decay channels is not established.

Understanding how m_i and the decay channel Δm affects state to state transition rates will constrain predictions regarding the behaviour of gravitational eigenstates from previous and future studies. Hence the purpose of this paper is to investigate the effect that m_i and Δm has on state to state transition rates and lifetimes of gravitational eigenstates held in non-relativistic regions of deep gravitational wells. This will improve the understanding of what set of quantum eigenvalues is likely to exhibit dark matter properties.

(Examiners: Please read appendix B for an extended literature review relevant to both paper 1 and paper 2.)

1.3) Methods:

1.3.1) Mathematical theory – Formulation of a Schrödinger Equation for weak gravity:

The mathematical framework for the Schrödinger Equation for weak gravity has previously been developed by Ernest [10, 11] and is reproduced here. A small particle mass m_p is presumed to exist in non-relativistic regions of a deep gravitational well provided by a large electrically neutral mass M ($m_p \ll M$). The established Schrodinger equation for Hydrogen is

$$-\frac{\hbar^2}{2\mu} \nabla^2 \psi(r, \theta, \phi) - \frac{e^2}{4\pi\epsilon_0 r} \psi(r, \theta, \phi) = i\hbar \frac{\partial}{\partial t} \psi(r, \theta, \phi) \quad (1.1)$$

where

$$\nabla^2 \psi(r, \theta, \phi) = \frac{1}{r^2 \sin(\theta)} \left[\sin(\theta) \frac{\partial}{\partial r} \left(r^2 \frac{\partial \psi}{\partial r} \right) + \frac{\partial}{\partial \theta} \left(\sin(\theta) \frac{\partial \psi}{\partial \theta} \right) + \frac{1}{\sin(\theta)} \frac{\partial^2 \psi}{\partial \phi^2} \right] \quad (1.2).$$

The formulation of the Schrodinger equation for weak gravity is formed by analogizing the Hydrogen case through replacing the Coulomb potential in (1.1) with the Newtonian gravitational potential to give

$$-\frac{\hbar^2}{2\mu}\nabla^2\psi(r, \theta, \phi) - \frac{GMm_p}{r}\psi(r, \theta, \phi) = i\hbar\frac{\partial}{\partial t}\psi(r, \theta, \phi) \quad (1.3)$$

where μ is the reduced mass

$$\mu = \frac{m_p M}{m_p + M} \quad (1.4)$$

and all other symbols have their usual meanings.

Using separation of variables leads to the time independent Schrodinger equation for weak gravity,

$$-\frac{\hbar^2}{2\mu}\nabla^2\psi(r, \theta, \phi) - \frac{GMm_p}{r}\psi(r, \theta, \phi) = E_n\psi(r, \theta, \phi) \quad (1.5)$$

where the energy levels E_n are

$$E_n = -\frac{\mu G^2 m_p^2 M^2}{2\hbar^2} \left(\frac{1}{n^2} \right) \quad (1.6).$$

The eigenfunction solutions to (1.5) are

$$|u\rangle = u_{n,\ell,m}(\mathbf{r}, t) = R_{n,\ell}(r)Y_{\ell,m}(\theta, \phi) \quad (1.7)$$

where l , m and n are the standard quantum eigenvalues numbers. The radial component and spherical harmonics in (1.7) are respectively given by

$$R_{n,l}(r) = N_{nl} \left(\frac{2r}{nb_0} \right)^l e^{\left(-\frac{r}{nb_0} \right)} L_{n-l-1}^{2l+1} \left(\frac{2r}{nb_0} \right) \quad (1.8)$$

and

$$Y_{l,m}(\theta, \phi) = \frac{(-1)^m}{2^l l!} \sqrt{\frac{2l+1}{4\pi} \frac{(l-m)!}{(l+m)!}} (\sin\theta)^m e^{im\phi} \sum_{k=0}^l \frac{(-1)^{l-k} l! (2k)! (\cos(\theta))^{2k-l-m}}{k! (l-k)! (2k-l-m)!} \quad (1.9).$$

Similar to the parameter a_0 in the atomic case, Ernest [10, 11] introduces b_0 where

$$b_0 = \frac{\hbar^2}{\mu G M m_p} \quad (1.10).$$

In (1.8), the normalisation constant is given by

$$N_{nl} = \left\{ \left(\frac{2}{nb_0} \right)^3 \frac{(n-l-1)!}{2n((n+l)!)^3} \right\}^{\frac{1}{2}} \quad (1.11)$$

and

$$L_{n-l-1}^{2l+1} \left(\frac{2r}{nb_0} \right) = (n+1)! \sum_{k=0}^{n-l-1} \frac{(-1)^{k+2l} \left(\frac{2r}{nb_0} \right)^k}{(n-l-1-k)! (2l+1+k)! k!} \quad (1.12)$$

are the standard form of the Laguerre polynomials.

1.3.2) Avoiding relativistic regions of gravity around the central mass M :

The Schrodinger Equation for weak gravity is only accurate in non-relativistic regions of gravity. However, the calculation of gravitational eigenstates quickly exceeds the computational resources of this investigation as the initial principle quantum number n_i increases beyond ~ 2000 . Therefore, a central mass which is as large as possible without requiring the application of relativistic gravity is required at values of $n < 2000$.

The average radial position of a gravitational eigenstate is given by

$$r_n = n^2 b_0 \quad (1.13)$$

and the Schwarzschild radius is

$$r_s = \frac{2GM_0}{c^2} \quad (1.14).$$

Relativistic regions around the central mass are avoided by ensuring $r_n \gg r_s$. By solving for a central mass where $r_n \geq 1000r_s$ for $n \sim 1$, it has been shown that the central mass required is 6.4×10^9 kg [1]. In order to be able to directly compare results with Whinray and Ernest [1], the same central mass of 6.4×10^9 kg will be applied here.

1.3.3) Mathematical Theory – State to state transition probability:

The mathematical theory for state to state transition probability is reproduced here from Ernest [10]. The state to state transition probability for radiative dipole decay $A_{i,f}$ for a transition $n_i \rightarrow n_f$ from initial state $|i\rangle$ to final state $|f\rangle$ is given by

$$A_{i,f} = \frac{\omega_{if}^3 |\langle f | e\mathbf{r} | i \rangle|^2}{3\varepsilon_0 \pi \hbar c^3} = \frac{\omega_{if}^3 \Pi_{if}^2}{3\varepsilon_0 \pi \hbar c^3} \quad (1.15).$$

Here e is the electronic charge, ε_0 the electrical permittivity of free space, ω_{if} is the angular frequency and Π_{if} is the absolute value of the dipole matrix element for spontaneous decay for the transition i to f . All other symbols have their usual meanings. The angular frequency ω_{if} is given by

$$\omega_{if} = \frac{\mu G^2 m_p^2 M^2}{2\hbar^2} (n_f^{-2} - n_i^{-2}) \quad (1.16).$$

From (1.15), $\Pi_{if} = |\langle f | e\mathbf{r} | i \rangle|$. Thus Π_{if} can be expressed unambiguously as

$$\begin{aligned}\Pi_{if} &= \left| \int_0^\infty \int_0^\pi \int_0^{2\pi} R_{nf,\ell f}^* Y_{\ell f,mf}^* e \mathbf{r} R_{ni,\ell i} Y_{\ell i,mi} r^2 \sin^2(\theta) \cos(\phi) d\phi d\theta dr \right| \\ &= \sqrt{\Pi_{ifx}^2 + \Pi_{ify}^2 + \Pi_{ifz}^2}\end{aligned}\quad (1.17)$$

where Π_{ifx} , Π_{ify} and Π_{ifz} are the x, y and z components of Π_{if} .

Π_{ifx}^2 , Π_{ify}^2 and Π_{ifz}^2 can be respectively written as

$$\Pi_{ifx}^2 = e \int_0^\infty R_{ni,\ell i}^* R_{nf,\ell f} r^3 dr \int_0^\pi \int_0^{2\pi} Y_{\ell i,mi}^* Y_{\ell f,mf} \sin^2(\theta) \cos(\phi) d\phi d\theta \quad (1.18)$$

$$\Pi_{ify}^2 = e \int_0^\infty R_{ni,\ell i}^* R_{nf,\ell f} r^3 dr \int_0^\pi \int_0^{2\pi} Y_{\ell i,mi}^* Y_{\ell f,mf} \sin^2(\theta) \sin(\phi) d\phi d\theta \quad (1.19)$$

$$\Pi_{ifz}^2 = e \int_0^\infty R_{ni,\ell i}^* R_{nf,\ell f} r^3 dr \int_0^\pi \int_0^{2\pi} Y_{\ell i,mi}^* Y_{\ell f,mf} \sin(\theta) \cos(\theta) d\phi d\theta \quad (1.20).$$

By observation, the dipole matrix element Π_{if} in (1.17) involves overlap integrals over the azimuthal, polar and radial coordinates. This leads to an allowed set of decay channels requiring the selection rules for quantum numbers m and l to obey $\Delta m = -1, 0, +1$ and $\Delta l = -1, +1$.

1.3.4) Mathematical Theory – State lifetimes:

The net decay rate A_i for state $|i\rangle$ is found by summing the state to state decay rates $A_{i,k}$ for each possible decay channel $|i\rangle \rightarrow |k\rangle$, so

$$A_i = \sum_k A_{i,k} = \frac{1}{\tau_i} \quad (1.21)$$

where τ_i is the state lifetime [10].

1.3.5) State to state transition rates as a function of Δm and m_i :

The purpose of this section was to examine state to state transition rates as a function of Δm and m_i . For all calculations, n_i was set to 150 and l_i was set to either 144 or 30 to give a p_i ($\equiv n_i - l_i$) value of 6 or 120 respectively. For $p_i = 6$, the range of m_i values evaluated were -144, -138, -132, ..., 132, 138, 144 for $\Delta l = 1$, and -138, -132, 126, ..., 126, 132, 138 for $\Delta l = -1$. For $p_i = 120$, the range of m_i values evaluated were -30, -29, -28, ..., 28, 29, 30. For each m_i , state to state transition rates were calculated in turn for $\Delta m = -1, 0, 1$ for $\Delta p = -5, -2, 0$. For $\Delta p = -5$ and $\Delta p = -2$, the two possible cases, $\Delta l = 1$ and $\Delta l = -1$, were evaluated separately. For $\Delta p = 0$, only the case where $\Delta l = -1$ was evaluated due to selection rules.

(Examiners: Please see Appendix E for the relevant computer package and Appendix G for the computer program which was used to perform the calculations in this section).

1.3.6) State to state transition rates as a function of p_i for all Δm decay channels:

The purpose of this section was to evaluate state to state transition rates as a function of p_i and n_i across all Δm decay channels. Calculations were performed for $n_i = 5, 10, 15, \dots, 100$. The range evaluated for p_i was 1, 2, 3, ..., $n_i - 1$, though this had to be trivially modified as necessary to accommodate selection rules for evaluations of different Δp and Δl . All n_i and p_i combinations were evaluated for state to state decay rates for $\Delta p = -2, -1, 0$. For $\Delta p = -2$, both $\Delta l = 1$ and $\Delta l = -1$ transitions were calculated. Due to selection rules, for $\Delta p = -1$ and 0, only the $\Delta l = -1$ case was evaluated. For all calculations, m_i was set to 0. For all $n_i, p_i, \Delta p$ and Δl combinations, evaluation of state to state transition rates was performed for $\Delta m = -1, 0, 1$.

(Examiners: Please see Appendix E for the relevant computer package and Appendix G for the computer program which was used to perform the calculations in this section).

1.3.7) State lifetimes:

A given state $\{n_i, l_i, m_i\}$ can decay according to $\Delta n = -l_f + 1$ to $n - 1$, $\Delta l = -1$ or 1 and $\Delta m = -1$, 0 or 1 . The range of initial values used to evaluate state lifetimes was $n_i = 5 - 100$, $l_i = 3 - 95$ and $p_i = 2 - 85$. Here, m_i was set at 0 as the results from section 1.3.5 above indicated that the lifetime of a state is independent of m_i provided the state to state transition rate for all Δm cases are summed. State lifetimes were found by taking the reciprocal of the sum of all state to state transition rates for all possible decay channels as per equation (1.21). This section directly extended work by Whinray and Ernest [1] where only the $\Delta m = 0$ decay channel was used to estimate state lifetimes.

(Examiners: Please see Appendix E for the relevant computer package and Appendix F for the computer program which was used to perform the calculations in this section).

(Examiners: Please see Appendix C for additional methods regarding development of computer programs and detailed presentation of each calculation performed in sections 1.3.5, 1.3.6 and 1.3.7).

1.4) Results:

1.4.1) Results for state to state transition rates as a function of Δm and m_i :

The results here are produced from methods section 1.3.5, “State to state transition rates as a function of Δm and m_i ”.

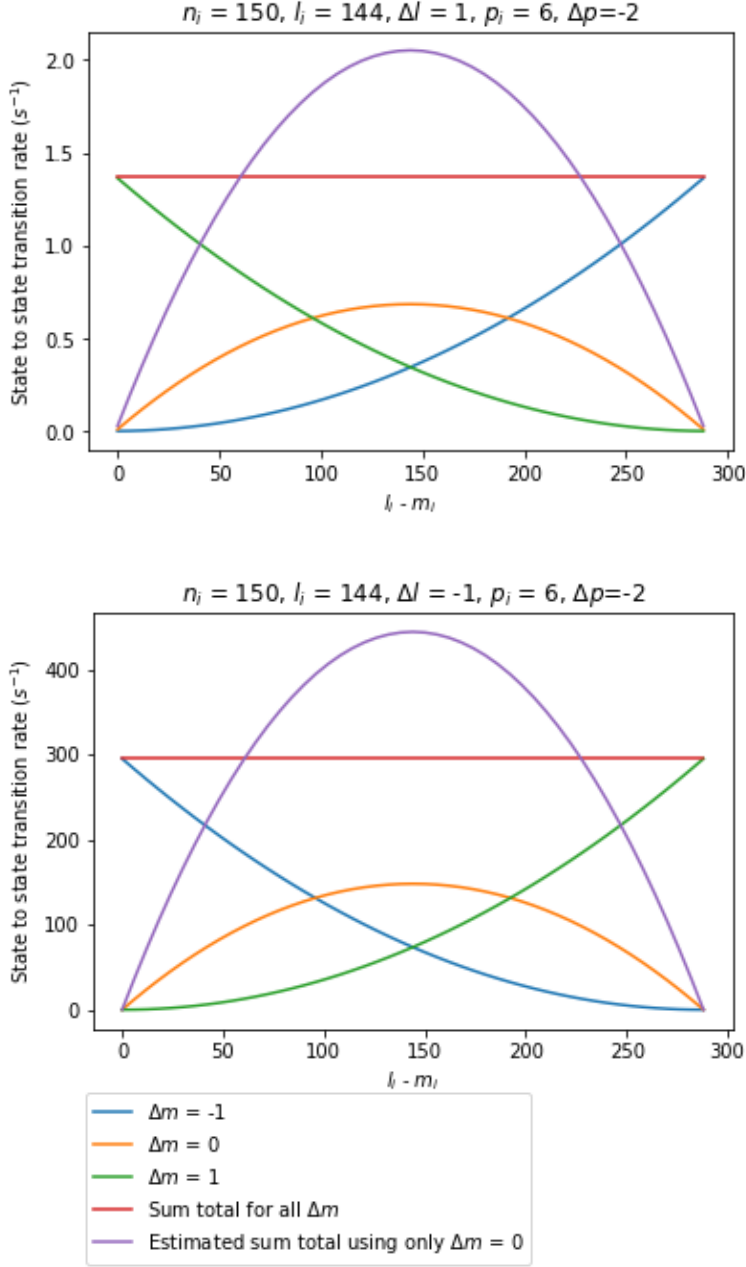


Fig. 1.4.1. State to state transitions rate $A_{i,f}$ as a function of $l_i - m_i$ and Δm for $n_i = 150$, $p_i = 6$, $\Delta p = -2$ and $l_i = 144$. (a) $\Delta l = 1$. (b) $\Delta l = -1$.

Figure 1.4.1 plots state to state transition rate as a function of $l_i - m_i$ and Δm for $n_i = 150$, $p_i = 6$ and $\Delta p = -2$. In 1.4.1(a), $\Delta l = 1$ and in 1.4.1(b), $\Delta l = -1$. The green line represents the transition rate for the $\Delta m = 1$ decay channel which is equal to zero when $l_i - m_i = 288$ in figure 1.4.1(a). However, in 1.4.1(b) the transition rate is 0 when $l_i - m_i = 0$. At $l_i - m_i = 0$, the transition $\Delta m = 1$, $\Delta l = -1$ would result in the prohibited combination of quantum eigenvalues

$l_i = 143$ and $m_i = 145$, hence the transition rate falls to 0. The transition rate for the $\Delta m = 1$ decay channel is maximum in 1.4.1(a) when $l_i - m_i$ is minimum. Conversely, the transition rate for the $\Delta m = 1$ decay channel is maximum in 1.4.1(b) when $l_i - m_i$ is maximum.

The blue line in figure 1 represents the transition rate for the $\Delta m = -1$ decay channel. In 1.4.1(a) this line is minimal when $l_i - m_i = 0$ and maximal when $l_i - m_i = 288$. However, the converse is true in figure 1.4.1(b). When $l_i - m_i = 288$, $m_i = -144$ and $l_i = 144$. Thus, when $l_i - m_i$ is at its maximum, the transition $\Delta m = -1$, $\Delta l = -1$ is prohibited so the transition rate for the $\Delta m = -1$ decay channel falls to 0 in figure 1.4.1(b). The orange line represents the transition rate for the $\Delta m = 0$ decay channel which has a peak when $l_i - m_i = 144$ in both figures 1.4.1(a) and (b). The transition $\Delta m = 0$, $\Delta l = -1$ is prohibited at $l_i - m_i = 0$ and $l_i - m_i = 144$. Hence the transition rate falls to zero at $l_i - m_i = 0$ and $l_i - m_i = 144$ in both figures 1.4.1(a) and (b).

The red line in figure 1 represents the sum of the state to state transition rate for the $\Delta m = -1$, $\Delta m = 0$ and $\Delta m = 1$ decay channels. The red line is horizontal and demonstrates the principle finding that the sum of all possible Δm decay channels is constant. The purple line represents the estimated sum for state to state transitions for all Δm decay channels found by multiplying the transition rate for the $\Delta m = 0$ decay channel by three. This is important since this estimate has been used in a previous study [1]. When $l_i - m_i$ is close to minimal or maximal, using the estimate represented by the purple line results in a gross underestimate of transition rate. However, when $l_i - m_i = 144$, this estimate significantly exceeds the true sum of the transition rate.

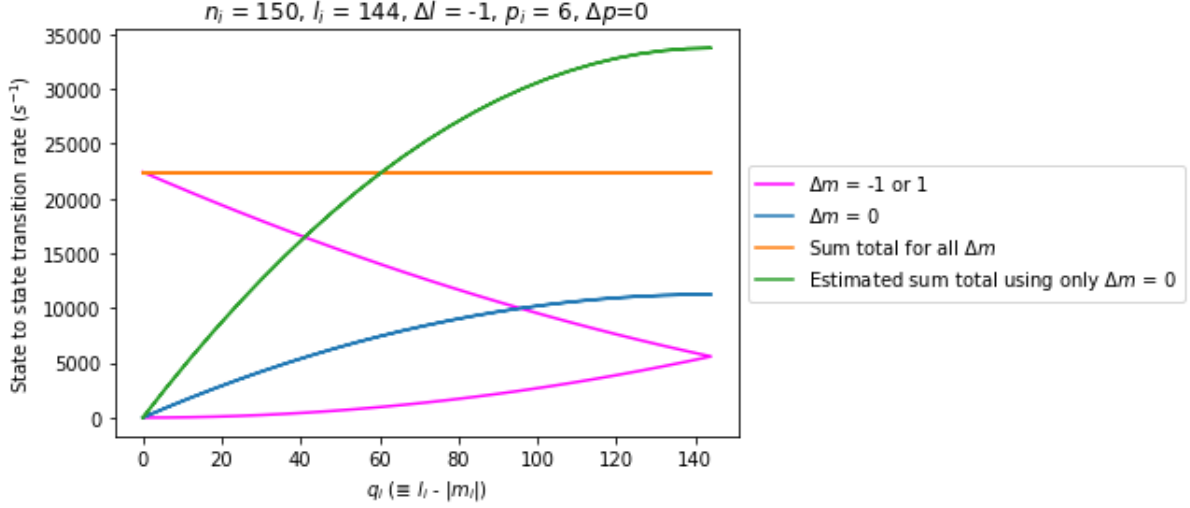


Fig. 1.4.2. State to state transitions rates $A_{i,f}$ as a function of $q_i (\equiv l_i - |m_i|)$ and Δm for $n_i = 150, p_i = 6, \Delta p = 0, l_i = 144$ and $\Delta l = -1$.

Figure 1.4.2 plots state to state transition rate as a function of $q_i (\equiv l_i - |m_i|)$ and Δm for $n_i = 150, p_i = 6$ and $\Delta p = 0$. Figure 2 is similar to figure 1.4.1 except the transition rates for the $\Delta m = -1$ and $\Delta m = 1$ decay channels have become indistinguishable from each other and are both represented by the magenta line. The blue line represents the transition rate for the $\Delta m = 0$ decay channel, which is minimal when q_i is minimal and maximal when q_i is maximal. The orange line demonstrates that the sum for the state to state transition rate for all possible Δm decay channels is constant. The green line represents three times the transition rate for the $\Delta m = 0$ decay channel. This reflects the accuracy of estimating the sum of the transition rates for all Δm decay channels using only the $\Delta m = 0$ decay channel. When q_i is maximum, the estimated sum of the transition rates exceeds the true figure and when q_i is minimum, the estimated sum of the transition rates falls to 0.

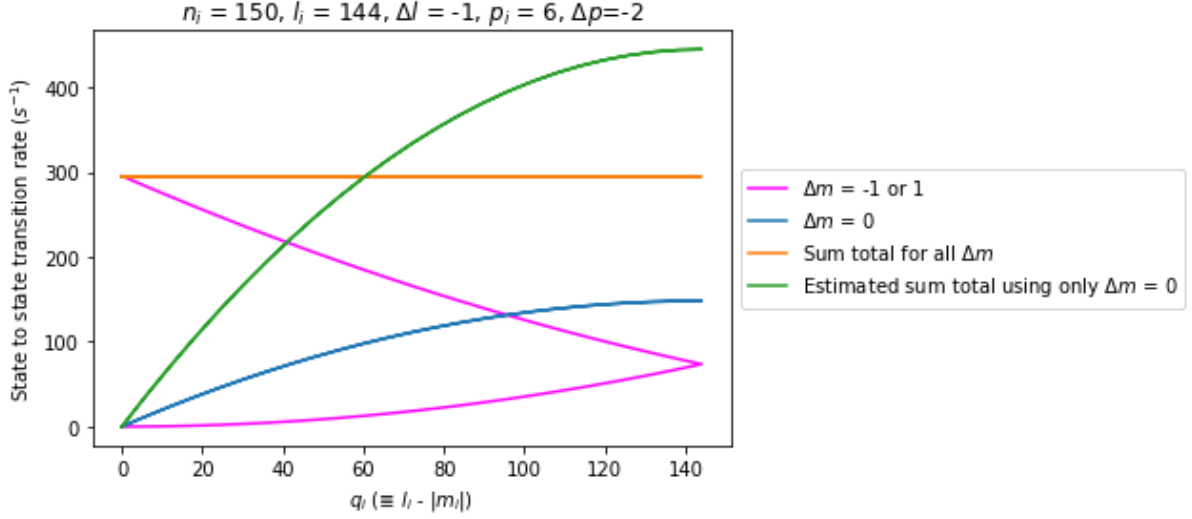


Fig. 1.4.3. State to state transitions rates $A_{i,f}$ as a function of $q_i (\equiv l_i - |m_i|)$ and Δm for $n_i = 150$, $p_i = 6$, $\Delta p = -2$, $l_i = 144$ and $\Delta l = -1$.

Figure 1.4.3 plots state to state transition rate as a function of q_i and Δm for $n_i = 150$, $p_i = 6$ and $\Delta p = -2$ with $\Delta l = -1$. The sum of the state to state transition rates for all Δm decay channels is decreased compared with figure 1.4.2 which indicates the transition in p (and hence n and l) is less favoured. The main finding is the consistency with the trends demonstrated in figure 1.4.22.

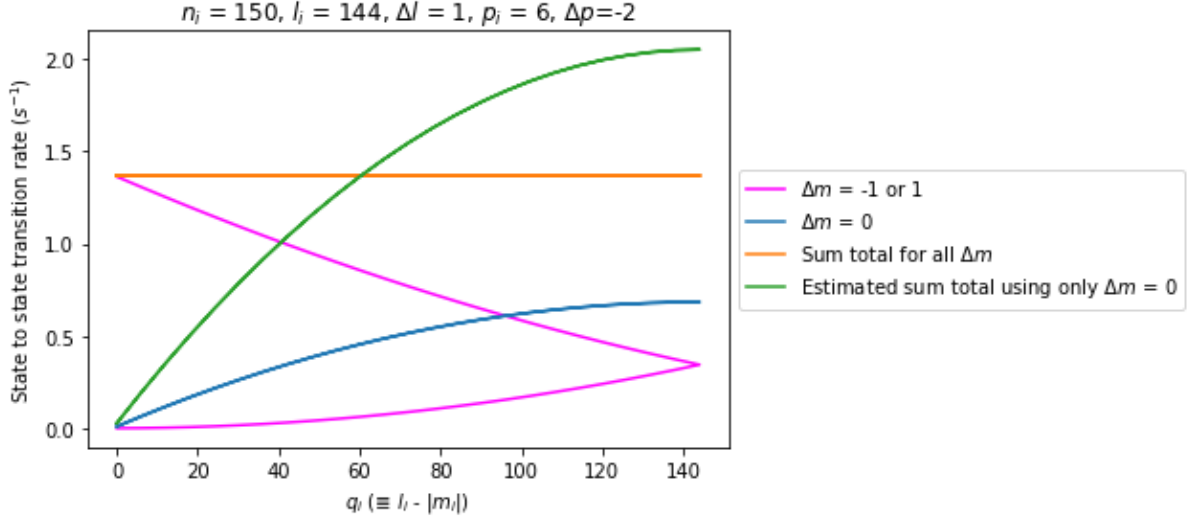


Fig. 1.4.4. State to state transitions rates $A_{i,f}$ as a function of $q_i (\equiv l_i - |m_i|)$ and Δm for $n_i = 150$, $p_i = 6$, $\Delta p = -2$, $l_i = 144$ and $\Delta l = 1$.

Figure 1.4.4 is the same as figure 1.4.3 except $\Delta l = 1$ instead of -1 . The sum of the state to state transition rates for all Δm decay channels is decreased compared with figure 3, however the trends are the same.

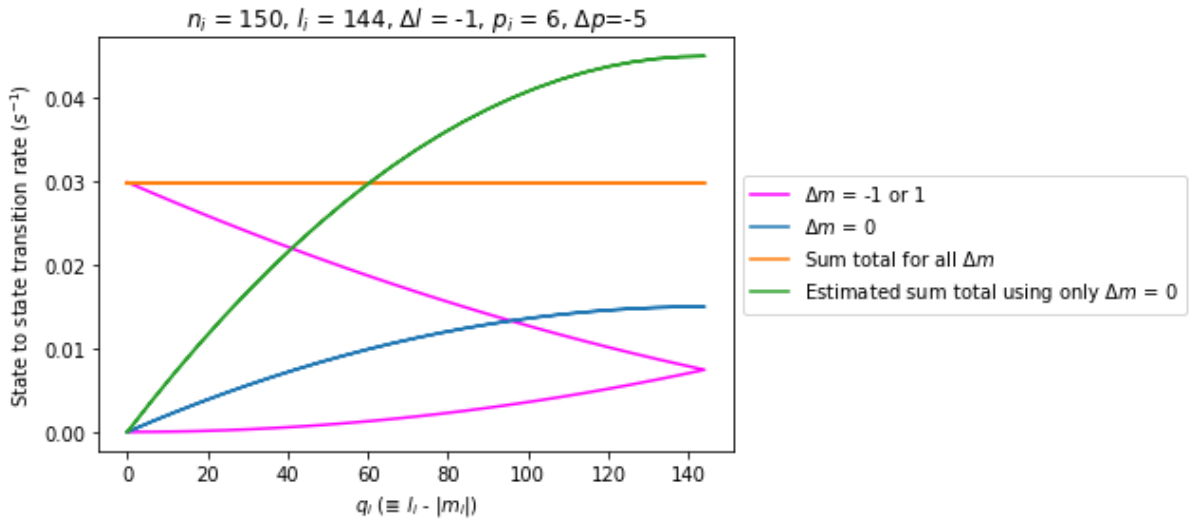


Fig. 1.4.5. State to state transitions rates $A_{i,f}$ as a function of $q_i (\equiv l_i - |m_i|)$ and Δm for $n_i = 150$, $p_i = 6$, $\Delta p = -5$, $l_i = 144$ and $\Delta l = -1$.

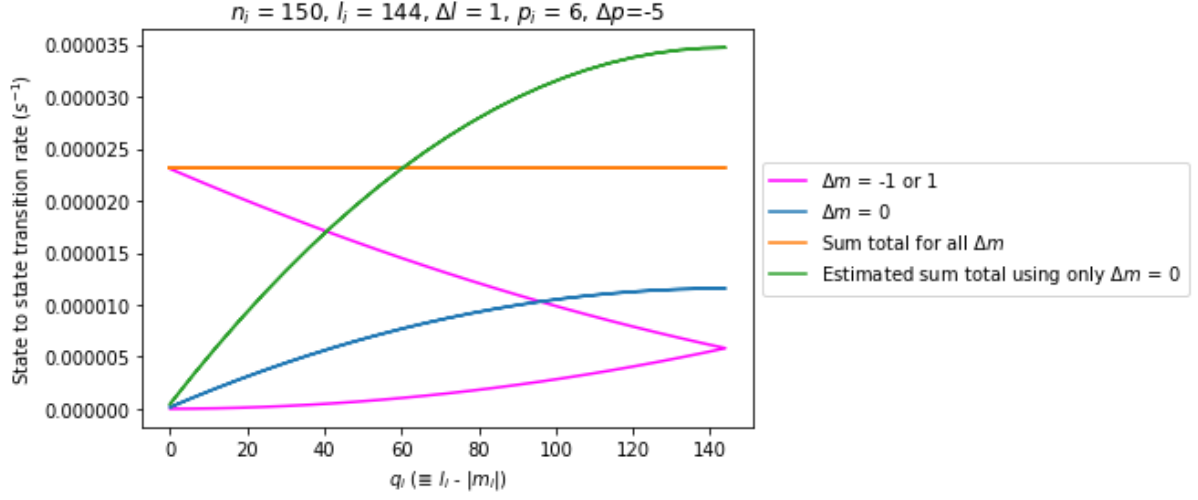


Fig. 1.4.6. State to state transitions rates $A_{i,f}$ as a function of $q_i (\equiv l_i - |m_i|)$ and Δm for $n_i = 150, p_i = 6, \Delta p = -5, l_i = 144$ and $\Delta l = 1$.

Figures 1.4.5 and 1.4.6 plot state to state transition rate as a function of q_i and Δm for $n_i = 150, p_i = 6$ and $\Delta p = -5$. Consistent with the findings in figure 1.4.3 and 1.4.4, when $\Delta l = -1$ (figure 1.4.5) the state to state transition rate is significantly higher compared with the state to state transition rate for $\Delta l = 1$ (figure 1.4.6). Across figures 1.4.1 to 1.4.6, the sum of all the transition rates for all possible Δm decay channels is constant.

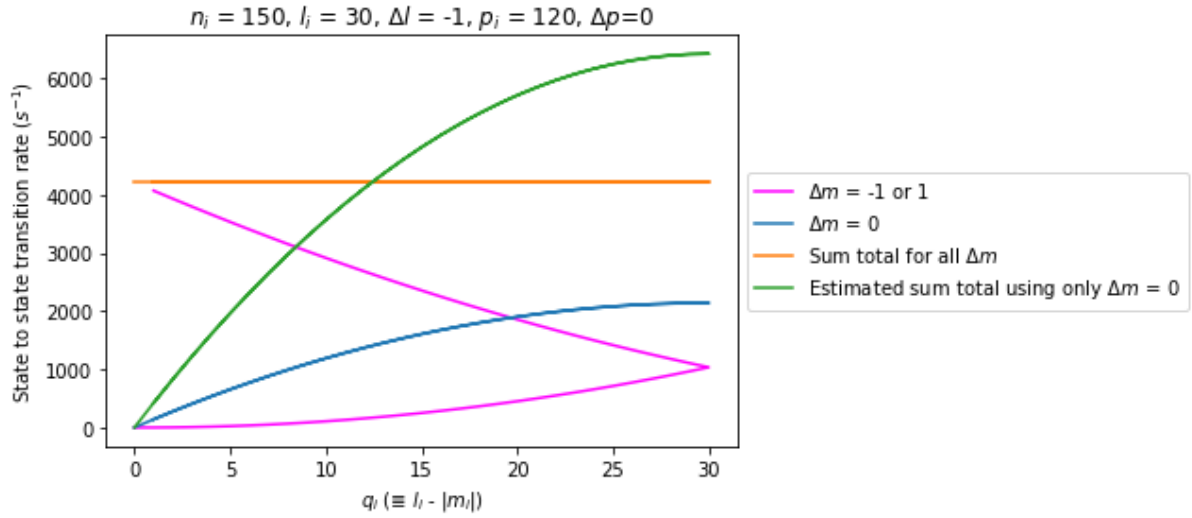


Fig. 1.4.7. State to state transitions rates $A_{i,f}$ as a function of $q_i (\equiv l_i - |m_i|)$ and Δm for $n_i = 150, p_i = 120, \Delta p = 0, l_i = 30$ and $\Delta l = -1$.

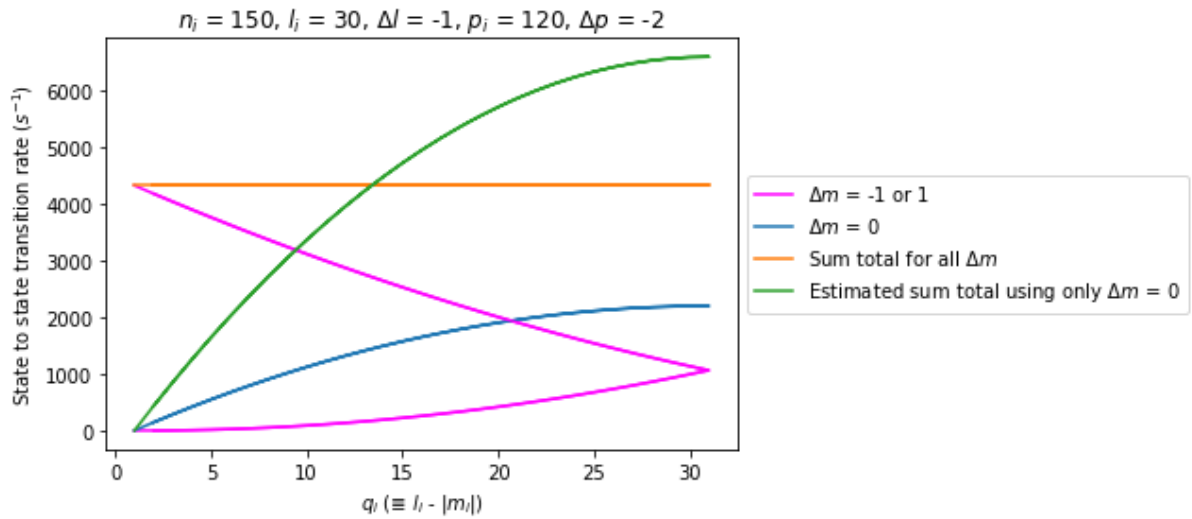


Fig. 1.4.8. State to state transitions rates $A_{i,f}$ as a function of $q_i (\equiv l_i - |m_i|)$ and Δm for $n_i = 150, p_i = 120, \Delta p = -2, l_i = 30$ and $\Delta l = -1$.

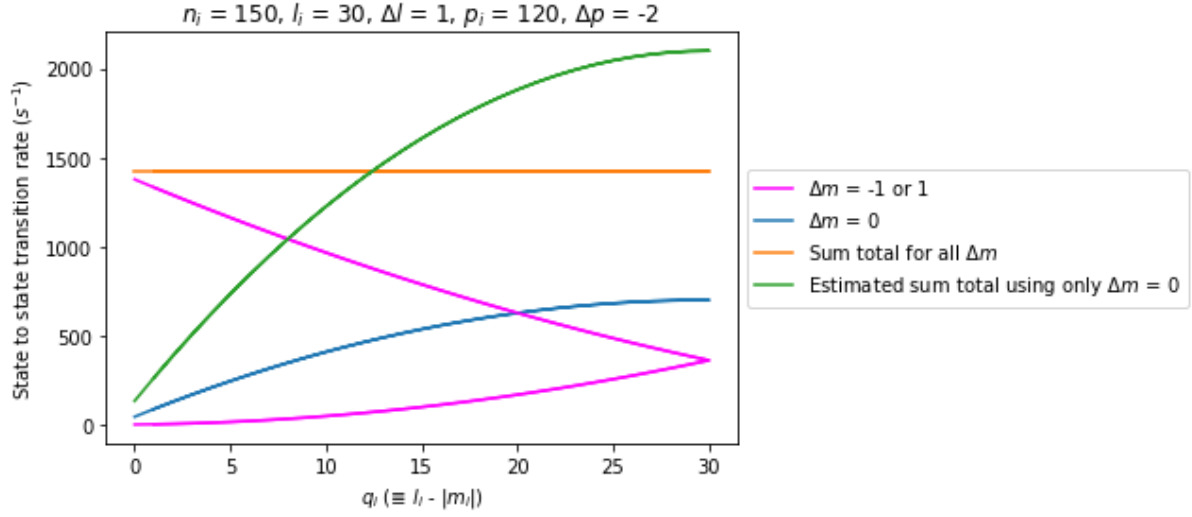


Fig. 1.4.9. State to state transitions rates $A_{i,f}$ as a function of $l_i - m_i$ and Δm for $n_i = 150$, $p_i = 120$, $\Delta p = -2$, $l_i = 30$ and $\Delta l = 1$.

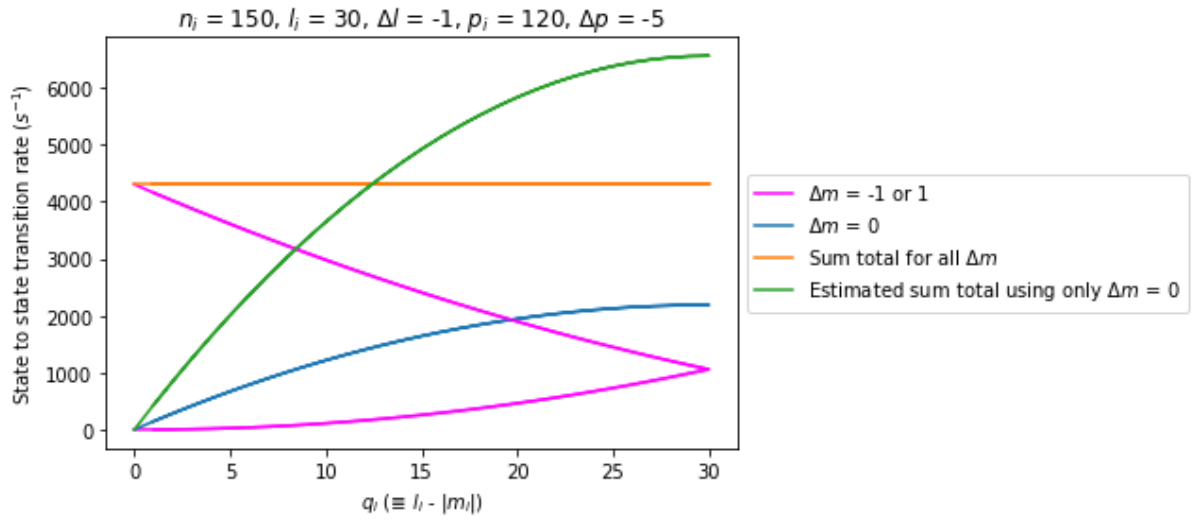


Fig. 1.4.10. State to state transitions rates $A_{i,f}$ as a function of $l_i - m_i$ and Δm for $n_i = 150$, $p_i = 120$, $\Delta p = -5$, $l_i = 30$ and $\Delta l = -1$.

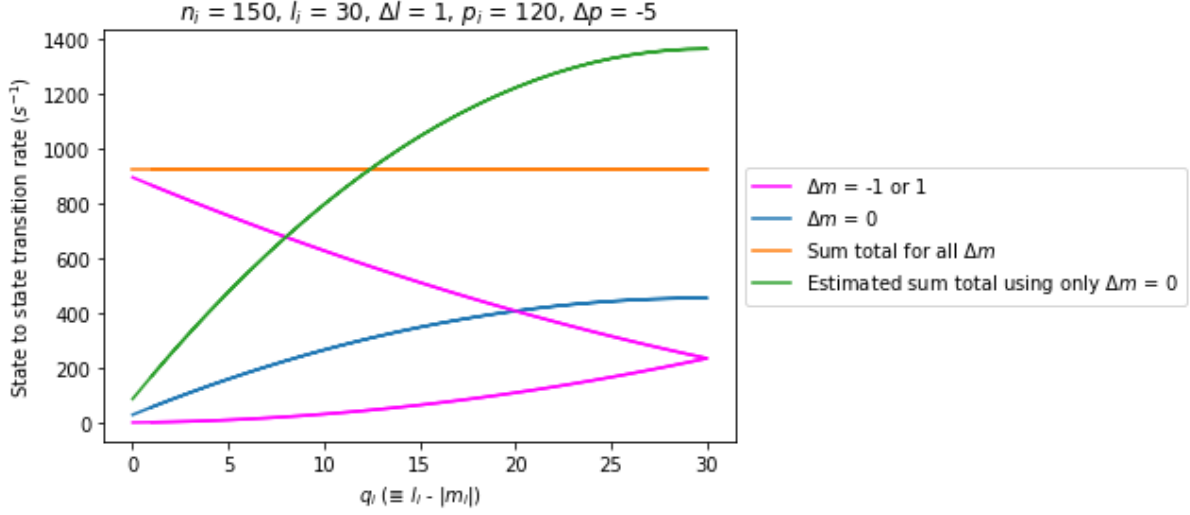


Fig. 1.4.11. State to state transitions rates $A_{i,f}$ as a function of $l_i - m_i$ and Δm for $n_i = 150$, $p_i = 120$, $\Delta p = -5$, $l_i = 30$ and $\Delta l = 1$.

Figures 1.4.7, 1.4.8, 1.4.9, 1.4.10 and 1.4.11 correlate respectively with figures 1.4.2, 1.4.3, 1.4.4, 1.4.5 and 1.4.6. The only difference between each respective figure is the value of p_i which is 120 for figures 1.4.7 to 1.4.11, and 6 for figures 1.4.2 to 1.4.6. The same trends found in figures 1.4.2-1.4.6 are found in figures 1.4.7-1.4.11. Notably, the sum of state to state transition rates for all possible Δm decay channels is always constant. Furthermore, the $\Delta l = -1$ decay channel is associated with a higher state to state transition rate than the $\Delta l = 1$ decay channel. When $\Delta p = 0$, the summed state to state transition rate for all Δm decay channels has been found to be greater for the case where $p_i = 6$. However, when $\Delta p = -5$ or -2 , the sum of all the state to state transition rates for all Δm decay channels has been found to be substantially greater in the cases where $p_i = 120$. The sum of the state to state transition rates for all Δm decay channels is similar for all cases where $p_i = 120$ and $\Delta l = -1$ for $\Delta p = 0, -2$ and -5 . However, the trend is not repeated for $p_i = 6$.

Table 1.4.1:

Ratio of m_i to l_i where the transition rate for the $\Delta m = 0$ decay channel best predicts the transition rate for the $\Delta m = 1$ and $\Delta m = -1$ decay channels for various p_i , Δl and Δp

p_i	Δl	Δp	Optimal m_i / l_i to predict transition rate for the $\Delta m = -1$ decay channel using the transition rate for the $\Delta m = 0$ decay channel	Transition rate for $\Delta m = 0$ decay channel as a percentage of transition rate for $\Delta m = -1$ decay channel at optimal m_i/l_i	Optimal m_i/l_i to predict transition rate for the $\Delta m = 1$ decay channel using the transition rate for the $\Delta m = 0$ decay channel	Transition rate for the $\Delta m = 0$ decay channel as a percentage of the transition rate for the $\Delta m = 1$ decay channel at optimal m_i/l_i	Related Figure
6	-1	0	1/3	100.5	-1/3	100.5%	1.4.1, 1.4.2
120	-1	0	1/3	102.6	-1/3	102.6%	1.4.7
6	1	-2	-1/3	100.0%	1/3	100.0%	1.4.4
120	1	-2	-1/3	100.0%	1/3	100.0%	1.4.9
6	-1	-2	1/3	100.5%	-1/3	100.5%	1.4.3
120	-1	-2	1/3	102.6%	-1/3	102.6%	1.4.8
6	1	-5	-1/3	100.0%	1/3	100.0%	1.4.6
120	1	-5	-1/3	100.0%	1/3	100.0%	1.4.11
6	-1	-5	1/3	100.5%	-1/3	100.5%	1.4.5
120	-1	-5	1/3	102.6%	-1/3	102.6%	1.4.10

Table 1 provides the ratio of m_i to l_i where the transition rate for the $\Delta m = 0$ channel is closest to the transition rates for the $\Delta m = -1$ and $\Delta m = 1$ decay channels. When $\Delta l = -1$, the transition rate for the $\Delta m = -1$ decay channel is best approximated by the transition rate for the $\Delta m = 0$ channel when $m_i/l_i = 1/3$ and the transition rate for the $\Delta m = 1$ decay channel is best approximated by the transition rate for the $\Delta m = 0$ decay channel when $m_i/l_i = -1/3$. The $\Delta m = 0$ decay channel over-predicted the transition rate by a maximum of 2.6% whenever the $\Delta l = -1$ channel was used. Conversely, when $\Delta l = 1$, the transition rate for the $\Delta m = -1$ decay channel is best approximated when $m_i/l_i = -1/3$ and the transition rate for the $\Delta m = 1$ decay channel is best approximated by $m_i/l_i = 1/3$. In this case the $\Delta m = 0$ decay channel predicted the transition rate exactly to at least one decimal place.

Table 1.4.2:

Ratio of m_i to q_i where the best estimate of the sum of the transition rates for all Δm decay channels is provided by multiplying the transition rate for the $\Delta m = 0$ decay channel by three for various p_i , Δl and Δp

p_i	Δl	Δp	m_i/q_i	Estimate of sum of transition rates for all Δm decay channels found by multiplying the transition rate for the $\Delta m = 0$ decay channel by three, as a percentage of the total sum of the transition rates for all Δm decay channels (%)
6	-1	0	5/12	99.3%
120	-1	0	2/5	97.6%
6	1	-2	5/12	99.3
120	1	-2	2/5	97.8%
6	-1	-2	5/12	99.3%
120	-1	-2	2/5	97.6%
6	1	-5	5/12	99.3%
120	1	-5	2/5	97.8%
6	-1	-5	5/12	99.3%
120	-1	-5	2/5	97.6%

Table 1.4.2 demonstrates the sum of the transition rates for each Δm decay channels is best estimated by multiplying the transition rate for the $\Delta m = 0$ decay channel by three when $m_i/q_i \sim 40$ -42%. In all cases presented here there was an underestimate of the sum by a maximum of 2.4%.

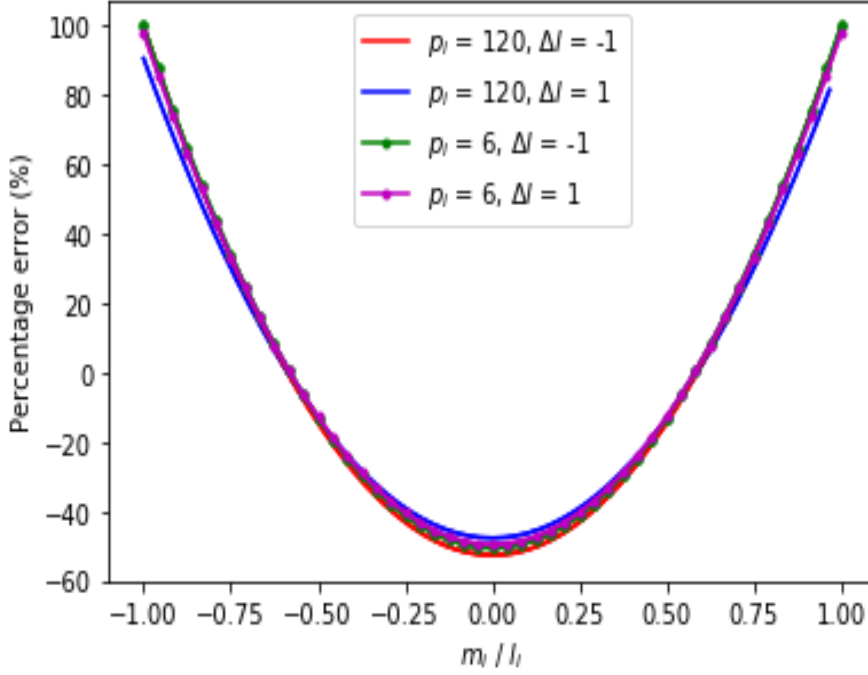


Fig. 1.4.12. Percentage error in estimating the sum of the state to state transition rates of all Δm decay channels by using the state to state transition rate for the $\Delta m = 0$ decay channel multiplied by three, plotted as a function of m_i / l_i .

Figure 1.4.12 shows the error obtained if the sum of state to state transition rates of all Δm decay channels is estimated by multiplying the transition rate for the $\Delta m = 0$ decay channel by three. Figure 1.4.12 plots the percentage error as a function of m_i / l_i . Positive error values indicate an overestimation in sum of state to state transition rate. All combinations of Δp , p_i , l_i , and Δl explored in figures 1.4.2 – 1.4.11 are plotted in figure 1.4.12. There is remarkable consistency regardless of the initial and final quantum numbers. When $\Delta l = -1$, the ‘U’ shaped curve is slightly sharper and reaches a marginally larger negative error than when $\Delta l = 1$ for the same p_i . The difference between the $\Delta l = -1$ and $\Delta l = 1$ curves is greater for $p_i = 120$. When m_i is greater than 70% of l_i , figure 1.4.12 demonstrates the sum of the state to

state transition rate for all Δm decay channels can be constrained to an upper limit if it is estimated through multiplying the decay rate for the $\Delta m = 0$ decay channel by three.

1.4.2) Results for state to state transition rates as a function of p_i for all Δm decay channels:

The results here are produced from methods section 1.3.6, “State to state transition rates as a function of p_i for all Δm decay channels”.

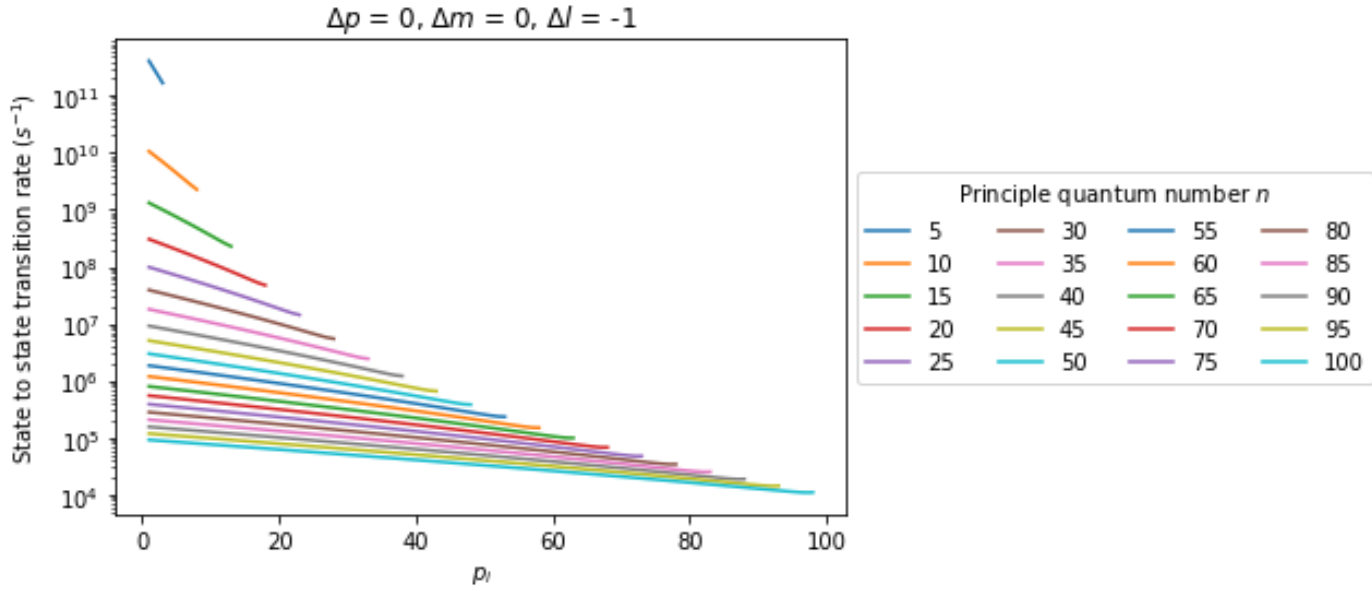


Fig. 1.4.13. State to state transitions rates $A_{i,f}$ as a function of p_i with $n = 5, 10, 15, \dots, 100$

for $m_i = 0$, $\Delta p = 0$, $\Delta m = 0$ and $\Delta l = -1$.

Figure 1.4.13 plots the state to state transition rate for various $n (= n_i)$ as a function of p_i when $\Delta p = 0$, $\Delta m = 0$ and $m_i = 0$. Due to selection rules, Δl can only be set to -1. Here $\Pi_{ifx} = \Pi_{ify} = 0$ which is the case whenever $\Delta m = 0$.

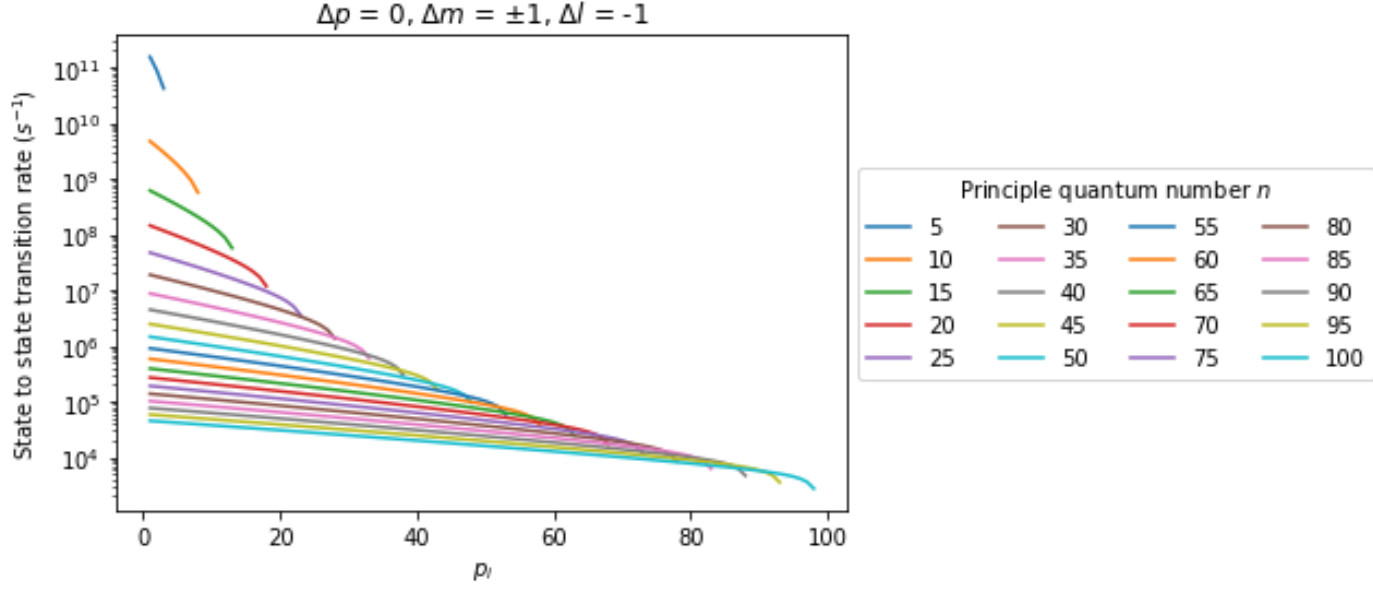


Fig. 1.4.14. State to state transitions rates $A_{i,f}$ as a function of initial p_i for $n = 5, 10, 15, \dots, 100$ for $m_i = 0$, $\Delta p = 0$, $\Delta m = \pm 1$ and $\Delta l = -1$.

Figure 1.4.14 uses the same initial quantum eigenvalues and changes in quantum numbers as figure 1.4.13, except here $\Delta m = \pm 1$. State to state transition rates were found to be the same for $\Delta m = 1$ and $\Delta m = -1$ for all scenarios in this section of results. Here $\Pi_{ifz} = 0$ (see equation 1.20) which is the case for all scenarios where $\Delta m = \pm 1$. The trends observed in figure 1.4.13 are similar to figure 1.4.14 with an approximately linear logarithmic decrease in state to state transition rate for increasing p_i . However, transition rates for the case where $\Delta m = \pm 1$ is significantly less than the transition rate for the case where $\Delta m = 0$ for the same n and p_i . Furthermore, there is a sudden decrease in transition rate for the higher values of p_i .

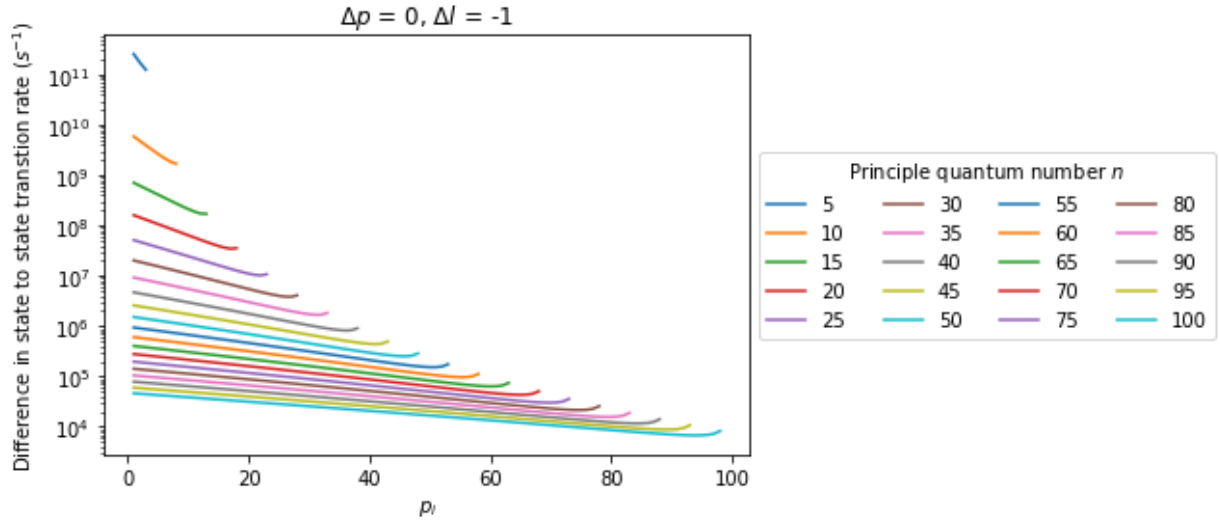


Fig. 1.4.15. Overestimation in state to state transition rates $A_{i,f}$ through using $\Delta m = 0$ to approximate the case where $\Delta m = \pm 1$ for $n = 5, 10, 15, \dots, 100$, $\Delta l = -1$ and $\Delta p = 0$.

Figure 1.4.15 quantifies the difference in state to state transition rate for the $\Delta m = 0$ decay channel compared to the transition rate for the $\Delta m = \pm 1$ decay channels. For all p_i and n , the state to state transition rate for the $\Delta m = 0$ decay channel is larger than for the state to state transition rate for the $\Delta m = \pm 1$ decay channels.

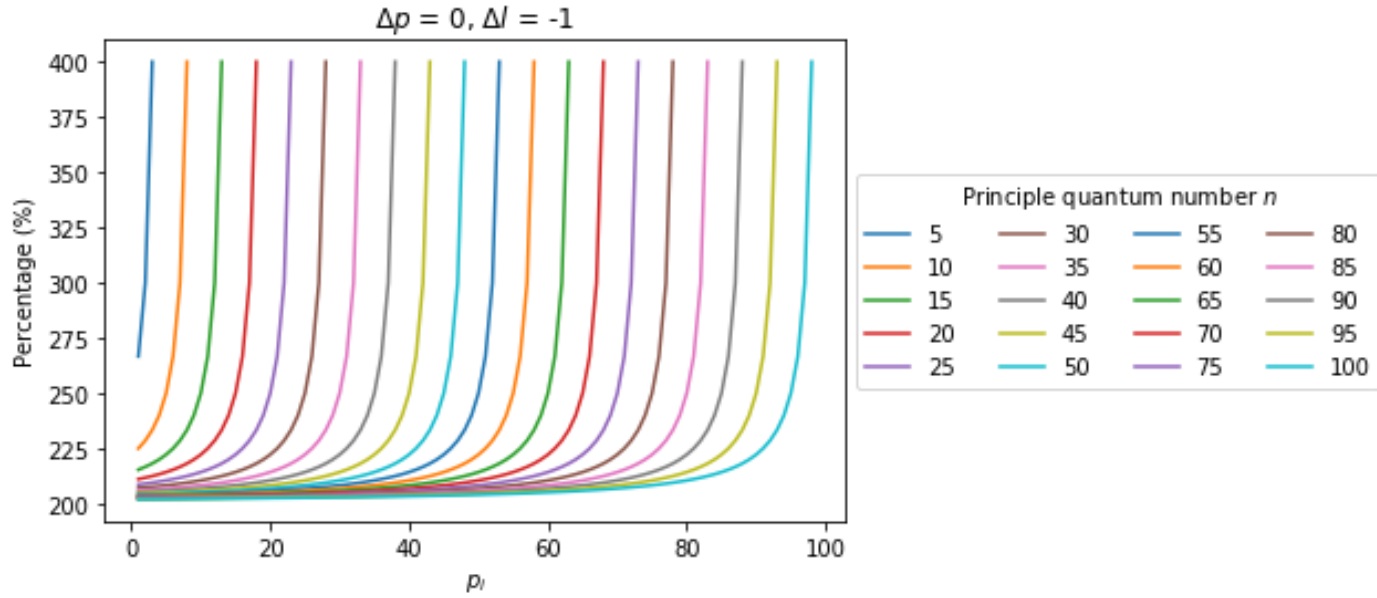


Fig. 1.4.16. State to state transition rates $A_{i,f}$ for $\Delta m = 0$ expressed as a percentage of state to state transition rates $A_{i,f}$ for $\Delta m = \pm 1$ where $n = 5, 10, 15, \dots, 100$, $\Delta l = -1$ and $\Delta p = 0$.

Figure 1.4.16 demonstrates the $\Delta m = 0$ decay channel has a state to state transition rate which is at least 200% greater for all n values assessed here. Furthermore, as p_i approaches its maximum value, the percentage difference in transition rate for all values of n approaches 400%.

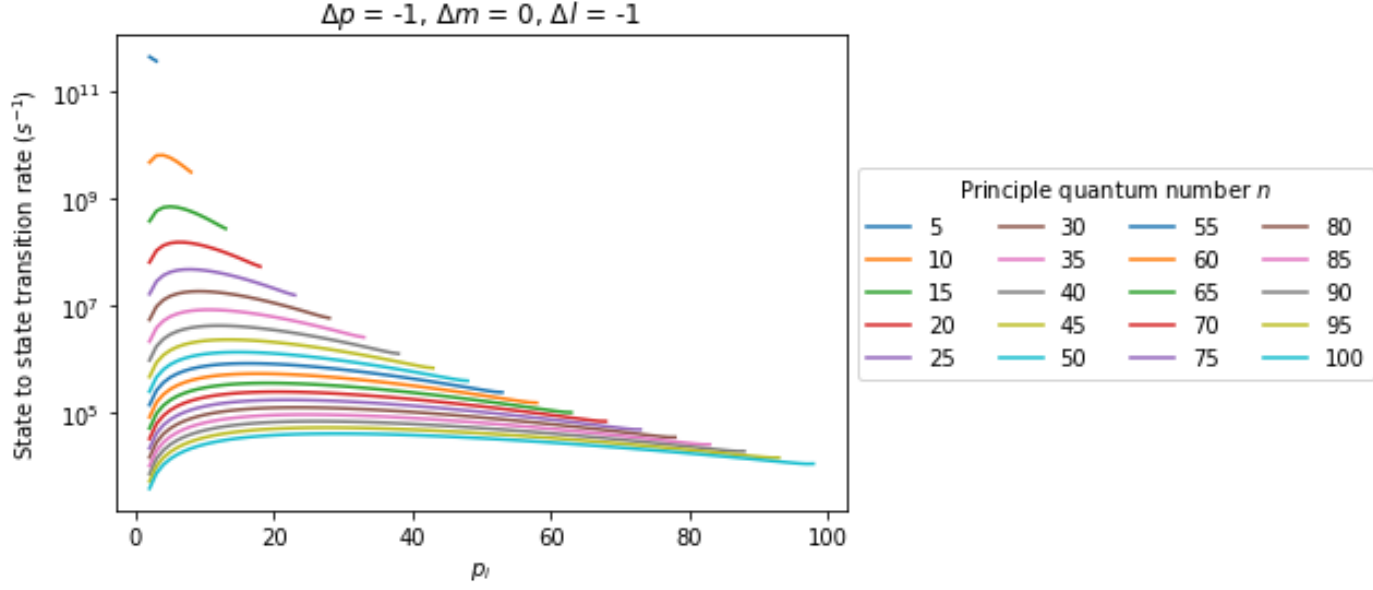


Fig. 1.4.17. State to state transitions rates $A_{i,f}$ as a function of p_i with $n = 5, 10, 15, \dots, 100$ for $m_i = 0, \Delta p = -1, \Delta m = 0$ and $\Delta l = -1$.

Figure 1.4.17 plots the state to state transition rate for various n as a function of p_i when $\Delta p = -1, \Delta m = 0$ and $m_i = 0$. Due to transition rules, only the case where $\Delta l = -1$ can be considered. State to state transition rate decreases as n increases. Except where $n = 5$, state to state transition rate increases with p_i until a maximum transition rate is reached. Further increases in p_i result in a decrease in state to state transition rate, though from $n \geq 25$, the transition rate for higher values of p_i remains above the transition rate for the lowest values of p_i .

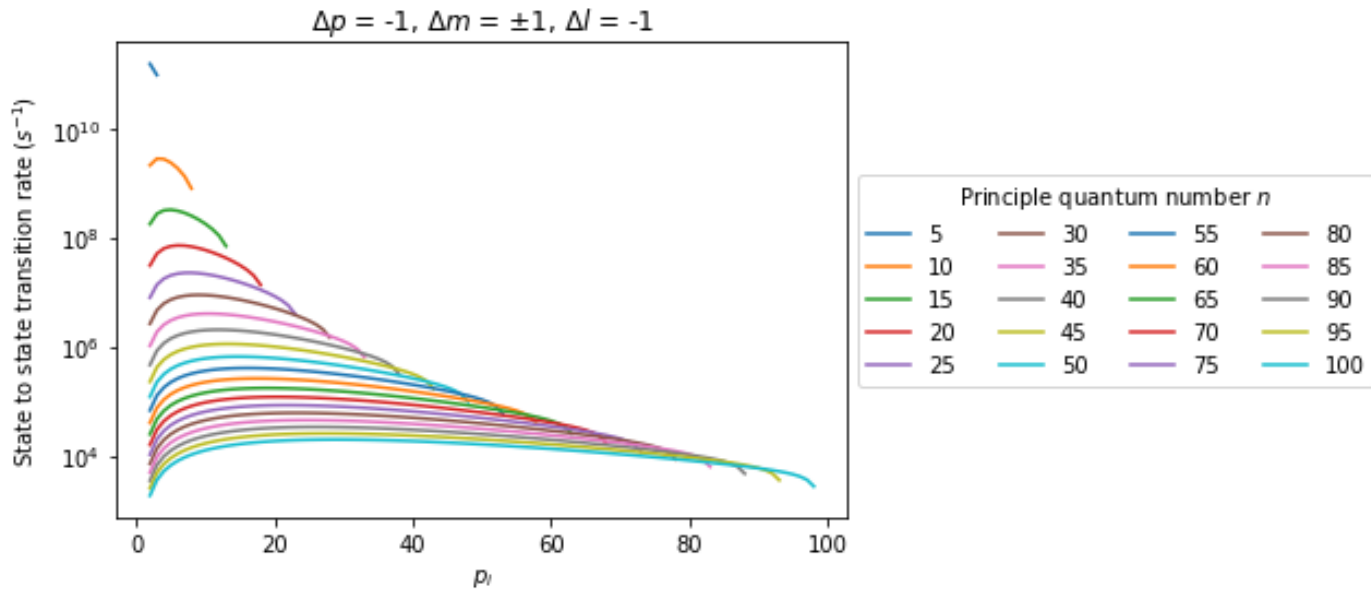


Fig. 1.4.18. State to state transitions rates $A_{i,f}$ as a function of p_i with $n = 5, 10, 15, \dots, 100$ for $m_i = 0, \Delta p = -1, \Delta m = \pm 1$ and $\Delta l = -1$.

Figure 1.4.18 is the exact same plot as figure 1.4.17 except here $\Delta m = \pm 1$. The state to state transition rates is clearly lower in figure 6 compared with figure 5 and a sharp decrease in transition rate for the highest p_i values is present.

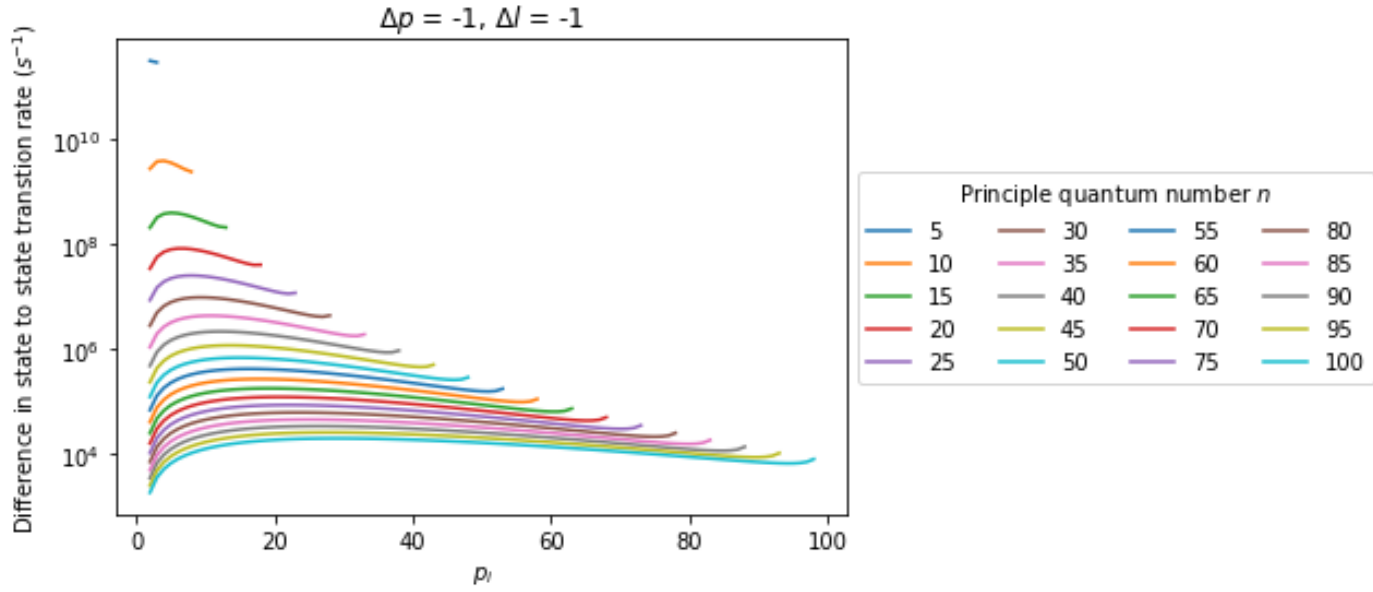


Fig. 1.4.19. Overestimation in state to state transition rates $A_{i,f}$ through using $\Delta m = 0$ to approximate the case where $\Delta m = \pm 1$ for $n = 5, 10, 15, \dots, 100$, $\Delta l = -1$ and $\Delta p = -1$.

Figure 1.4.19 plots the difference in the state to state transition rate between the $\Delta m = 0$ and $\Delta m = \pm 1$ decay channels for $\Delta p = -1$. The state to state transition rate for $\Delta m = 0$ is greater than that for $\Delta m = \pm 1$.

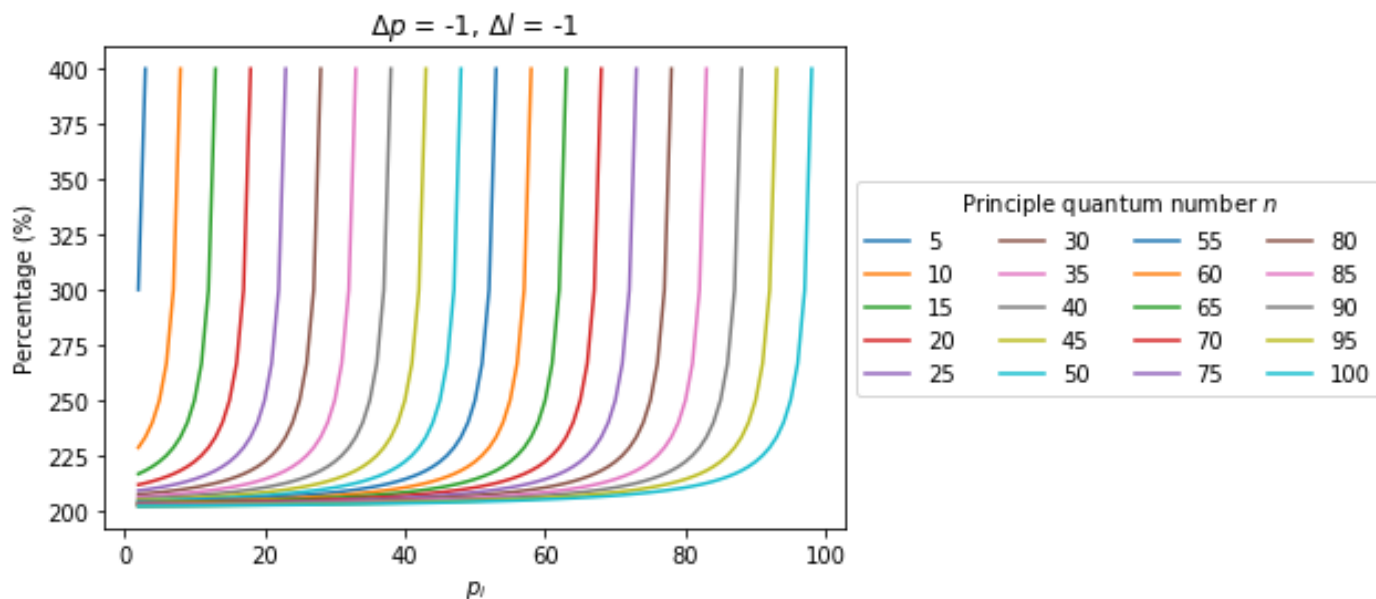


Fig. 1.4.20. State to state transition rates $A_{i,f}$ for $\Delta m = 0$ expressed as a percentage of state to state transition rates $A_{i,f}$ for $\Delta m = \pm 1$ where $n = 5, 10, 15, \dots, 100$, $\Delta l = -1$ and $\Delta p = -1$.

Figure 1.4.20 is almost identical to figure 1.4.16 and again demonstrates that when $\Delta p = -1$, the state to state transition rate for $\Delta m = 0$ is at least 200% greater for all n values when compared to the transition rate for $\Delta m = \pm 1$. Furthermore, as p_i increases, the percentage difference in transition rate for all n reaches the figure of 400% as p_i reaches its maximum value.

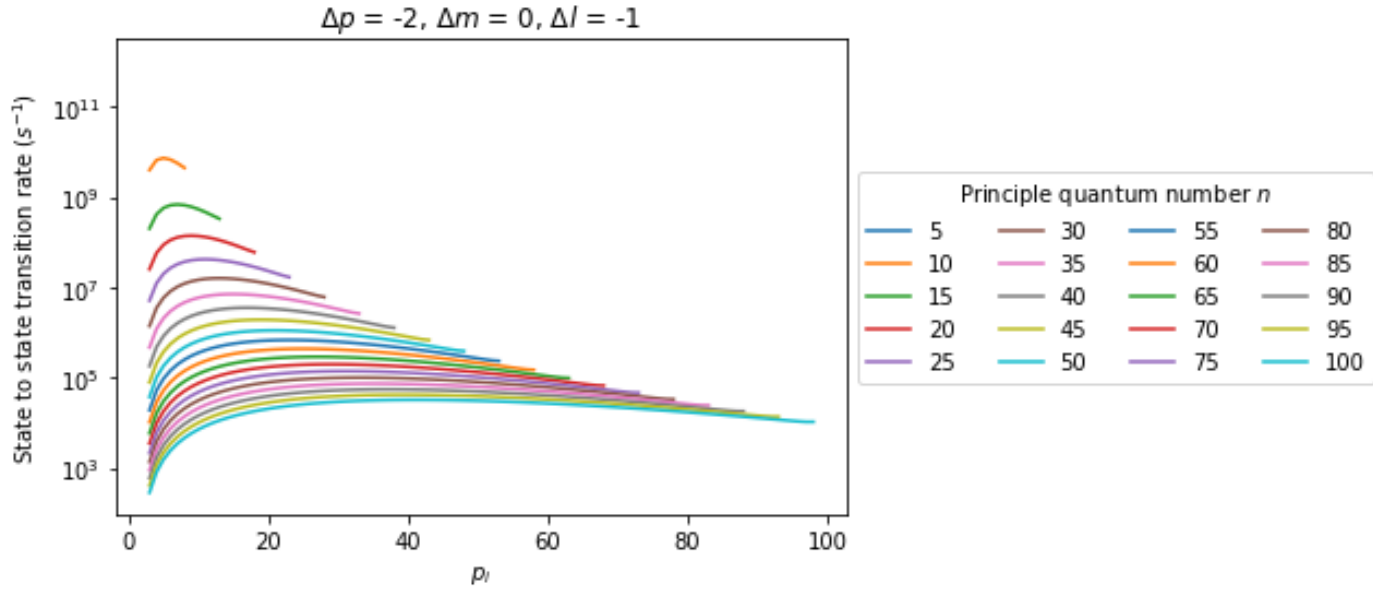


Fig. 1.4.21. State to state transitions rates $A_{i,f}$ as a function of p_i with $n = 5, 10, 15, \dots, 100$ for $m_i = 0, \Delta p = -2, \Delta m = 0$ and $\Delta l = -1$.

Figure 1.4.21 plots the state to state transition rate for various n as a function of p_i when $\Delta p = -2, \Delta m = 0, m_i = 0$, and $\Delta l = -1$. State to state transition rates are lowest for the smallest p_i and a maximum transition rate is reached as p_i increases. However, compared with the above scenarios where $\Delta p = -1$ or 0 , the gradient of the decrease in state to state transition rates is smaller once the maximum transition rate has been reached.

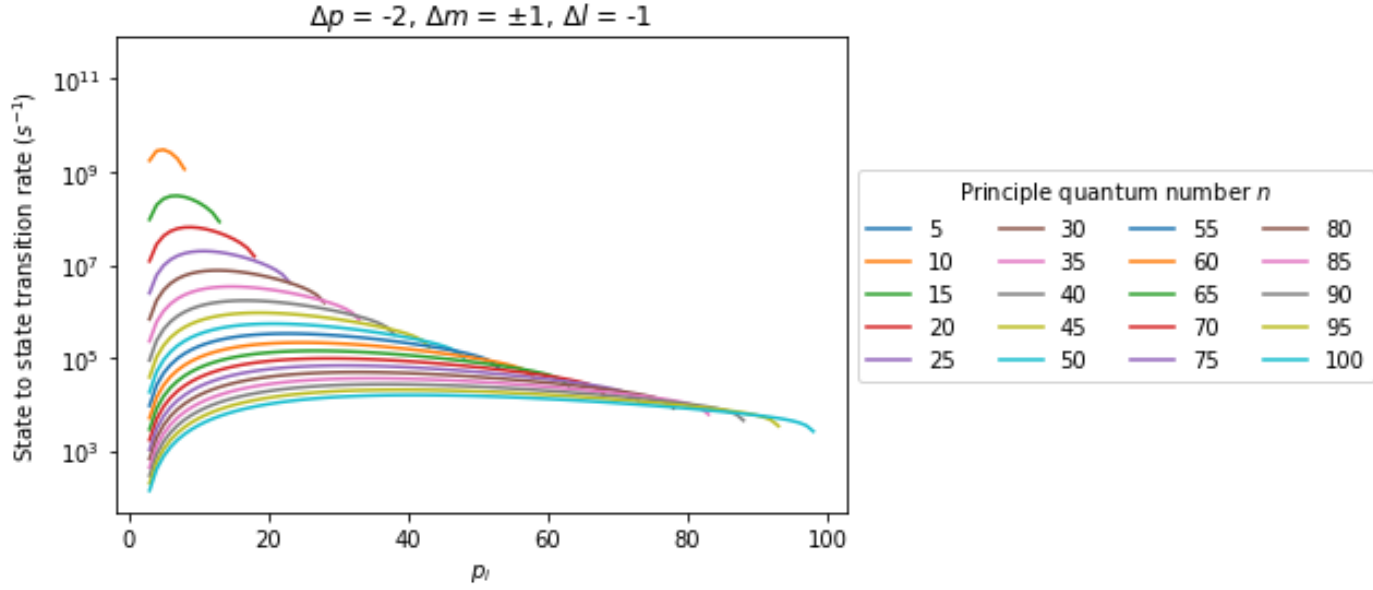


Fig. 1.4.22. State to state transitions rates $A_{i,f}$ as a function of p_i with $n = 5, 10, 15, \dots, 100$ for $m_i = 0, \Delta p = -2, \Delta m = \pm 1$ and $\Delta l = -1$.

Figure 1.4.22 is the exact same plot as figure 1.4.21 except here $\Delta m = \pm 1$. Consistent with figures 1.4.14 and 1.4.18, the state to state transition rate is less for the case where $\Delta m = \pm 1$ when compared to the case where $\Delta m = 0$. The sudden decrease in transition rate for the highest values of p_i is again demonstrated.

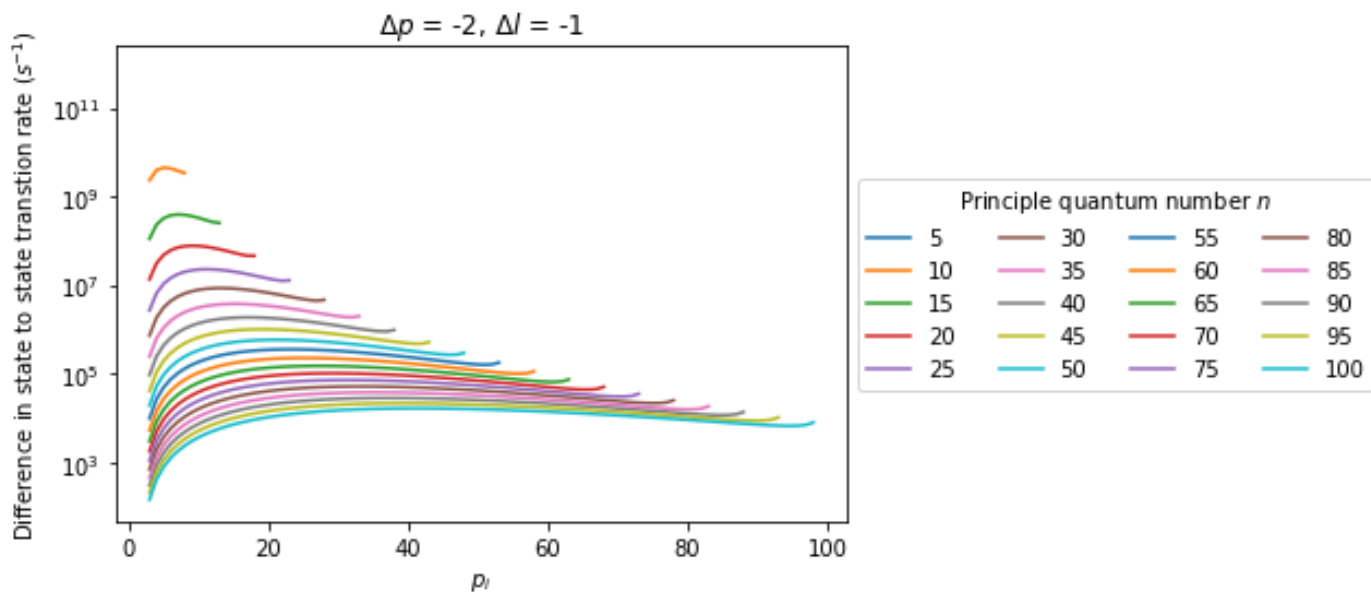


Fig. 1.4.23. Overestimation in state to state transition rates $A_{i,f}$ through using $\Delta m = 0$ to approximate the case where $\Delta m = \pm 1$ for $n = 5, 10, 15, \dots, 100$, $\Delta l = -1$ and $\Delta p = -1$.

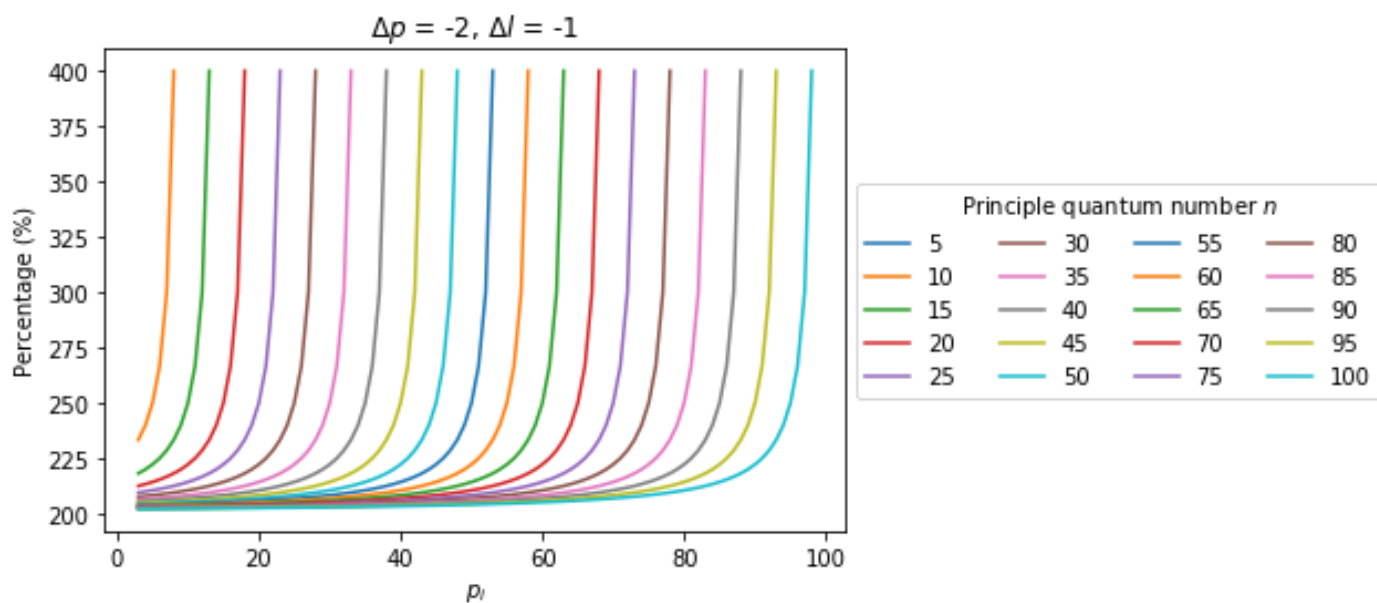


Fig. 1.4.24. State to state transition rates $A_{i,f}$ for $\Delta m = 0$ expressed as a percentage of state to state transition rates $A_{i,f}$ for $\Delta m = \pm 1$ where $n = 5, 10, 15, \dots, 100$, $\Delta l = -1$ and $\Delta p = -1$.

Figure 1.4.23 shows the difference between the state to state transition rate for the $\Delta m = 0$ and $\Delta m = \pm 1$ decay channels for $\Delta p = -2$ and $\Delta l = -1$. Consistent with figures 1.4.15 and 1.4.19, the transition rate is significantly higher for the $\Delta m = 0$ decay channel. Figure 1.4.24 considers the state to state transition rate for the $\Delta m = 0$ decay channel as a percentage of the transition rate for the $\Delta m = \pm 1$ decay channels. Again, the results are extremely consistent with the results in figures 1.4.16 and 1.4.20 with transition rates starting at $\sim 200\%$ greater for the $\Delta m = 0$ decay channel. For maximal p_i associated with each n , the transition rates are consistently 400% greater for the $\Delta m = 0$ decay channel.

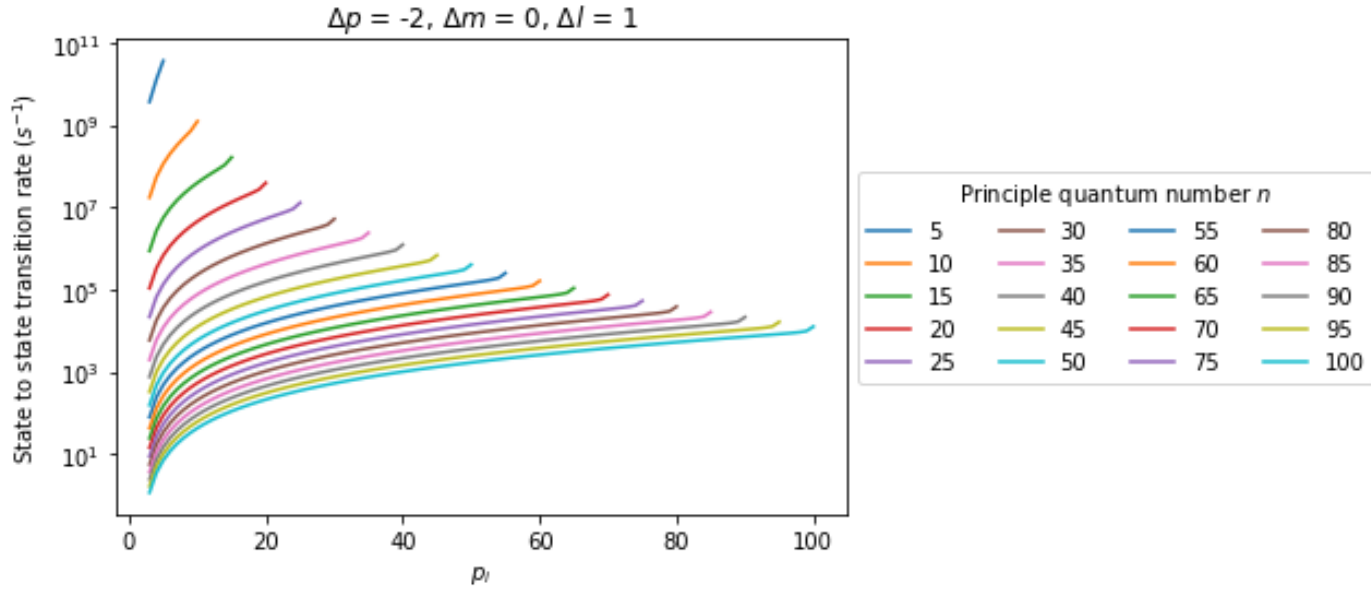


Fig. 1.4.25. State to state transitions rates $A_{i,f}$ as a function of p_i with $n = 5, 10, 15, \dots, 100$ for $m_i = 0$, $\Delta p = -2$, $\Delta m = 0$ and $\Delta l = 1$.

Figure 1.4.25 plots the state to state transition rate for various n as a function of p_i when $\Delta p = -2$, $\Delta m = 0$, $m_i = 0$, and $\Delta l = 1$. This plot is consistent with the results found by Whinray and Ernest [1] with state to state transitions decreasing as n increases and increasing as p_i

increases. This contrasts with previous related figures 1.4.13, 1.4.17 and (especially) 1.4.21 where transition rates would peak before decreasing. A sudden increase in state to state transition rate is present for maximal p_i due to a sharp maximum in the polar spread of the spherical harmonic, as previously found by Whinray and Ernest [1].

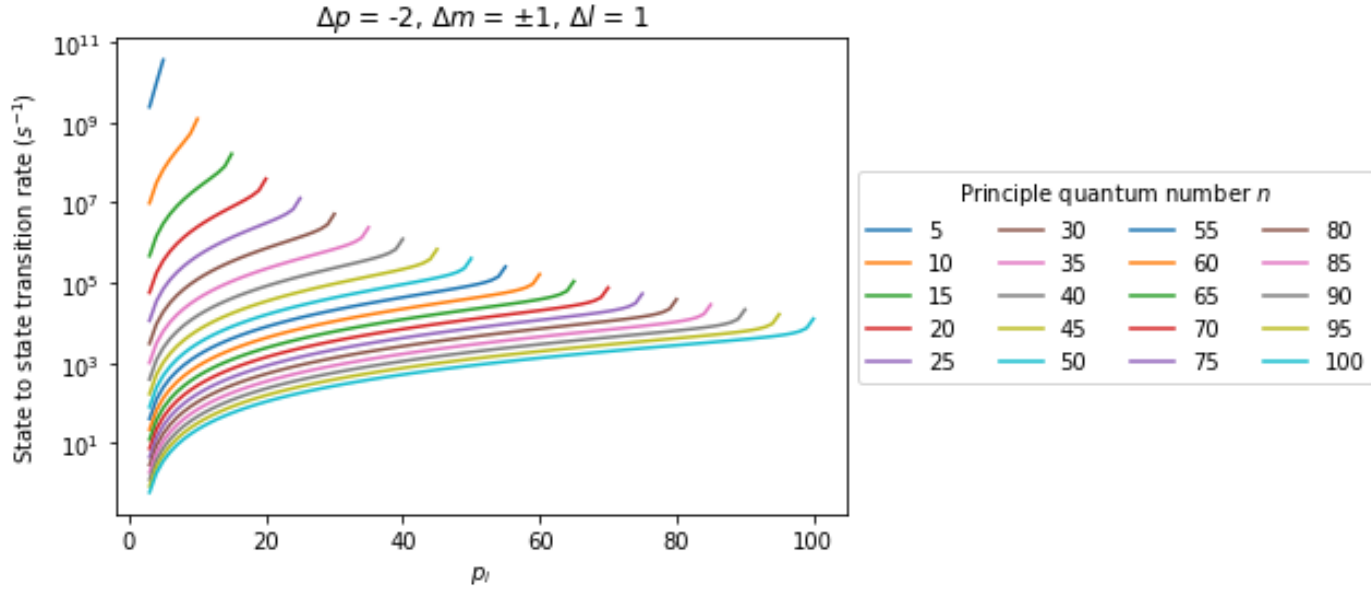


Fig. 1.4.26. State to state transitions rates $A_{i,f}$ as a function of p_i with $n = 5, 10, 15, \dots, 100$ for $m_i = 0$, $\Delta p = -2$, $\Delta m = \pm 1$ and $\Delta l = 1$.

Figure 1.4.26 is the same as figure 1.4.25 except here $\Delta m = \pm 1$. The state to state transition rate is less when compared to figure 1.4.25 though it is not as obvious as previous similar cases. Most pronounced is the sharp increase in state to state transition rate for maximum levels of p_i , which is contrary to previous related plots in figures 1.4.14, 1.4.18 and 1.4.22.

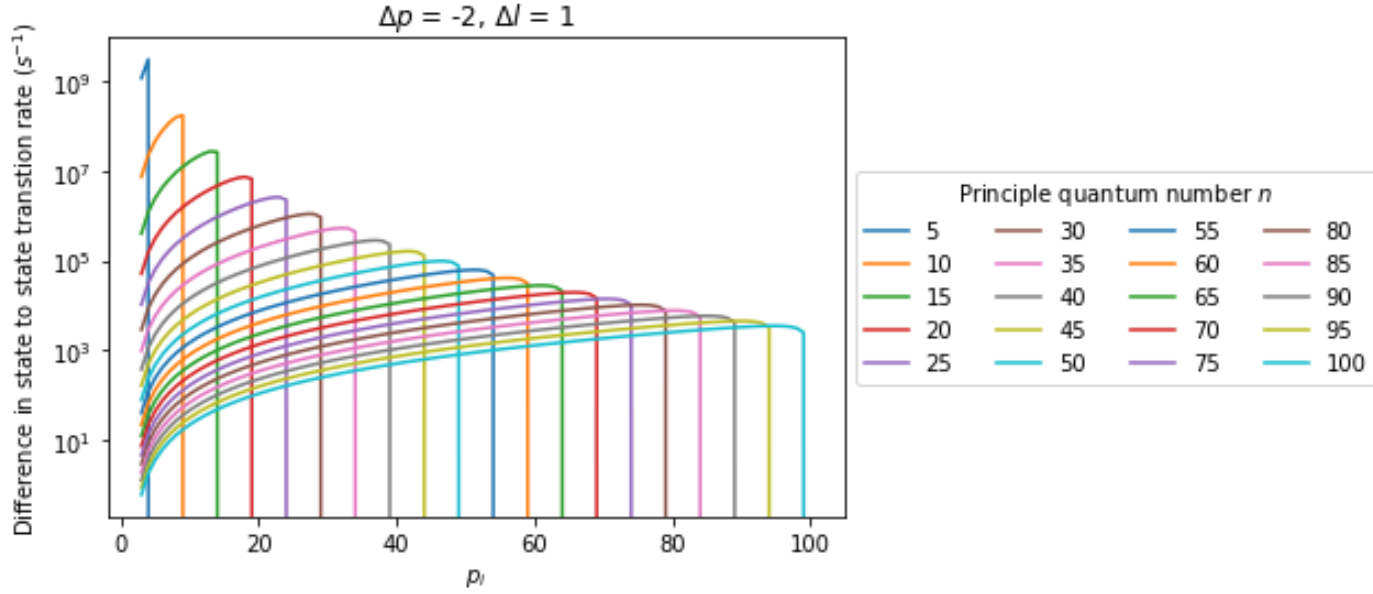


Fig. 1.4.27. Overestimation in state to state transition rates $A_{i,f}$ through using $\Delta m = 0$ to approximate the case where $\Delta m = \pm 1$ for $n = 5, 10, 15, \dots, 100$, $\Delta l = 1$ and $\Delta p = -2$.

Figure 1.4.27 plots the difference in the state to state transition rate between the $\Delta m = 0$ and $\Delta m = \pm 1$ decay channels for $\Delta p = -2$ and $\Delta l = 1$. Consistent with previous results in figures 1.4.15, 1.4.19 and 1.4.23, the state to state transition rate for the $\Delta m = 0$ decay channel is greater for almost all p_i . However, for maximal p_i , there is no difference between the transition rate for the $\Delta m = 0$ and $\Delta m = \pm 1$ decay channels. The sharp increase in decay rate demonstrated in figure 1.4.26 means the transition rate at maximum p_i becomes equal for the two cases.

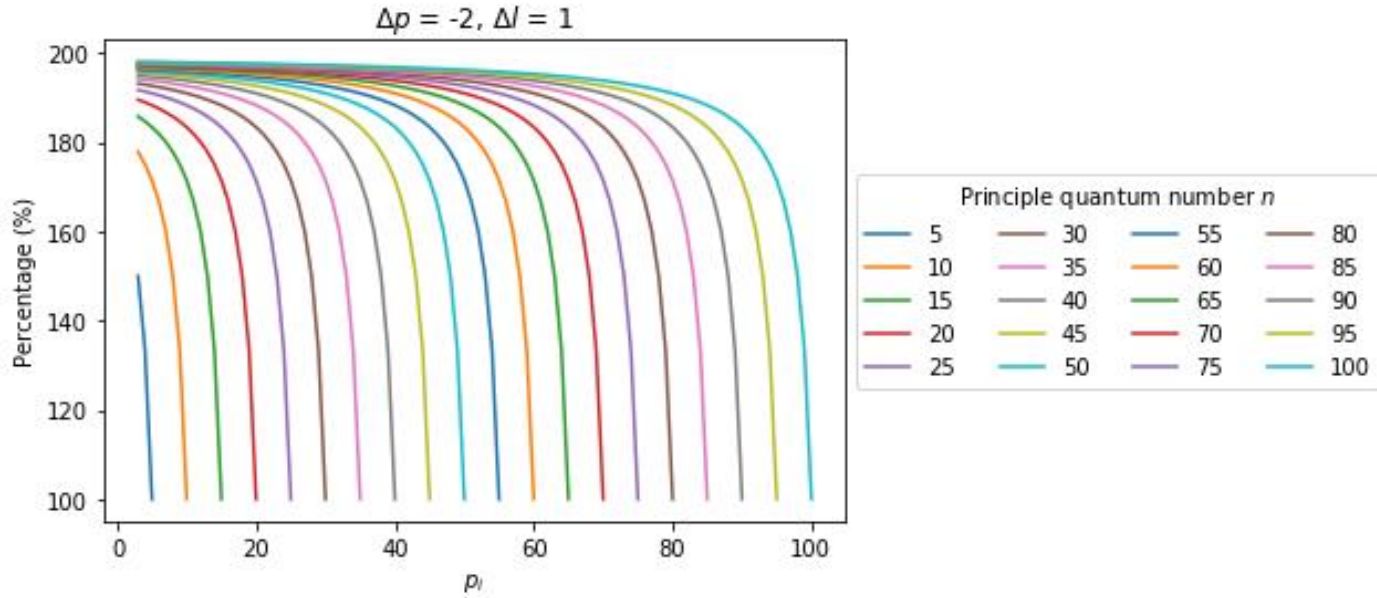


Fig. 1.4.28. State to state transition rates $A_{i,f}$ for $\Delta m = 0$ expressed as a percentage of state to state transition rates $A_{i,f}$ for $\Delta m = \pm 1$ where $n = 5, 10, 15, \dots, 100$, $\Delta l = 1$ and $\Delta p = -2$.

Figure 1.4.28 plots the state to state transition rate for $\Delta m = 0$, $\Delta l = 1$ and $\Delta p = -2$ as a percentage of the case where $\Delta m = \pm 1$. Figure 1.4.28 demonstrates the transition rate for the $\Delta m = 0$ decay channel is greater than the transition rate for the $\Delta m = \pm 1$ decay channels for all p_i , except for maximal p_i relative to n when the transition rates become equivalent. The difference in state to state transition rate decreases as p_i increases and the percentage difference between the two cases approaches a maximum of 200%. This contrasts with similar plots in figures 1.4.16, 1.4.20 and 1.4.24 where the maximal difference in decay rate was $\sim 400\%$ and increased for increasing p_i .

1.4.3) Results for state lifetimes:

The results here are produced from methods section 1.3.7, “State lifetimes”.

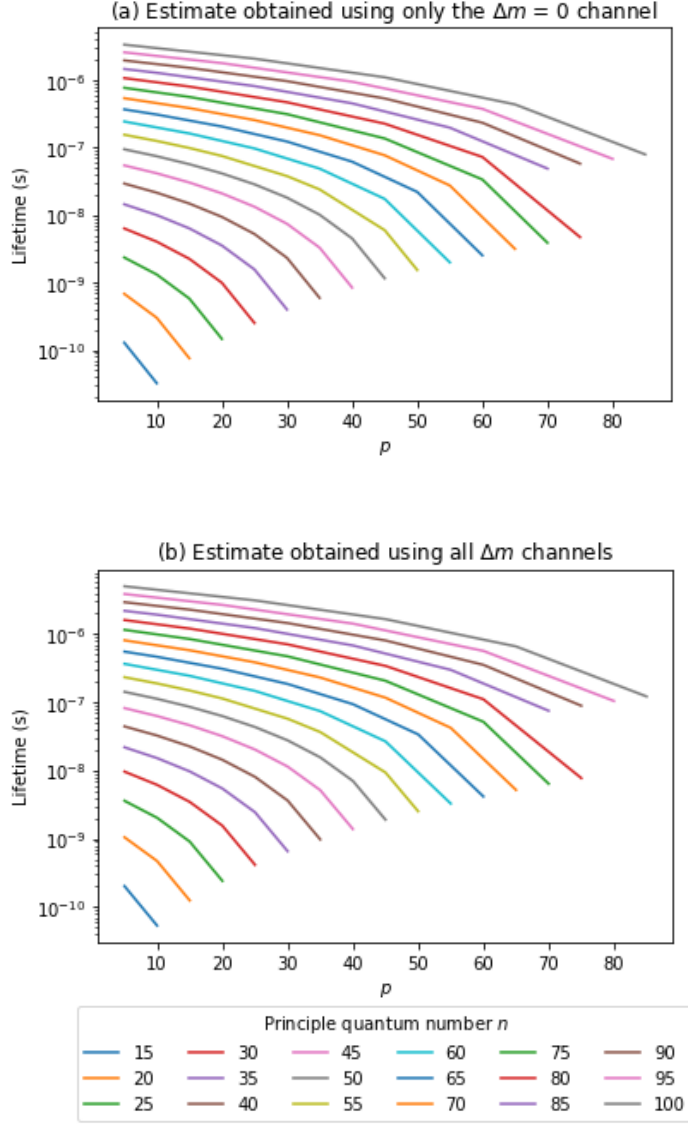


Fig. 1.4.29. State lifetimes for $n = 15, 20, 25, \dots, 100$ as a function of p . (a) Lifetimes estimated by only using the $\Delta m = 0$ decay channel. (b) Lifetimes found by considering all Δm decay channels.

Figure 1.4.29 plots state lifetimes as a function of p for various n . Figure 1.4.29(a) reproduces and confirms previous work by Whinray and Ernest (2018) who used the decay rate for the $\Delta m = 0$ channel multiplied by three to estimate the sum of the decay rate through all Δm channels. The inverse of the estimated sum of the decay rate through all Δm decay

channels was then taken to estimate state lifetimes. Figure 1.4.29(b) uses the inverse of the sum of the decay rates for all Δm decay channels to calculate state lifetimes. Significantly, the state lifetimes are underestimated for all cases of n and p in figure 1.4.29(a).

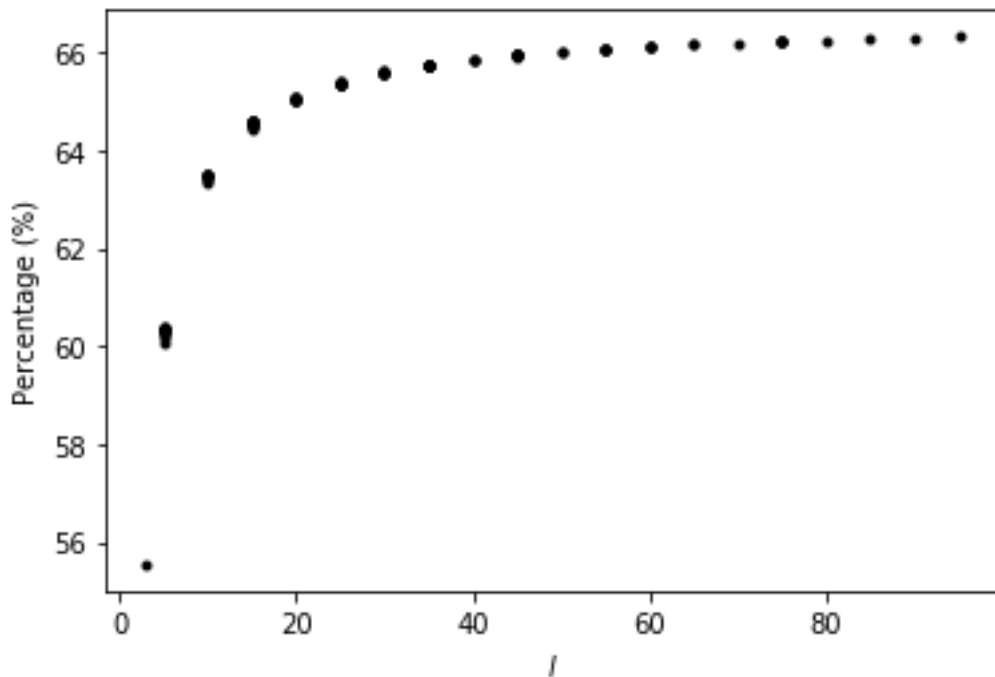


Fig. 1.4.30. Scatter plot of estimated state lifetime (using $\Delta m = 0$ decay channel) as a percentage of actual state lifetime, plotted as a function of l .

Figure 1.4.30 shows how well lifetimes are estimated using only the $\Delta m = 0$ decay channel. Estimated state lifetimes were found to lie between ~55-67% of state lifetimes calculated using all Δm decay channels.

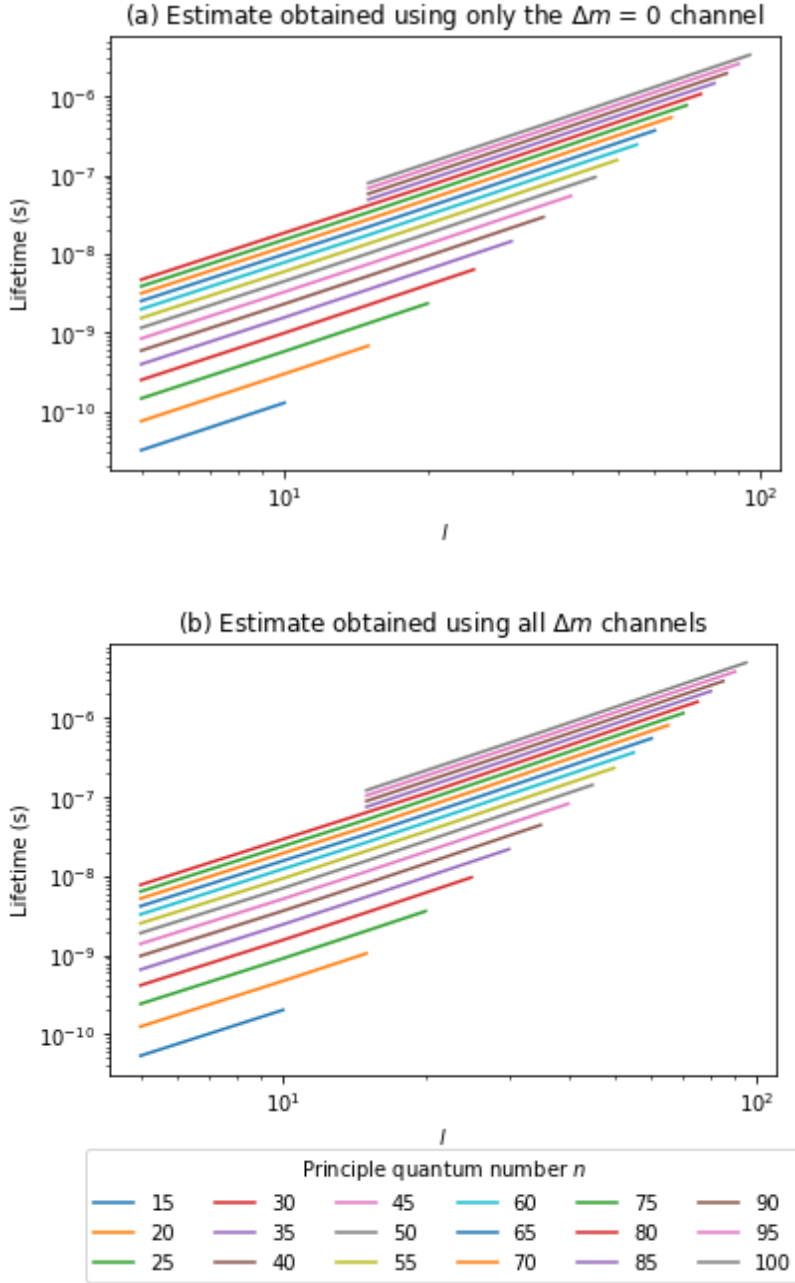


Fig. 1.4.31. Log-log plot of state lifetimes for $n = 15, 20, 25, \dots, 100$ as a function of l . (a) Lifetimes estimated by only using the $\Delta m = 0$ decay channel. (b) Lifetimes found by considering all Δm decay channels.

Whinray and Ernest [1] previously reported an empirical relationship between state lifetimes ' τ ' and l where $\tau \propto l^\beta$ and $\beta = 2.009 \pm 0.004$. This result has been reproduced and confirmed

in figure 1.4.31(a). However, Whinray and Ernest [1] only estimated state lifetimes using the $\Delta m = 0$ decay channel. Figure 1.4.31(b) shows state lifetimes calculated using all Δm decay channels. For the values of n and l studied in figure 3(b), it has been found that $\beta = 1.995 \pm 0.043$. This result agrees with Whinray and Ernest [1], however it suggests a greater degree of spread in β when all Δm decay channels are included. Accordant with figures 1.4.29 and 1.4.30, the state lifetimes are always greater when calculated for all Δm decay channels.

(Examiners: Please see appendix k1 to k4 to view Python coding examples to analyse data and produce graphs above).

1.5) Discussion:

This study applied the mathematical framework provided by the Schrödinger equation for weak gravity to investigate the effect of the quantum eigenvalue m on state to state transition rates and lifetimes of gravitational eigenstates in non-relativistic regions of deep gravitational wells. Both the effect of the change in m (Δm) and $q_i (\equiv l_i - |m_i|)$ were assessed. Whenever $\Delta m = 0$, $\Pi_{ifx} = \Pi_{ify} = 0$, so only the Π_{ifz} component of the dipole matrix element Π_{if} needs to be calculated in equation (1.15) to evaluate state to state transition rates.

Furthermore, when $m_i = 0$, the spherical harmonic component $Y_{l,m}$ (equation 1.9) of Π_{if} is simpler. For this reason, previous studies set $m_i = 0$ and only considered the $\Delta m = 0$ decay channel when studying empirical relationships of state to state transition rates and state lifetimes of gravitational eigenstates [1]. However, quantification of how well these empirical relationships apply to other m_i and other Δm decay channels was lacking.

For the values assessed here, the sum of the state to state transition rates for all three Δm decay channels was found to be constant regardless of the choice of q_i . This profound result is demonstrated in figures 1.4.1 - 1.4.11. So, when calculating the lifetime of a state with a combination of n_i , l_i , and m_i , any convenient number can be chosen to replace m_i provided all possible Δm decay channels are summed. Significantly, this result is true for all systems where quantum mechanics is applied and is not limited to the study of gravitational eigenstates. If m_i is set at 0, computation time of state to state transitions is reduced. However, this result is only proven here for the quantum eigenvalues evaluated as per methods section 1.3.2. Ideally, future research will prove the generality of this result through analytical analysis.

The state to state transition rate was found to depend strongly on the combination of Δl , Δm and m_i as shown in figures 1.4.1 – 1.4.11. Previous empirical research into state to state transition rates of gravitational eigenstates set $m_i = 0$ and used only the $\Delta m = 0$ decay channel [1]. Fortunately, it has been found that when q_i is maximal (so $m_i = 0$), the state to state transition rate for the $\Delta m = 0$ decay channel is significantly larger than the state to state transition rate for the $\Delta m = 1$ and the $\Delta m = -1$ decay channels. Future research can use this finding to constrain the maximal possible state to state transition rate if m_i is set to 0.

Table 1.4.1 shows regions where the transition rate for the $\Delta m = 0$ decay channel most accurately reflects the transition rate for the non-zero Δm decay channels. In particular, when $\Delta m \Delta l = -1$, the best estimate provided by the $\Delta m = 0$ decay channel for the transition rate of the non-zero Δm decay channels occurs when $m_i/l_i = 1/3$. Conversely, when $\Delta m \Delta l = 1$, the best estimate for the transition rate for the non-zero Δm decay channels is provided by the

transition rate for the $\Delta m = 0$ decay channel when $m_i/l_i = -1/3$. This suggests values of m_i where time can be saved through only calculating the transition rate for the $\Delta m = 0$ decay channel. Similarly, table 1.4.2 shows multiplying the transition rate for the $\Delta m = 0$ decay channel by three in order to estimate the sum of the transition rate for all Δm decay channels is shown be most accurate when m_i is $\sim 40\text{-}42\%$ of q_i . This result suggests future research could use the inverse of three times the transition rate for the $\Delta m = 0$ decay channel when m_i is $40\text{-}42\%$ of q_i to obtain an accurate estimate of a state lifetime. This is particularly useful as quantum eigenvalues increase and calculating the transition rates for the $\Delta m = -1$ and $\Delta m = 1$ decay channels quickly becomes impractical. However, as these are empirical findings, extrapolation to quantum eigenvalues not explored here needs to be approached with caution.

As a direct extension of Whinray and Ernest [1], state to state transition rate as a function of p_i was broadened to include the non-zero Δm decay channels. In this study, if the calculation of a transition rate for a given state through the $\Delta m = 0$ decay channel took one hour, the same calculation through a non-zero Δm decay channel was found to take approximately ten hours. This is presented as evidence for the necessity to be able to constrain transition rates for the non-zero Δm decay channels by only calculating the transition rate for the $\Delta m = 0$ decay channel.

In all results presented in section 1.4.2, whenever $m_i = 0$, the state to state transition rate is the same for the $\Delta m = -1$ and $\Delta m = 1$ decay channels. Thus, if completely accurate state to state transition rates are needed for a state with $m_i = 0$, only the $\Delta m = 0$ decay channel and one of the non-zero Δm decay channels needs to be calculated. The results presented in section 1.4.1 indicated that when $m_i = 0$, the transition rate for the $\Delta m = 0$ decay channel would

exceed that of the $\Delta m = -1$ and $\Delta m = 1$ decay channels. The results presented in section 1.4.2 indicate that this is indeed the case. The general shape and trends of state to state transition rate as a function of p_i previously demonstrated for the decay channel $\Delta m = 0$ [1] are clearly demonstrated for the non-zero Δm decay channels, with some important differences.

When $\Delta l = -1$, the $\Delta m = 0$ decay channel shows a sharp increase in state to state transition rate when approaching maximal p_i due to a sharp maximum in the polar spread of the spherical harmonic. However, when $\Delta m = \pm 1$, the transition rate undergoes a sharp decrease at maximum p_i levels. Using the $\Delta m = 0$ decay channel to estimate transition rates through the non-zero Δm decay channels resulted in an overestimation of at least 200%, which increases to 400% for maximum p_i .

The $\Delta l = 1$ decay channel similarly showed the transition rate for the $\Delta m = 0$ decay channel was around twice as high as the transition rate through the non-zero Δm decay channel up to p_i of around 80% of n_i . However, once p_i approaches its maximum value, the difference in the transition rates between the $\Delta m = 0$ and non-zero Δm decay channels falls to 0%. These results show that the decrease in transition rate due to the sharp maximum in the polar spread of the spherical harmonic is greater in the non-zero Δm decay channels.

Whinray and Ernest [1] estimated total state lifetimes by setting m_i to 0 and evaluating the inverse of the transition rate for the $\Delta m = 0$ decay channel multiplied by three. From the results in section 1.4.1, it is reasonable to extrapolate that total state lifetime is independent of m_i . However, since state to state transition rates have been shown in sections 1.4.1 and 1.4.2 to depend heavily on the Δm decay channel, total state lifetimes were calculated in this paper

for all Δm decay channels with m_i set to 0. For the quantum eigenvalues evaluated here, state lifetimes estimated by Whinray and Ernest [1] account for ~55.5% to ~66% of true state lifetimes with lower l values associated with a greater degree of underestimation. Whinray and Ernest [1] reported an empirical relationship for state lifetimes as $\tau \propto n^3 l^\beta$ where $\beta = 2.009 \pm 0.004$. Here it was found that $\beta = 1.995 \pm 0.043$ where the error reflects the standard deviation in the value of β . Whinray and Ernest [1] considered lifetimes for n of up to 400. Here n was only considered up to 100 due to the time taken to calculate non-zero Δm decay channels. It is unclear whether this contributed to the increased error in the value of β or if it has something to do with the decay channels themselves.

1.5.1) Implications:

This investigation supports previous research demonstrating gravitational eigenstates become increasingly dark as n_i increases and as p_i becomes a small portion of n_i [1, 10, 11]. It has been shown that previous empirical research using only the $\Delta m = 0$ decay channel has underestimated the stability of gravitational eigenstates. Thus, previous research acts as an upper constraint to state to state transition rates and a minimal constraint for total state lifetimes.

The main difficulty in studying QDM is the time required for evaluation of relevant overlap integrals due to the extreme quantum numbers required. Calculating overlap integrals at $n \sim 10^{31} - 10^{34}$ is required to be reflective of galactic halos and is not plausible with current computer technology. Analytical methods have only found approximate methods for all but a few tractable scenarios. Hence recent research has focused on attempting to find an empirical relationship to estimate state to state transition rates and total state lifetimes. However, even

calculating state to state transition rates for n of up to 2000 presents time consuming computational challenges.

Besides supporting previous research [1, 10, 11] and by association supporting the theory of QDM, this investigation places limits on what can be ascertained from simplifying calculations to only considering the $\Delta m = 0$ decay channel. Provided q_i is maximum, the $\Delta m = 0$ decay channel will provide a constraint on the maximal transition rate for all Δm decay channels. This can also be extended to the study of total state lifetimes where the $\Delta m = 0$ decay channel can be used to constrain the lower limit for expected lifetimes.

Whilst the aim of this investigation was to formally test the impact of m_i and Δm in the theory of QDM, the results are true for all quantum mechanical systems in spherically symmetric Coulomb-type potentials. Possibly most significant is the finding that the sum of state to state transition rates for all possible Δm channels is constant. However, due to the empirical nature of this investigation, the extension of the relationships beyond the quantum numbers studied here should be approached with caution. Ideally an analytical approach is required to prove the generality of the results presented here.

1.6) References

- [1] T. A. Whinray and A. D. Ernest, "Relations between transition rates and quantum numbers in gravitational potentials," *Grav. Cosmol.* **24**, 97 (2018).
- [2] I. A. Yegerova, A. Babic, P. Salucci, K. Spekkens and A. Pizzella, "Rotation curves of luminous spiral galaxies," *Astron. Nachr.* **332**, 846 (2011).

- [3] A. S. Bolton, S. Burles, L. V. E Koopmans, T. Treu, R. Gavazzi, L. A. Moustakas, R. Wayth and D. J. Schlegel, “The Sloan Lens ACS survey. V. The full ACS strong-lens sample,” *Astrophys. J.* **682**, 964 (2008).
- [4] D. Harvey, R. J. Massey, T. D. Kitching, A. M. Taylor and E. R. Tittley, “The non-gravitational interactions of dark matter in colliding galaxy clusters,” *Science* **347** 1261381 (2015).
- [5] E. Di Valentino, E. Giusarma, M. Lattanzi, A. Melchiorri and O. Mena, “Axion cold dark matter: status after Planck and BICEP2,” *Phys. Rev. D* **90** 043534 (2014).
- [6] T. M. Undagoitia and L. Rauch, “Dark matter direct-detection experiments,” *J. Phys. G. Nucl. Part. Phys.* **43** 013001 (2015).
- [7] D. I. Clowe, M. Bradac, A. H. Gonzalez, M. Markevitch, S. W. Randall, C. Jones and D. Zaritsky , “A direct empirical proof of the existence of dark matter,” *Astrophys. J. Lett.* **648**, L109 (2006).
- [8] N. E. Mavromatos, M. Sakellariadou and M. F. Yusaf, “Can the relativistic field theory version of modified Newtonian dynamics avoid dark matter on galactic scales?,” *Phys. Rev. D* **79** 081301 (2009).
- [9] A. D. Ernest and M. P. Collins, “Structural features of high-n gravitational eigenstates,” *Grav. Cosmol.* **18**, 242 (2012).
- [10] A. D. Ernest, “Gravitational eigenstates in weak gravity I: dipole decay rates of charged particles,” *J. Phys. A: Math. Theor.* **42** 115207 (2009).
- [11] A. D. Ernest, “Gravitational eigenstates in weak gravity II: further approximate methods for decay rates,” *J. Phys. A: Math. Theor.* **42** 115208 (2009).

- [12] H. Zbinden, J. Brendel, W. Tittel and N Gisin, “Experimental test of relativistic quantum state collapse with moving reference frames,” *J. Phys. A Math. Theor.* **34**, 7103 (2001).
- [13] J. R. Friedman, V. Patel, W. Chen, S. K. Tolpygo and J. E. Lukens, “Quantum superposition of macroscopic states,” *Nature* **406**, 43 (2000).
- [14] M. H. Anderson, J. R. Ensher, M. R. Matthews, C. E. Wieman, and E. A Cornell, “Observation of Bose-Einstein condensation in dilute atomic vapour,” *Science* **269**, 198 (1995).
- [15] V. V. Nesvizhevsky, H. G. Börner and A. K. Petukhiv, “Quantum states of neutrons in the Earths gravitational field,” *Nature* **415**, 297 (2002).

Paper 2: Relations between binding energy, central mass and transition rates of charged particles held in gravitational eigenstates in non-relativistic regions of deep gravitational wells.

2.1) Abstract:

This paper extends the theoretical quantum dark matter model which predicts baryons and electrons held in eigenstates by deep gravitational wells can exhibit small interaction cross sections due to the composition of the gravitational eigenspectrum of their wave functions. In this paper, the effect of the central mass on the electromagnetic state to state transition rates (Einstein A coefficients) of gravitational eigenstates was examined. Two binding energies, -172 eV and -344 eV, were held constant as the central mass was varied. A relationship was found between the decay A and the central mass M. In particular given two state to state transition rates A_1 and A_2 that correspond to the same initial value of p ($= p_i \equiv n_i - l_i$) and same Δp ($\equiv \Delta n - \Delta l$), and two corresponding central mass values M_1 and M_2 , it was found that $A_2 \approx A_1 \left(\frac{M_2}{M_1}\right)^{\Delta p-1} \approx A_1 \left(\frac{n_2}{n_1}\right)^{\Delta p-1}$, where n_1 and n_2 are the initial n values corresponding to the specific energy used. This finding agrees with the quantum dark matter model by showing the state to state transition rate for particles held in gravitational eigenstates decreases markedly as n increases and represents a step forward in estimating state to state transition rates for large values of n and l which are otherwise impractical to calculate. Significantly, this paper supports previous research showing there exists a theoretical set of high n and relatively high l gravitational eigenstates with dark matter properties.

Abstract Length: 17 lines (maximum allowed is 20 lines)

Character count of article: 28 632 (maximum allowed is 40 000).

2.2) Introduction:

Whilst postulations about the existence of non-luminous matter can be traced back to at least the 18th Century, significant dynamical astronomical investigations suggestive of dark matter were first completed in the 1930's [1]. It wasn't until the 1970's, when strong evidence for the flat rotation curves across many galaxies was found, that the 'dark matter problem' gained widespread attention [2, 3]. Robust independent sources of evidence for dark matter now exist including galaxy/cluster collisions [4], gravitational lensing studies [5] and cosmic microwave background constraints on parameters of Lambda Cold Dark Matter (Λ CDM) [6].

Λ CDM is the most cited cosmological interpretation of the universe, largely due to its success in predicting and describing many astrophysical phenomena. However, more than 30 years of concentrated effort has failed to find unambiguous experimental evidence for a particle to account for the dark matter component of Λ CDM [7, 8]. Λ CDM faces many other well-known challenges. For example, the cuspy halo problem [9], the missing satellites problem [10] and the angular momentum catastrophe [11].

Modified Newtonian Dynamics and other alternative theories of gravity have also been postulated as solutions to the 'dark matter problem'. However, an alternative theory of gravity explaining all observed 'dark matter phenomena' is presently absent [12, 13]. The absence of experimental evidence for a dark matter particle and the absence of a viable alternative theory of gravity justifies continued theoretical investigation into the possible constituents of dark matter.

The quantum dark matter (QDM) theory applies quantum mechanics to particles held in eigenstates by deep gravitational wells. As a result of the scale of quantum numbers involved, gravitational eigenstates can have extreme Rydberg atom like properties. The states of interest are those with high total angular momentum l relative to the principle quantum number n . Theoretical studies have indicated these gravitational eigenstates have extremely low interaction cross sections and long lifetimes which has led to them being proposed as dark matter candidates [14-17].

Application of quantum mechanics to systems where gravity becomes the primary binding energy is novel. However, gravitational eigenstates have been shown to exist [18] which suggests quantum theory can be applied to gravity the same way it is applied to other potentials. Furthermore, there is no formal reason to limit the application of quantum mechanics based on the size of the phenomena. Indeed, macroscopic application of quantum theory has been theoretically and experimentally established e.g. superluminal connection of entangled particles over many kilometres [19] and Bose-Einstein condensates [20].

The development of the theory surrounding QDM faces many technical mathematical difficulties. Except for a few tractable scenarios, the extreme value of quantum numbers required at galactic scales means calculating the state to state transition rate for a given gravitational eigenstate is often impractical. General solutions to the overlap integrals for state to state transition rates have been found, however their direct application is also limited due large summations which cannot, in general, be truncated [14].

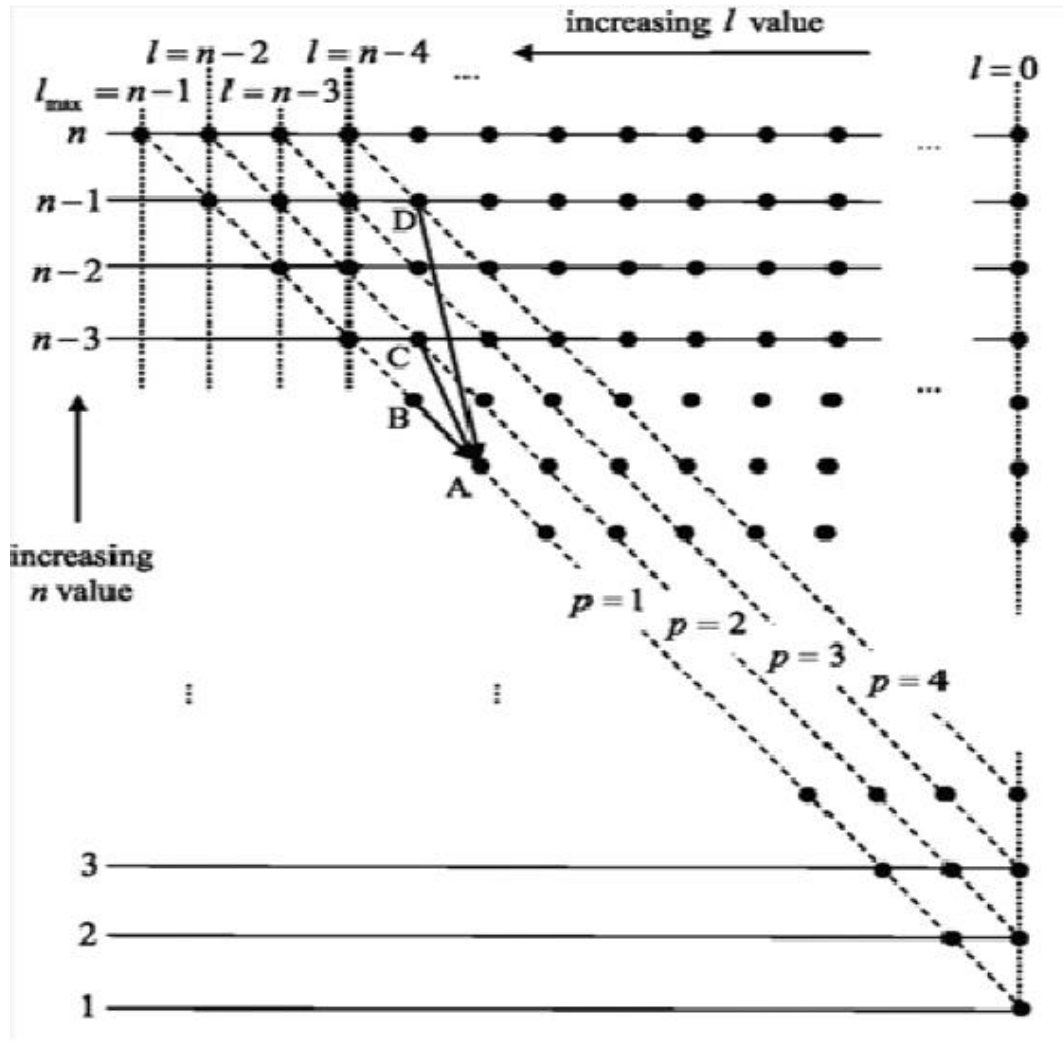


Fig. 2.1. Schematic representing the high n -, l -, m -valued stationary states, drawn to emphasize the parameter $p \equiv n - l$. Each solid circle on the diagram represents $2l + 1$ z -projection substates [14].

Figure 2.1 is a schematic representation of stationary quantum states. Vertical lines and horizontal lines represent states of constant l and n respectively. Each dot on the diagram represents the $2l + 1$ z -projection substates, m . Each diagonal runs along a certain value of p , where $p \equiv n - l$. The quantity p is introduced since the states of interest have low p values relative to n and the formulae for the gravitational eigenfunctions are more conveniently expressed in terms of p . Exact formulae for state to state transition rates have been

developed for transitions along the same p diagonal such as B to A in figure 2.1. Likewise, exact formulae exist for the transitions from one diagonal to the next, such as transition C to A in figure 2.1. However, when considering a transition like D to A in figure 2.1, the situation becomes progressively more complicated as we move to the right of the state diagram and approximate formulas must be employed [14, 15].

Recent research has focused on finding empirical relationships to predict state to state transition rates and lifetimes of gravitational eigenstates beyond the far right of the state diagram in figure 2.1. Whinray and Ernest [17] were able to show low p values were associated with lower state to state transition rates and that state lifetimes were proportional to $n^3 l^\beta$ where $\beta = 2.009 \pm 0.004$. However, Whinray and Ernest [17] limited their study to gravitational eigenstates with initial and final m values of 0. Bonham et al [21] extended the work by Whinray and Ernest [17] to include all possible m decay channels (i.e. $\Delta m = -1, 0, 1$). Significantly, Bonham et al [21] found that the state to state transitions rates were greatest for the $\Delta m = 0$ decay channel when the initial value of m (m_i) was set to zero. Hence, the $\Delta m = 0$ decay channel can act as a maximal constraint on state to state transition rates for states with $m_i = 0$. It was also found that the sum of all the state to state transition rates for all Δm decay channels was constant regardless of the value of m_i . However, neither Whinray and Ernest [17], nor Bonham et al [21], found an empirical relationship that could be extrapolated to calculate state to state transition rates at high values of n and l .

The work by Whinray and Ernest [17] and Bonham et al [21] used the same central mass for all levels of n and p studied. This means that as n increased and the average radial distance of gravitational eigenstates increased, the binding energy decreased. Whilst these previous

studies provide information on the behaviour of gravitational eigenstates for increasing n around the same central mass, they do not provide data on how state to state transition rates are expected to behave in gravitational systems with different central masses. Hence, in this paper, state to state transition rates will be studied as a function of central mass. The binding energy will be held constant which will require the average radial distance of gravitational eigenstates, and thus n , to increase. The results from this paper will add to the knowledge of the empirical behaviour of the state to state transition rates of gravitational eigenstates in increasingly deep gravitational wells.

(Examiners: As advised in Paper 1, please read appendix B for an extended literature review relevant to both paper 1 and paper 2.)

2.3) Methods:

2.3.1) Mathematical theory –Schrödinger Equation for weak gravity:

The mathematical framework for the Schrödinger Equation for weak gravity has been previously developed by Ernest [14, 15]. Salient features relevant to this study are outlined below.

The formulation of the Schrödinger equation for weak gravity is accomplished by replacing the Coulomb potential in the atomic case with the Newtonian gravitational potential to give

$$-\frac{\hbar^2}{2\mu}\nabla^2\psi(r, \theta, \phi) - \frac{GMm_p}{r}\psi(r, \theta, \phi) = i\hbar\frac{\partial}{\partial t}\psi(r, \theta, \phi) \quad (2.1)$$

where μ is the reduced mass, M is the central mass and all other symbols have their usual meanings.

The time independent Schrodinger equation for weak gravity is found using separation of variables to give

$$-\frac{\hbar^2}{2\mu}\nabla^2\psi(r, \theta, \phi) - \frac{GMm_p}{r}\psi(r, \theta, \phi) = E_n\psi(r, \theta, \phi) \quad (2.2)$$

where the energy levels E_n are

$$E_n = -\frac{\mu G^2 m_p^2 M^2}{2\hbar^2} \left(\frac{1}{n^2}\right) \quad (2.3).$$

The eigenfunction solutions to (2.2) are

$$|u\rangle = u_{n,\ell,m}(\mathbf{r}, t) = R_{n,\ell}(r)Y_{\ell,m}(\theta, \phi) \quad (2.4)$$

where l , m and n are the standard quantum eigenvalues. The radial component and spherical harmonics in (2.4) are respectively given by

$$R_{n,l}(r) = N_{nl} \left(\frac{2r}{nb_0}\right)^l e^{\left(-\frac{r}{nb_0}\right)} L_{n-l-1}^{2l+1} \left(\frac{2r}{nb_0}\right) \quad (2.5)$$

and

$$Y_{l,m}(\theta, \phi) = \frac{(-1)^m}{2^l l!} \sqrt{\frac{2l+1}{4\pi} \frac{(l-m)!}{(l+m)!}} (\sin\theta)^m e^{im\phi} \sum_{k=0}^l \frac{(-1)^{l-k} l!}{k!(l-k)!} \frac{(2k)! (\cos(\theta))^{2k-l-m}}{(2k-l-m)!} \quad (2.6).$$

Similar to the parameter a_0 in the atomic case, Ernest (2009a, 2009b) introduces b_0 where

$$b_0 = \frac{\hbar^2}{\mu GMm_p} \quad (2.7).$$

In (2.5), the normalisation constant is given by

$$N_{nl} = \left\{ \left(\frac{2}{nb_0} \right)^3 \frac{(n-l-1)!}{2n((n+l)!)^3} \right\}^{\frac{1}{2}} \quad (2.8)$$

and

$$L_{n-l-1}^{2l+1} \left(\frac{2r}{nb_0} \right) = (n+1)! \sum_{k=0}^{n-l-1} \frac{(-1)^{k+2l} \left(\frac{2r}{nb_0} \right)^k}{(n-l-1-k)! (2l+1+k)! k!} \quad (2.9)$$

are the standard form of the Laguerre polynomials.

2.3.2) Mathematical Theory – State to state transition rate:

The state to state transition rate for radiative dipole decay $A_{i,f}$ for a transition $n_i \rightarrow n_f$ from initial state $|i\rangle$ to final state $|f\rangle$ for a charged particle is given by

$$A_{i,f} = \frac{\omega_{if}^3 |\langle f | e\mathbf{r} | i \rangle|^2}{3\varepsilon_0 \pi \hbar c^3} = \frac{\omega_{if}^3 \Pi_{if}^2}{3\varepsilon_0 \pi \hbar c^3} \quad (2.10).$$

Here, e is the electronic charge, ε_0 the electrical permittivity of free space, ω_{if} is the angular frequency given by

$$\omega_{if} = \frac{\mu G^2 m_p^2 M^2}{2\hbar^2} (n_f^{-2} - n_i^{-2}) \quad (2.11)$$

and Π_{if} is the absolute value of the dipole matrix element for spontaneous decay for the transition $|i\rangle$ to $|f\rangle$. All other symbols have their usual meanings. The dipole matrix element Π_{if} in (2.10) involves overlap integrals over the azimuthal, polar and radial coordinates leading to an allowed set of decay channels requiring the selection rules for quantum numbers m and l to obey $\Delta m = -1, 0, +1$ and $\Delta l = -1, +1$.

2.3.3) State to state transition rate as a function of central mass:

The purpose of this investigation was to examine state to state transition rates as a function of central mass for gravitational eigenstates of the same binding energy. State to state transition rates were evaluated for the values of n_i , l_i , m_i , Δl , Δp , Δm and central mass M as outlined below. The M range studied was 8.58×10^9 kg to 3.35×10^{11} kg. In order to maintain a constant binding energy across all gravitational eigenstates, n_i was increased as M increased according to (2.3). Related n_i range was 50, 100, 150, ..., 1950, though the lowest value of n_i (and hence central mass) increased as needed for increased values of p_i .

State to state transition rates were evaluated for the range of M and n_i above with a binding energy of -172 eV for $p_i = 3, 10, 25, 50, 75, 100$ and $\Delta p = -5, -4, -3, -2, -1, 0$. When $p_i = 3$, only the $\Delta p = -2, -1, 0$ decay channels were examined due to selection rules. Where $\Delta p = -5, -4, -3, -2$, transition rates were calculated for both the $\Delta l = -1$ and $\Delta l = 1$ decay channels. Again, due to selection rules, the transitions rates for $\Delta p = -1, 0$ were only evaluated for $\Delta l = -1$. For all p_i , state to state transition rates were evaluated for $m_i = 0$ and $\Delta m = 0$. However, for $p_i = 3$, the state to state transition rates for $\Delta m = -1$ and $\Delta m = 1$ were also evaluated at $m_i = 0$ for $n_i = 50, 100, 150, \dots, 1000$ (M range of 8.58×10^9 kg to 1.72×10^{11} kg) and $\Delta p = -2, -1, 0$. From Bonham et al [21] it was expected that the state to state transition rate through the $\Delta m = 0$ decay channel would act as a maximum constraint on the state to state transition rate for all Δm decay channels when $m_i = 0$ and this acted as a check of those findings for the values evaluated here.

To check consistency of trends for other binding energies, state to state transition rates were also calculated for the binding energy of -344 eV at $p_i = 3, 10, 50, 100$ for $\Delta p = -2, -1, 0$ for

the same range of M and n_i evaluated for -172 eV above. Where $\Delta p = -2$, transition rates were calculated for both the $\Delta l = -1$ and $\Delta l = 1$ decay channels. Due to selection rules, the transitions rate for $\Delta p = -1, 0$ were only evaluated for $\Delta l = -1$. For all p_i , state to state transition rates were evaluated for $m_i = 0$ and $\Delta m = 0$ as this acts to constrain maximal state to state transition rate for all Δm decay channels [21].

(Examiners: Please see appendix I for the relevant computer package and appendix J for the relevant computer package which was used to perform all calculations in this paper).

2.3.4) Avoiding relativistic regions of gravity around the central mass M :

The Schrodinger Equation for weak gravity is only accurate in non-relativistic regions of deep gravitational wells. Relativistic regions around the central mass are avoided by ensuring $r_n \gg r_s$ where r_n is the average radial position of a gravitational eigenstate given by

$$r_n = n^2 b_0 \quad (2.12)$$

and r_s is the Schwarzschild radius, given by

$$r_s = \frac{2GM_0}{c^2} \quad (2.13).$$

In this paper, avoidance of relativistic regions was ensured by the requirement $r_n \geq 1000r_s$.

(Examiners: Please see appendix D for extended methods relevant to paper 2).

2.4) Results:

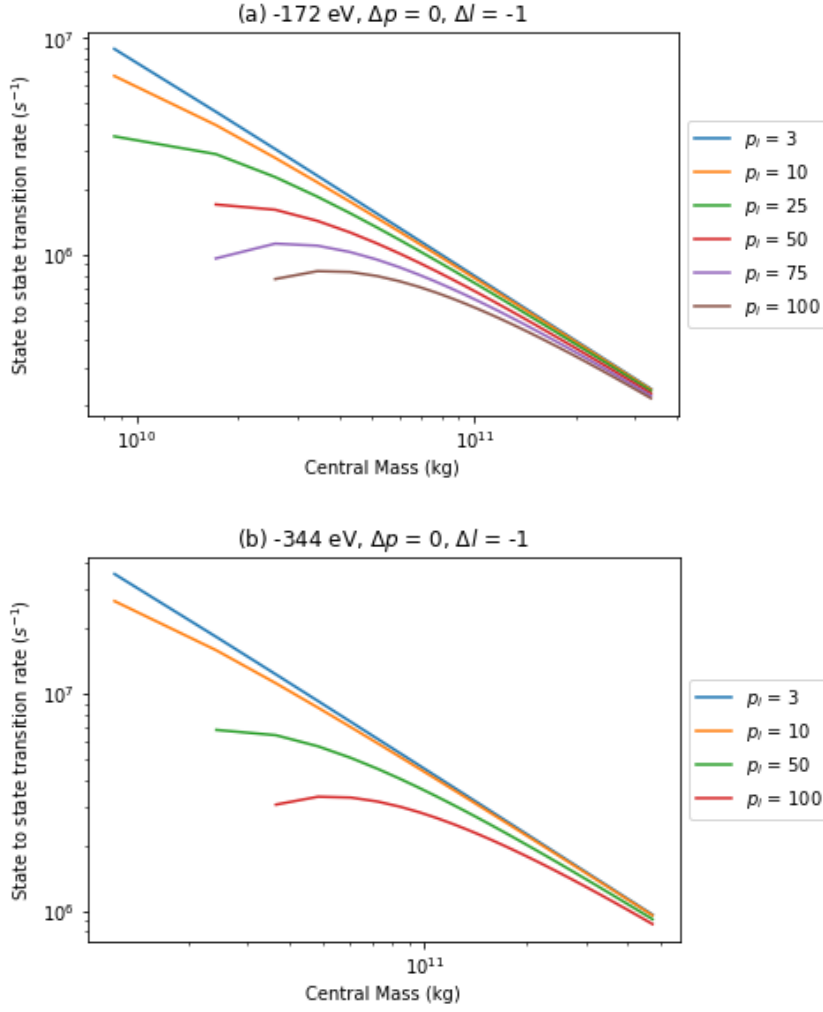


Fig. 2.2. Log-log plot of state to state transition rate $A_{i,f}$ as a function of central mass with $\Delta p = 0$, $\Delta l = -1$ and $\Delta m = 0$. (a) State binding energy is -172 eV for $p_i = 3, 10, 25, 50, 75$ and 100. (b) State binding energy is -344 eV for $p_i = 3, 10, 50$ and 100.

Figure 2.2(a) is a log-log plot of state to state transition rate as a function of central mass for a state binding energy of -172 eV. Here $\Delta p = 0$, $\Delta l = -1$ and $\Delta m = 0$. Each line in figure 2.2 represents a different p_i . In all graphs in this section, the starting point of each line for each p_i reflects the lowest n_i evaluated due selection rules. Consistent with previous research [17,

21], when $\Delta p = 0$, the lowest p_i is associated with the highest decay rate and as p_i increases the transition rate decreases. For $p_i = 3, 10, 25$ and 50 the gradient becomes gradually more negative as the central mass increases. For $p_i = 75$ and 100 , the gradient is initially positive and becomes negative as the central mass increases. In all cases, the relationship between state to state transition rate and central mass approaches a negative linear log-log relationship. Figure 2.2(b) shows that the trends established in figure 2.2(a) are maintained when the binding energy is doubled, however, the magnitude of the state to state transition rate is increased.

To maintain a constant binding energy in all graphs in the results presented here, n_i must increase as the central mass increases. Also, l_i must grow with n_i to maintain a constant p_i which leads to the ratio of l_i to n_i rising. These points are important since all p_i lines approach a negative linear log-log relationship for all graphs in this paper as the central mass increases, regardless of the values of p_i , Δp and Δl investigated.

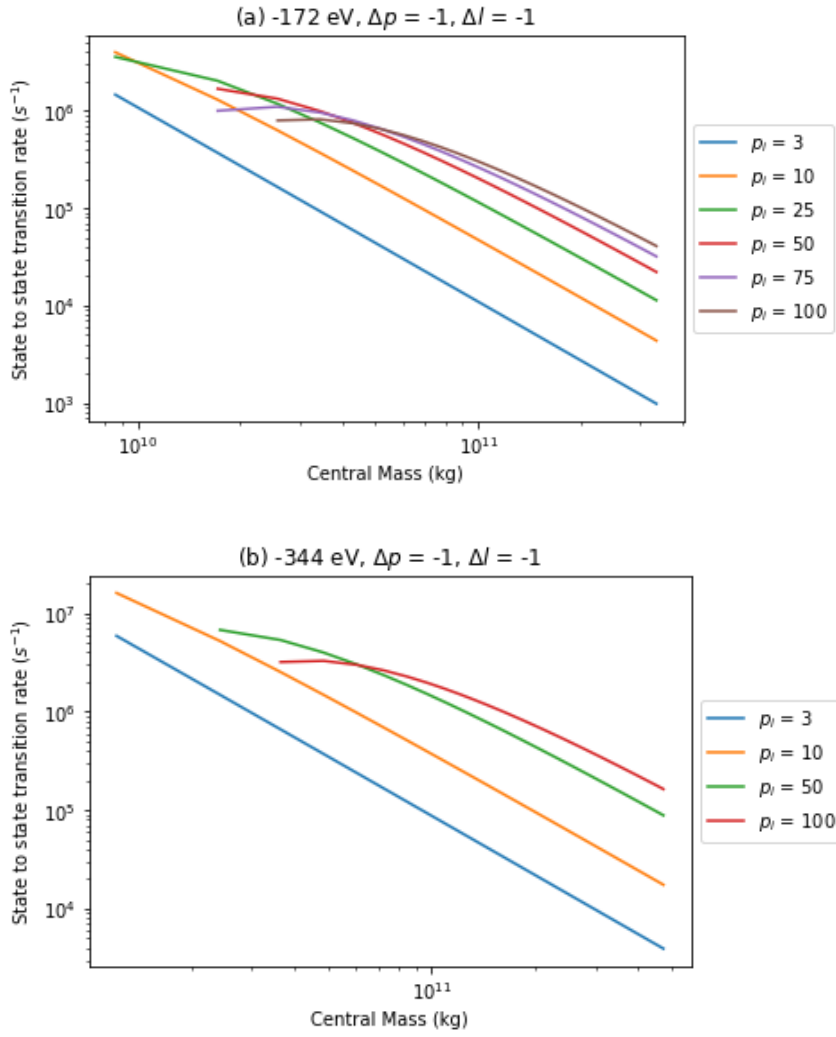


Fig. 2.3. Log-log plot of state to state transition rate $A_{i,f}$ as a function of central mass with $\Delta p = -1$, $\Delta l = -1$ and $\Delta m = 0$. (a) State binding energy is -172 eV for $p_i = 3, 10, 25, 50, 75$ and 100. (b) State binding energy is -344 eV for $p_i = 3, 10, 50$, and 100.

Figure 2.3 shows the state to state transition rate plotted as a function of central mass for $\Delta p = -1$ and state binding energy (a) -172 eV and (b) -344 eV. Both 2.3(a) and 2.3(b) look similar for each p_i investigated with the only obvious difference being the increased transition rate associated with a higher binding energy in 2.3(b). The trends in both figure 2.3(a) and 2.3(b) are consistent with lower p_i being associated with lower transition rates. When central mass and n_i are low, the state to state transition rates are often found to be higher for lower p_i ,

though this effect is lost as the central mass increases and the approximate negative linear log-log relationship is established.

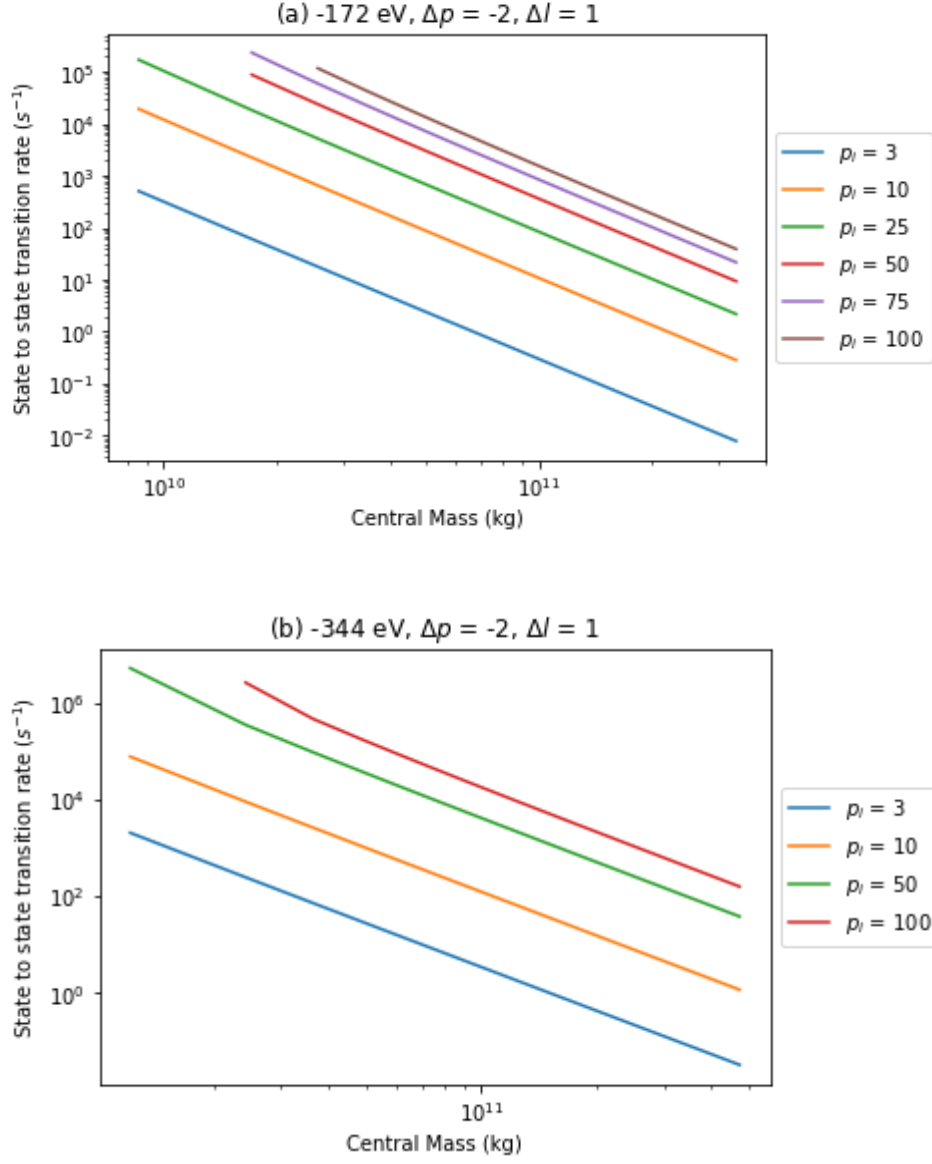


Fig. 2.4. Log-log plot of state to state transition rate $A_{i,f}$ as a function of central mass for $\Delta p = -2$, $\Delta l = 1$ and $\Delta m = 0$. (a) State binding energy is -172 eV for $p_i = 3, 10, 25, 50, 75$ and 100. (b) State binding energy is -344 eV for $p_i = 3, 10, 50$, and 100.

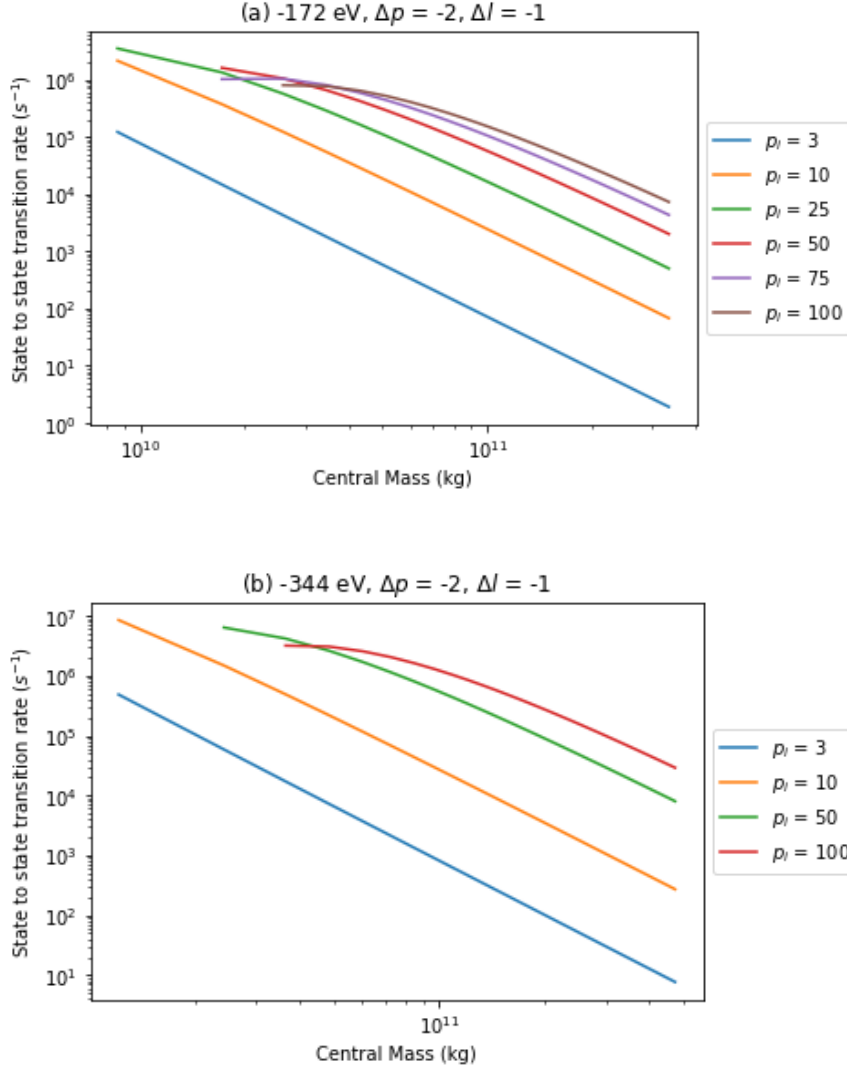


Fig. 2.5. Log-log plot of state to state transition rate $A_{i,f}$ as a function of central mass for $\Delta p = -2$, $\Delta l = -1$ and $\Delta m = 0$. (a) State binding energy is -172 eV for $p_i = 3, 10, 25, 50, 75$ and 100. (b) State binding energy is -344 eV for $p_i = 3, 10, 50$, and 100.

Figures 2.4 and 2.5 show the state to state transition rate as a function of central mass for $\Delta p = -2$. All lines consistently approach a negative linear log-log relationship for both binding energies of -172 eV and -344 eV in figures 2.4 and 2.5. Figure 2.5 is consistent with the results found in figure 2.3 which suggests the shape of trends for low central masses is more dependent on Δl than on Δp , though $\Delta p = -2$ is associated with a lower decay rate when

compared with $\Delta p = -1$. Figure 2.4 shows that when central mass is lower and $\Delta l = 1$, the initial gradient is more negative, and this is more obvious for higher p_i .

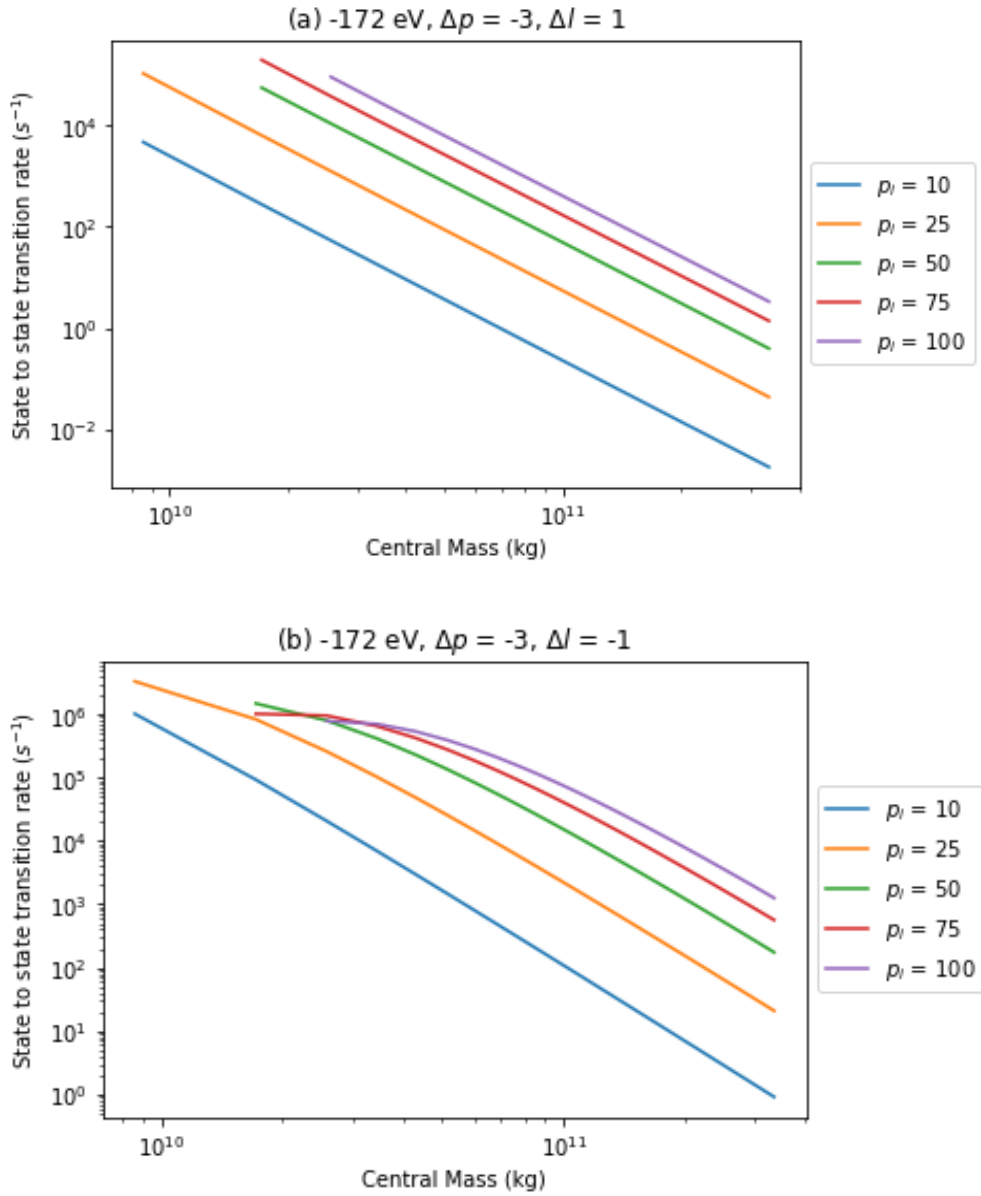


Fig. 2.6. Log-log plot of state to state transition rate $A_{i,f}$ as a function of central mass for $p_i = 10, 25, 50, 75$ and 100 . Here the binding energy is -172 eV with $\Delta p = -3$ and $\Delta m = 0$. (a) $\Delta l = 1$. (b) $\Delta l = -1$.

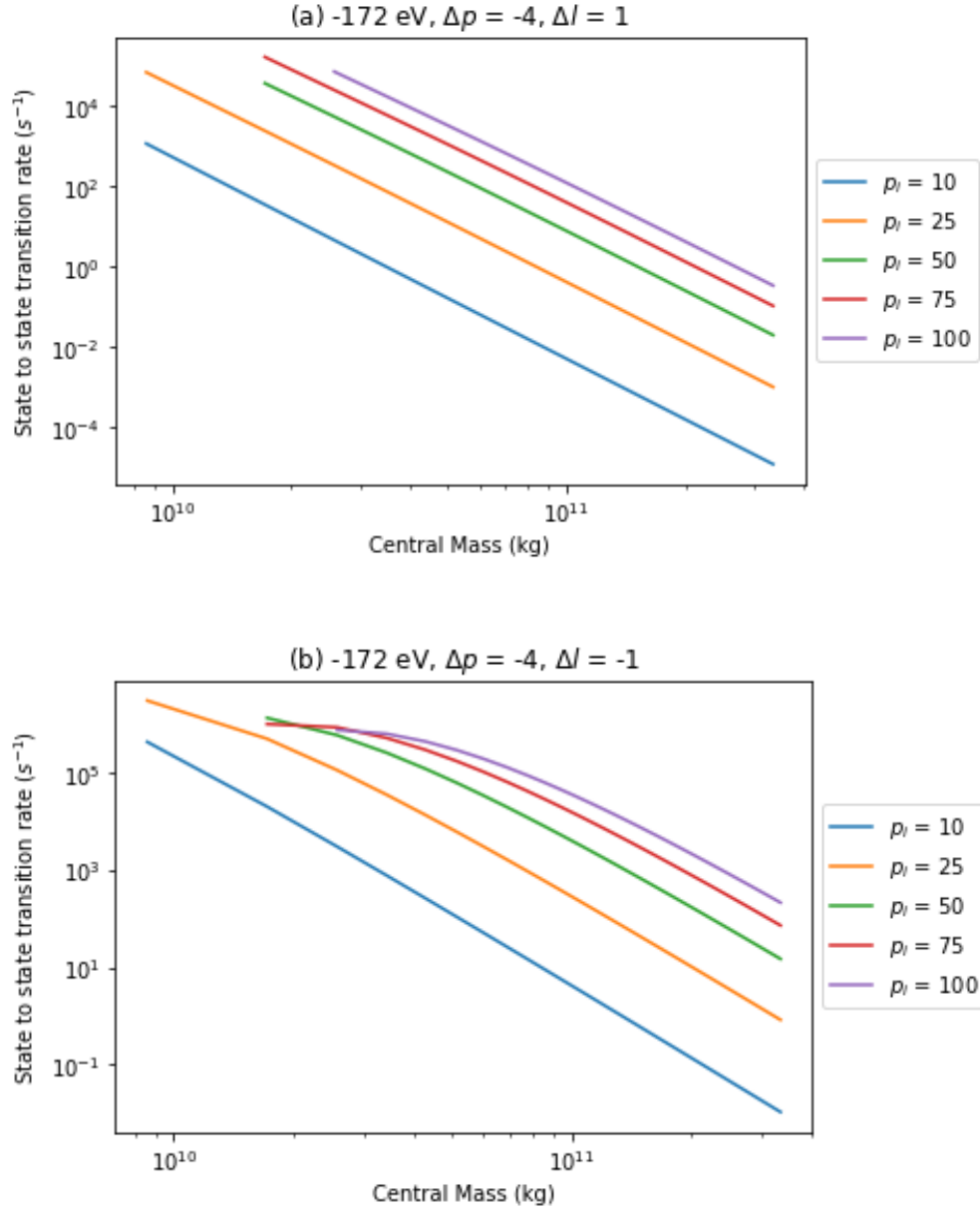


Fig. 2.7. Log-log plot of state to state transition rate $A_{i,f}$ as a function of central mass for $p_i = 10, 25, 50, 75$ and 100 . Here the binding energy is -172 eV with $\Delta p = -4$ and $\Delta m = 0$. (a) $\Delta l = 1$. (b) $\Delta l = -1$.

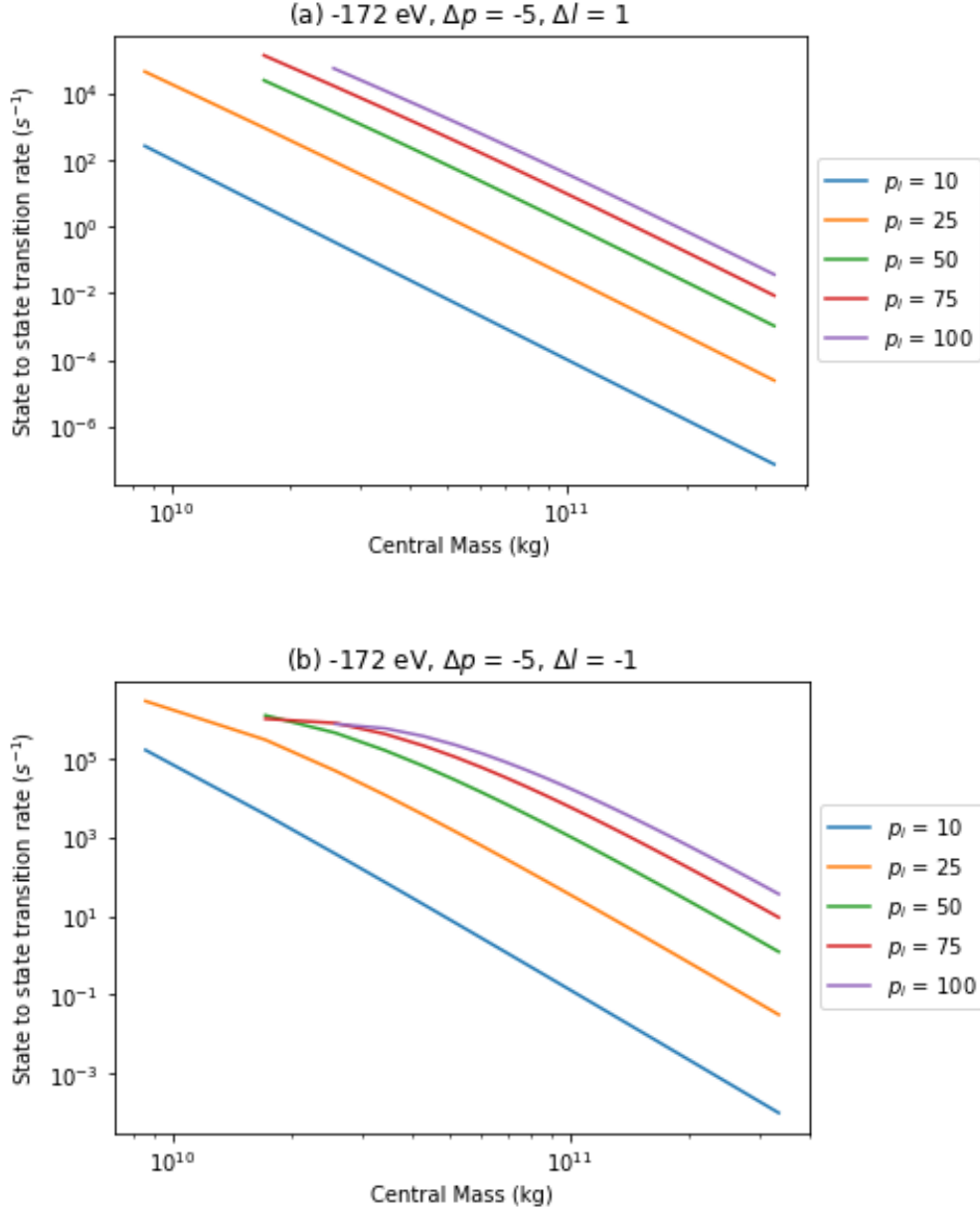


Fig. 2.8. Log-log plot of state to state transition rate $A_{i,f}$ as a function of central mass for $p_i = 10, 25, 50, 75$ and 100 . Here the binding energy is -172 eV with $\Delta p = -5$ and $\Delta m = 0$. (a) $\Delta l = 1$. (b) $\Delta l = -1$.

Figures 2.6, 2.7 and 2.8 show consistency of results found in figures 2.3, 2.4 and 2.5. The trends of the curves are more dependent on Δl than Δp for low p_i . When $\Delta l = -1$, $\Delta p \leq -1$ and the central mass is low, the state to state transition rate for higher p_i is often lower than the

transition rate for low p_i and the gradient of the curves is frequently positive. However, as the central mass increases, the gradient for each p_i line becomes negative and a linear log-log relationship for state to state transition rate and central mass is approached. However, when $\Delta l = 1$, $\Delta p \leq -1$ and the central mass is low, the state to state transition rate is always higher for larger p_i values. Also, the gradient of each line of p_i is negative for the entire central mass range. Consistent with previous research [17, 21] the state to state transition rate for the $\Delta l = -1$ decay channels is higher than that for the $\Delta l = 1$ decay channel for a given Δp .

Furthermore, more negative Δp values are associated with lower decay rates. Significantly, all trends were maintained when the binding energy of -172 eV was compared with -344 eV, though the higher binding energy is associated with a higher decay rate.

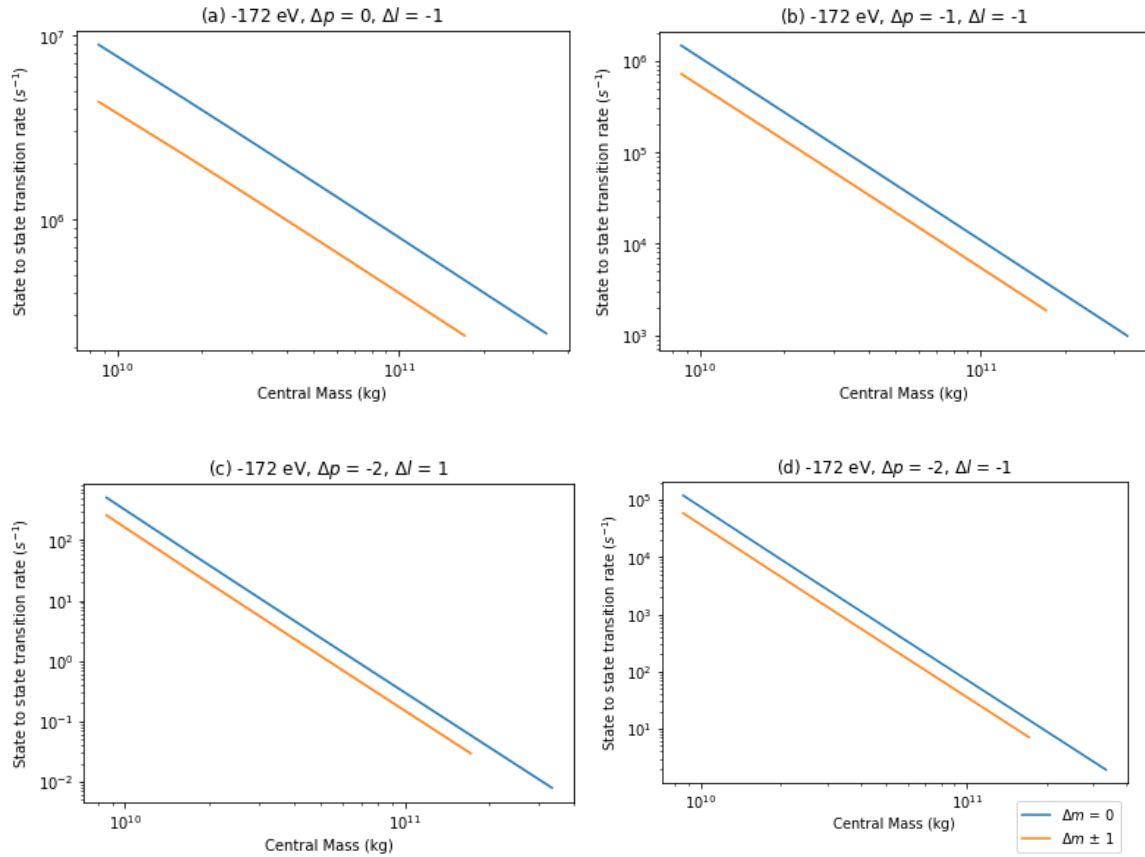


Fig. 2.9. Log-log plot of state to state transition rate $A_{i,f}$ as a function of central mass for binding energy of -172 eV, $p_i = 3$, $m_i = 0$ and $\Delta m = -1, 0, 1$. (a) $\Delta p = 0$, $\Delta l = -1$. (b) $\Delta p = -1$, $\Delta l = -1$. (c) $\Delta p = -2$, $\Delta l = 1$. (d) $\Delta p = -2$, $\Delta l = -1$

Bonham et al [21] showed the state to state transition rate for the $\Delta m = 0$ decay can constrain the upper bound on the state to state transition rate for other Δm decay channels provided $m_i = 0$. Figure 2.9 acts as a check of this finding for the values evaluated in this study. In figure 2.9, state to state transition rate is plotted as a function of central mass for $p_i = 3$ and $m_i = 0$, for (a) $\Delta p = 0$ with $\Delta l = 1$, (b) $\Delta p = -1$ with $\Delta l = 1$, (c) $\Delta p = -2$ with $\Delta l = 1$ and (d) for $\Delta p = -2$ with $\Delta l = 1$. In all cases, the state to state transition rate for the $\Delta m = 0$ decay channel was higher when compared with the $\Delta m = \pm 1$ decay channels.

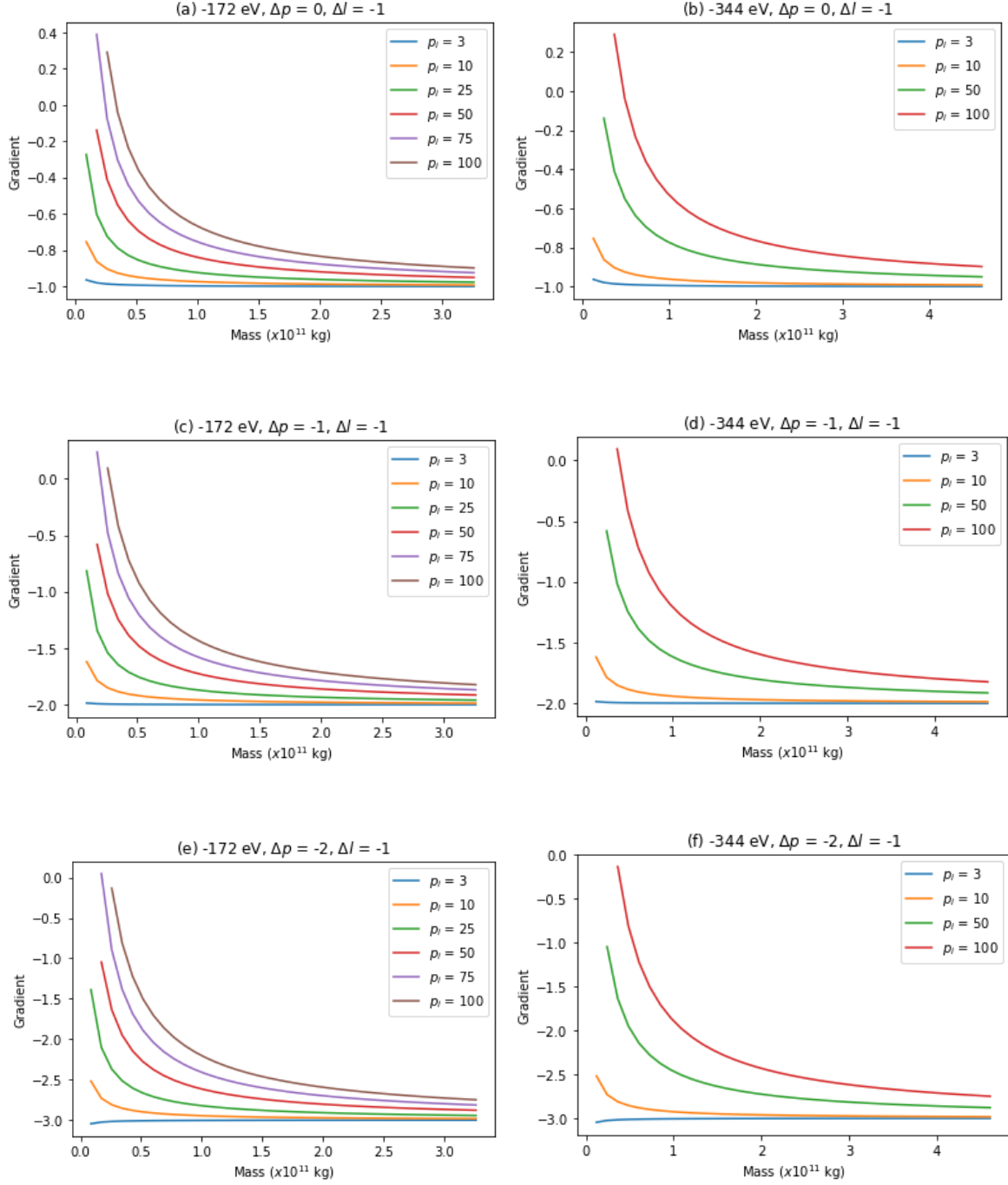


Fig. 2.10. Gradient of the log-log relationship between state to state transition rate and central mass, plotted as a function of central mass with $\Delta l = -1$. (a) Binding energy of -172 eV, $\Delta p = 0$. (b) Binding energy of -344 eV, $\Delta p = 0$. (c) Binding energy of -172 eV, $\Delta p = -1$. (d) Binding energy of -344 eV, $\Delta p = -1$. (e) Binding energy of -172 eV, $\Delta p = -2$. (f) Binding energy of -172 eV, $\Delta p = -2$.

Figure 2.10 plots the gradient of the log-log relationship between state to state transition rate and central mass for $\Delta p = 0, -1, -2$ and $\Delta l = -1$ i.e. the gradients of the curves in figures 2.2, 2.3 and 2.5. In figures 2.10(a) to 2.10(f), the trends for the case where the binding energy is -172 eV is the same as the case where the binding energy is -344 eV. Figures 2.10(a) to 2.10(f) show that as p_i decreases the magnitude of the negative gradient increases. As the central mass increases, all gradients σ in all figures are found to approach the following approximate relationship:

$$\sigma = \Delta p - 1 \quad (2.14)$$

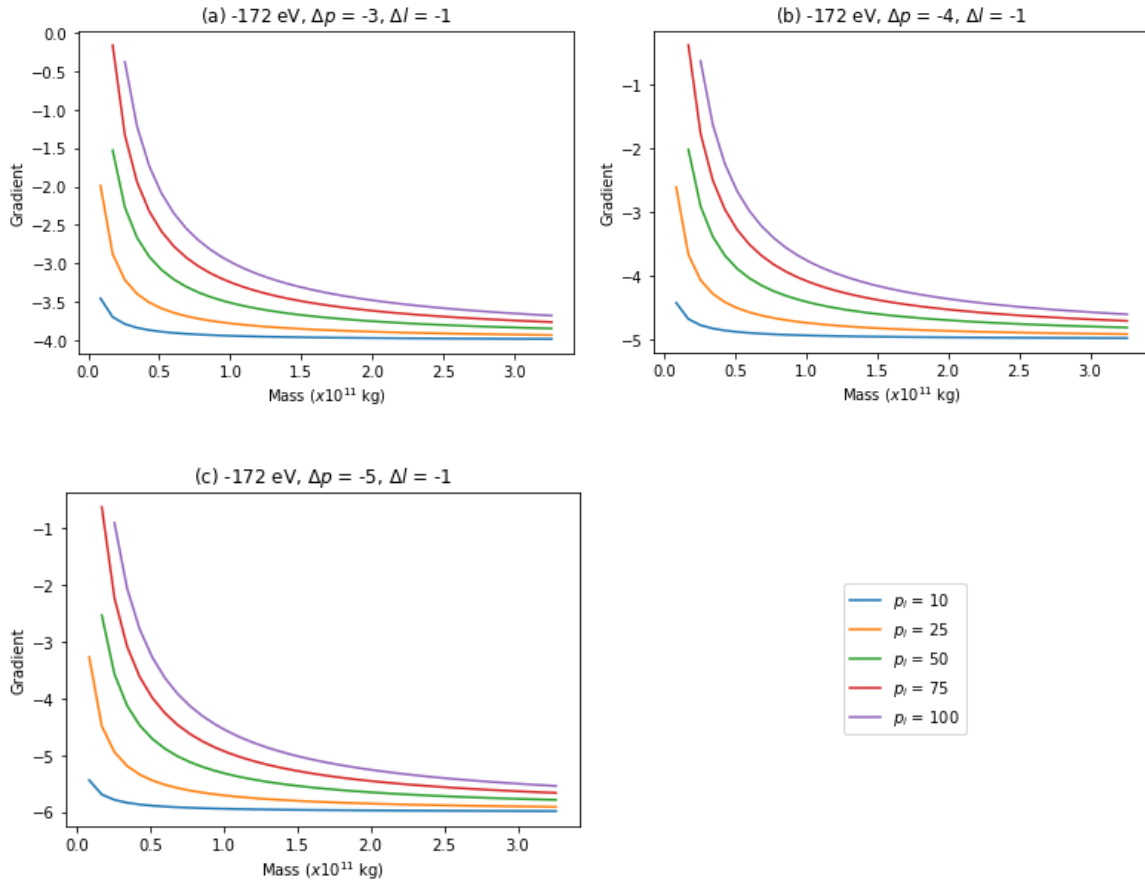


Fig. 2.11. Gradient of the log-log relationship between state to state transition rate and central mass, plotted as a function of central mass for a binding energy of -172 eV with $\Delta l = -1$. (a) $\Delta p = -3$. (b) $\Delta p = -4$ (c) $\Delta p = -5$.

Figures 2.11(a), 2.10(b) and 2.11(c) extends the results found in figure 2.9 to $\Delta p = -3, -4, -5$, and correlate with the gradients of the curves in figures 2.6(b), 2.7(b) and 2.8(b) respectively. Again, it has been found that as the central mass increases, all gradients approach the relationship presented in (2.14).

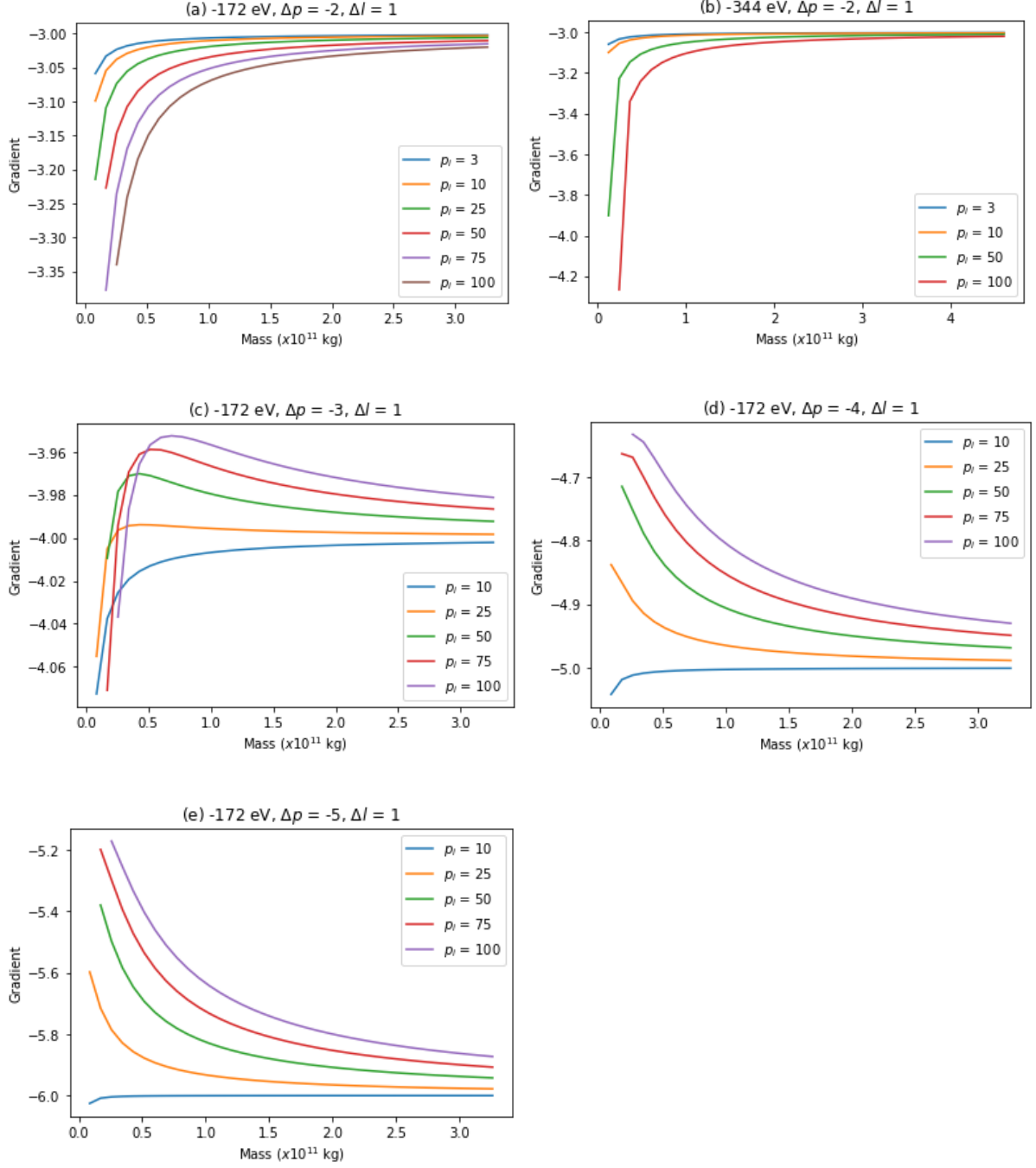


Fig. 2.12. Gradient of the log-log relationship between state to state transition rate and central mass, plotted as a function of central mass with $\Delta l = 1$. (a) Binding energy of -172 eV, $\Delta p = -2$. (b) Binding energy of -344 eV, $\Delta p = -2$. (c) Binding energy of -172 eV, $\Delta p = -3$. (d) Binding energy of -172 eV, $\Delta p = -4$. (e) Binding energy of -172 eV, $\Delta p = -5$.

Figures 2.12(a), 2.12(b), 2.12(c), 2.12(d) and 2.12(e) reflect the gradients of the curves in figures 2.4(a), 2.4(b), 2.6(a), 2.7(a) and 2.8(a) respectively. Comparing figure 2.12 to figures 2.10 and 2.11 above, the most significant difference is the Δl value which is +1 in figure 2.12 as this reflects the difference in the pattern of gradients for each p_i . In figures 2.12(a) and 2.12(b), the trends across the two binding energies of -172 eV and -344 eV are equivalent. In figures 2.12(a), 2.12(b) and 2.12(c), the magnitude of the negative gradient is larger for lower central masses before the gradients for all p_i approach the relationship in (2.14) as the central mass increases. Again, the approximate relationship in (2.14) is approached as the central mass increases.

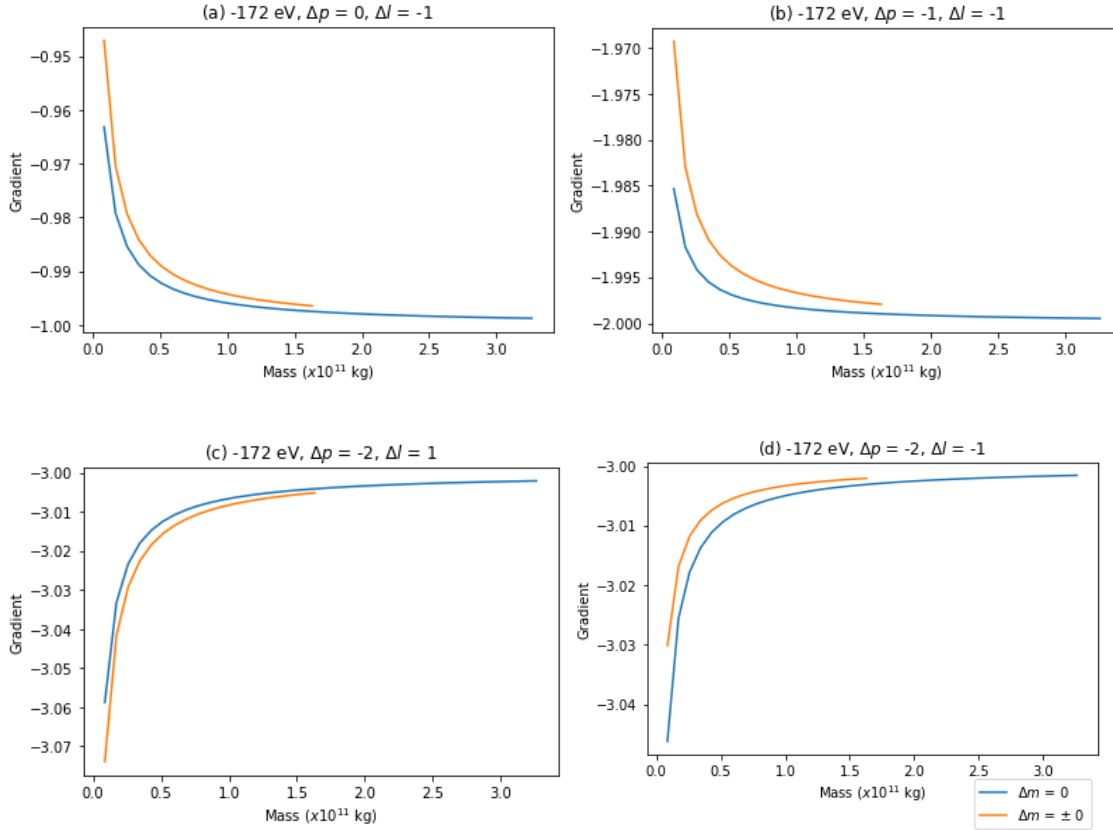


Fig. 2.13. Gradient of the log-log relationship between state to state transition rate and central mass, plotted as a function of central mass for binding energy -172 eV, $\Delta m = 0$ or ± 1 and $p_i = 3$. (a) $\Delta p = -0$, $\Delta l = -1$. (b) $\Delta p = -1$, $\Delta l = -1$ (c) $\Delta p = -2$, $\Delta l = 1$. (d) $\Delta p = -2$, $\Delta l = -1$.

Figure 2.13 plots the respective gradients of the curves in figure 8 as a function of central mass. Figure 2.13 checks the trends in gradients for different values of Δm . The difference in gradients for different Δm across the range of central mass values evaluated here is less than 1% for all Δp and Δl . Also, as the central mass increases, the difference between the gradients decreases. Figures 2.12(a), 2.12(b) and 2.12(c) show that the magnitude of the negative gradient when $\Delta m = \pm 1$ is less than when $\Delta m = 0$ and $\Delta l = -1$ for $\Delta p = 0, -1, -2$. Contrarily, figure 2.12(c) shows the magnitude of the negative gradient when $\Delta m = \pm 1$ is more than when $\Delta m = 0$ and $\Delta l = 1$ for $\Delta p = -2$. The findings here show that as the central mass increases, the approximate relationship in (2.14) is approached regardless of the Δm decay channel evaluated.

2.5) Discussion:

This study applied the mathematical framework provided by the Schrödinger equation for weak gravity to investigate how the magnitude of the central mass affects state to state transition rates of gravitational eigenstates held in deep gravitational wells in non-relativistic regions of gravity. To prevent particles in gravitational eigenstates being ‘ionized’ from a central mass, a binding energy greater or equal to the expected energy of photons within a gravitational system is required. Hence a binding energy of -172 eV was chosen as this reflects the approximate temperature of a galactic halo [22]. This ensures trends evaluated here can be extrapolated to galactic scales to contribute to analysis of the QDM theory. To test for consistency of trends established at -172 eV, a second binding energy of -344 eV was also evaluated.

The linear relationship between central mass and the principle quantum number n is reflected in (2.3). Thus, the trends discussed here also directly reflect changing n with the same binding energy. Previous empirical studies into the state to state transition rates of gravitational eigenstates looked at the effect of increasing n whilst maintaining the same central mass. However, since the central mass was held constant, the binding energy decreased as n increased. Consistent with these previous studies, this investigation found that state to state decay rate decreased with increasing n and decreasing p_i when $\Delta p < 0$ [17, 21]. When $\Delta p = 0$, it was found that the state to state transition rate was higher for lower p_i which is also consistent with Bonham et al [21].

Figures 2.2-2.9 suggest a linear log-log relationship between state to state transition rate and central mass for all evaluated Δp and Δl values regardless of the binding energy used. This trend is most obvious when $\Delta l = 1$. However, this trend is not obvious for higher values of p_i , particularly for low central mass values and for cases when $\Delta l = -1$. This reflects the relative value of p_i to n_i . As the central mass increases, the relative value of p_i to n_i decreases. When p_i is less than 20% of n_i , the linear log-log relationship is consistently approached. When considering extrapolation to the galactic scale, the relative value of p_i to n_i can remain low enough for the linear log-log relationship to be a good approximation of spontaneous dipole decay despite much higher values of p_i .

As p_i decreases (so l_i increases relative to n_i), the radial extent of the probability density decreases [14]. As p_i increases, the radial extent of the probability density increases and there is also an increase in the number of closely spaced spatial oscillations [14]. So the transition rate for higher p_i relative to n_i has more reliance on the spherical harmonics in determining

Π_{ij} in (2.10). This suggests why for low n_i we initially observe some higher p_i with lower state to state transition rates until l_i becomes a significant portion of n_i .

Regardless of binding energy, Δp , p_i , Δm or Δl values evaluated here, the linear log-log relationship between state to state transition rate and central mass has a gradient which approaches the (very approximate) formula (2.14). Higher p_i take longer to approach the relationship in (2.14) which is expected given the shape of the transition rates for each p_i in figures 2.2-2.9. The difference in how quickly different valued p_i eigenstates approach the linear log-log relationship for state to state transition rate and central mass is reflected in how quickly each different valued p_i eigenstate approaches the gradient expressed in (2.14).

The relationship in (2.14) is potentially useful for estimating or checking estimates of state to state transition rates for high n which are impractical to evaluate directly. Suppose we have a state to state transition rate A_1 for an initial gravitational eigenstate with mass M_1 and principle quantum number n_1 . Further suppose we have a state to state transition rate A_2 for another initial gravitational eigenstate with a different mass M_2 and subsequently different principle quantum number n_2 . If both A_1 and A_2 have the same Δp , and their respective initial gravitational eigenstates have the same binding energy and p_i , from (2.14) the relation between A_1 and A_2 can be expressed as

$$\frac{\log_{10} A_2 - \log_{10} A_1}{\log_{10} M_2 - \log_{10} M_1} \approx \Delta p - 1 \quad (2.15).$$

Simplifying and solving for A_2 we obtain

$$A_2 \approx A_1 \left(\frac{M_2}{M_1} \right)^{\Delta p - 1} \quad (2.16).$$

From (2.3), $M \propto n$ and hence it is possible to directly substitute n for M to give

$$A_2 \approx A_1 \left(\frac{n_2}{n_1} \right)^{\Delta p - 1} \quad (2.17).$$

Significantly, (2.17) allows the calculation of state to state transition rate for a given gravitational eigenstate provided the state to state transition rate is known for another gravitational eigenstate with the same p_i and binding energy, and hence also allows determination of state to state decay rates with scaling of the central mass.

Previous attempts have been made to find a predictive empirical relationship between state to state transition rate, Δp and n with little success [17]. Whilst (2.17) provides a simple possible solution, it still has significant limitations. Firstly, we only know that the approximate relationship works for the values evaluated here. Secondly, based on the discussion above, the relationship does not consistently exist until p_i is less than 20% of n_l . This limits the maximum level of n_l and p_i which can be directly evaluated when finding a value for A_1 in (2.17). For example, an accurate estimate of any state to state transition rate for a gravitational eigenstate with $p_i = 1000$ would require the initial direct evaluation of a state to state transition rate for $n_l \geq 5000$ to find A_1 , which exceeds reasonable computation time. The final major issue affecting accuracy is the logarithmic nature of the relationship which requires the factor $\Delta p - 1$ in (2.17) to be closely reflective of the gradient or the error will be extremely high.

Future research may be able to overcome the shortcomings of using (2.17) to estimate state to state transition rates. Firstly, for a given central mass and binding energy, there may exist a relationship between the difference in state to state transition rate and the difference between successive p_i . If such a relationship were found, it would be possible to initially evaluate a state to state transition rate for any convenient p_i (i.e. very low) and then find A_1 in (2.17) for

any p_i of the same central mass and initial principle quantum number. Secondly, further investigation into how the gradient of the log-log relationship between state to state transition rate and central mass approaches that expected by (2.14) for a given p_i would lead to greater accuracy.

Despite the limitations of the approximate relation in (2.17), it provides insight into the QDM theory. As the central mass and subsequently n grows, the decrease in state to state transition rate for a given p_i is heavily dependent on Δp . Optical transitions require $\Delta p \sim 10^{21}$. Thus, those transitions which are detectable are the very transitions which quickly become less likely as we consider systems with increasingly larger central masses. Thus, eigenstates at a given binding energy are expected to be ‘darker’ for larger central masses.

2.5.1) Conclusion:

The relationship between two state to state transition rates A_1 and A_2 , with the same Δp , for two initial gravitational eigenstates with respective central masses M_1 and M_2 , can be approximately expressed as $A_2 \approx A_1 \left(\frac{M_2}{M_1}\right)^{\Delta p - 1}$, provided both initial gravitational eigenstates have the same p_i and binding energy. This relationship can also be expressed as a function of n as $A_2 \approx A_1 \left(\frac{n_2}{n_1}\right)^{\Delta p - 1}$. Therefore, provided either A_1 or A_2 is known, the state to state transition rate can be estimated for a gravitational eigenstate with a respective n_1 or n_2 . This paper supports previous research showing there exists a set of high n and low p valued theoretical gravitational eigenstates which have properties congruent with that expected for dark matter. Furthermore, this paper clearly demonstrates the rapid decrease in the state to state transition rates of gravitational eigenstates as the central mass increases.

2.6) References

- [1] F. Zwicky, “Spectral displacement of extra galactic nebulae,” *Helv. Phys. Acta* **6**, 110 (1933).
- [2] J. G. de Swart, G. Bertone and J. van Dongen, “How dark matter came to matter,” *Nat. Astron.* **1**, 0059 (2017).
- [3] S. M. Faber and J. S. Gallagher, “Masses and mass-to-light ratios of galaxies,” *Ann. Rev. Astron. Astrophys.* **17**, 135 (1979).
- [4] D. Harvey, R. J. Massey, T. D. Kitching, A. M. Taylor and E. R. Tittley, “The non-gravitational interactions of dark matter in colliding galaxy clusters,” *Science* **347** 1261381 (2015).
- [5] A. S. Bolton, S. Burles, L. V. E Koopmans, T. Treu, R. Gavazzi, L. A. Moustakas, R. Wayth and D. J. Schlegel, “The Sloan Lens ACS survey. V. The full ACS strong-lens sample,” *Astrophys. J.* **682**, 964 (2008).
- [6] R. Massey, J. Rhodes, R. Ellis, N. Scoville, A. Leauthaud, A. Finoguenov, P. Capak, D. Bacon, H. Aussel, J. Kneib, A. Koekemoer, H. McCracken, B. Mobasher, S. Pires, A. Refregier, S. Sasaki, J. Starck, Y. Taniguchi, A. Taylor and J. Taylor, “Dark matter maps reveal cosmic scaffolding,” *Nature*, **445**, 05497 (2007).
- [7] E. Di Valentino, E. Giusarma, M. Lattanzi, A. Melchiorri and O. Mena, “Axion cold dark matter: status after Planck and BICEP2,” *Phys. Rev. D* **90** 043534 (2014).
- [8] T. M. Undagoitia and L. Rauch, “Dark matter direct-detection experiments,” *J. Phys. G. Nucl. Part. Phys.* **43** 013001 (2015).
- [9] B. Moore, T. Quinn, F. Governato, J. Stadel and G. Lake, “Cold collapse and the core catastrophe,” *Mon. Notices Royal Astron. Soc.* **310**, 1147 (1999).

- [10] B. Moore, S. Ghigna, F. Governato, G. Lake, T. Quinn, J. Stadel and P. Tozzi, “Dark matter substructure within galactic halos,” *Astrophys. J. Lett.* **524**, L19 (1999).
- [11] V. F. Cardone, A. Del Popolo and P. Kroupa, “Angular momentum transfer and the size-mass relation in early type galaxies,” *Mon. Notices Royal Astron. Soc.* **400**, 766 (2009).
- [12] D. I. Clowe, M. Bradac, A. H. Gonzalez, M. Markevitch, S. W. Randall, C. Jones and D. Zaritsky, “A direct empirical proof of the existence of dark matter,” *Astrophys. J. Lett.* **648**, L109 (2006).
- [13] N. E. Mavromatos, M. Sakellariadou and M. F. Yusaf, “Can the relativistic field theory version of modified Newtonian dynamics avoid dark matter on galactic scales?,” *Phys. Rev. D* **79** 081301 (2009).
- [14] A. D. Ernest, “Gravitational eigenstates in weak gravity I: dipole decay rates of charged particles,” *J. Phys. A: Math. Theor.* **42** 115207 (2009).
- [15] A. D. Ernest, “Gravitational eigenstates in weak gravity II: further approximate methods for decay rates,” *J. Phys. A: Math. Theor.* **42** 115208 (2009).
- [16] A. D. Ernest and M. P. Collins, “Structural features of high-n gravitational eigenstates,” *Grav. Cosmol.* **18**, 242 (2012).
- [17] T. A. Whinray and A. D. Ernest, “Relations between transition rates and quantum numbers in gravitational potentials,” *Grav. Cosmol.* **24**, 97 (2018).
- [18] V. V. Nesvizhevsky, H. G. Borner and A. K. Petukhiv, “Quantum states of neutrons in the Earths gravitational field,” *Nature* **415**, 297 (2002).
- [19] H. Zbinden, J. Brendel, W. Tittel and N Gisin, “Experimental test of relativistic quantum state collapse with moving reference frames,” *J. Phys. A Math. Theor.* **34**, 7103 (2001).

[20] M. H. Anderson, J. R. Ensher, M. R. Matthews, C. E. Wieman, and E. A Cornell, “Observation of Bose-Einstein condensation in dilute atomic vapour,” *Science* **269**, 198 (1995).

[21] M. J. Bonham, A. D. Ernest and M. P. Collins, “Relations between the quantum eigenvalue m and transition rates of charged particles held in gravitational eigenstates in non-relativistic regions of deep gravitational wells,” *Paper 1* (2020).

[22] S. Das, S. Mathur and A. Gupta, “The warm-hot, extended, massive circumgalactic medium of NGC 3221: an XMM-Newton discovery,” *Astrophys. J.* **897** ab93d2 (2020).

Appendix A: Guidelines for Authors of Gravitation and Cosmology

Address for submission:

RGS, VNIIMS, Otdel 302, Ozernaya 46, 119361, Moscow, Russia

Phone: +7 (495) 781 28 68, Fax: +7 (495) 781 28 68

e-mail: rusgs@phys.msu.ru; kb20@yandex.ru

Manuscripts should be submitted to the editorial board by e-mail simultaneously to both addresses indicated above. The text should contain the title, authors, their affiliations with exact addresses, e-mail addresses and abstract (at most 20 lines).

All manuscripts are peer reviewed. There is no page charge. PDF files of articles papers will be sent to their authors on request.

An original research article should preferably be no longer than 40 000 characters, a review article should be at most than 70 000 characters. Sections, figures, and tables are numbered with Arabic numerals. References are numbered in the text in the form [1], [2–5], etc. The format for the list of references is indicated in the samples below. References should be listed in the order they appear in the main text.

We ask authors to prepare their files in \LaTeX , `\documentclass{article}` (though Revtex or Revtex4 are also admissible). The use of our old style file GC.STY is optional.

In your TEX file, to include displayed mathematical formulas, please always place the appropriate commands (such as `\[`, `\]`, `$$`, `\begin{equation}`, `\end{equation}`, etc.) on separate lines shift left. Black-and-white figures may be included in your TEX file (if prepared by \LaTeX tools) or may be presented as separate EPS files. Please use archive tools (GZ, ZIP, ARJ) when sending

big files (over 100 kB). If you are sending several files, please send them packed in a single archive file.

Other formats of submission (DOC, PDF, PS) are allowed before peer review. Once a paper is accepted for publication, a \LaTeX version of the manuscript will be requested.

Sample References

[1] F. Zwicky, “Spectral displacement of extra galactic nebulae,” *Helv. Phys. Acta* **6**, 110 (1933).

[2] S. Das and S. N. Patitsas. “Can MOND type hypotheses be tested in a free fall laboratory environment?” *Phys. Rev. D* **87** 107101 (2013).

[2] A. Einstein, *The Meaning of Relativity: Four Lectures Delivered at Princeton University*, (Princeton Univ. Press, Princeton, 2004).

[3] I. I. Ivanov and P. P. Petrov, *The Universe and Its Neighborhood*, Arxiv: 9909.9999; to appear in *Phys. Rev. Z*.

[4] W. W. Wise, in: *Selected Discoveries*, ed. by A.A. Ivanov et al. (North Pole Univ. Press, North Pole, 2016).

[5] H. H. High, *Tops of Gravitational Science*, Ph D Thesis (Everest University, 2999).

Appendix B: Extended Literature review

B.1 – Introduction and background:

This extended literature review is intended to supplement and increase the depth of the background provided in the introductions to the two publishable articles in this dissertation. In many cases, topics raised in the introduction to both papers is extended upon. In other instances, completely new information is provided

Dark matter (DM) refers to any substance which is mostly or exclusively detectable through its gravitating effects. The use of the virial theorem by Zwicky (1937) to estimate the mass of galaxy clusters is one of the earliest observations' indicative of the existence of dark matter. Zwicky (1937) concluded that given the velocity dispersion of nebulae in the Coma system, the average mass density had to be higher than that deduced from visible matter.

In this review, the evidence for DM will be described and an analysis of the most common hypothetical DM candidates will follow. The successes and failures of the standard cosmological model, Lambda Cold Dark Matter (Λ CDM), will be discussed before briefly assessing alternative theories of gravity. Finally, the Quantum Dark Matter (QDM) hypothesis will be reviewed in detail.

B.1.1 – The Λ CDM cosmological model:

Λ CDM is the most cited cosmological interpretation of the universe, largely due to its success in predicting and describing many astrophysical phenomena. However, Λ CDM faces many serious challenges which will be expanded on in section B4. Since many astronomical

observations are interpreted through the filter of Λ CDM, a brief summary of its structure is provided here. Λ CDM consists of three main components:

1. The cosmological constant Λ representing dark energy
2. Cold dark matter (CDM)
3. Baryonic (ordinary) matter

And consists of six parameters:

1. Physical baryon density
2. Physical cold dark matter density
3. Dark energy density
4. Curvature perturbations
5. Scalar spectral index
6. Reionization optical depth

(Hinshaw et al., 2013)

B.2 – Current observational evidence suggesting the existence of DM:

As will be shown, the evidence for DM is robust. Here the rotation curves of galaxies, gravitational lensing, galaxy-cluster collisions, the Cosmic Microwave Background (CMB), Lyman-alpha forest observations and the formation of large-scale structure will be reviewed.

B2.1 – Rotation curves of galaxies:

Rotation curves are graphical representations of orbital velocities of gas and stars plotted as a function of radial distance from the galactic centre. Assuming the validity of current gravitational theories and using only the visible mass in a spiral galaxy, the expected orbital

velocities outside the galactic bulge are expected to decrease. Specifically, using Newtonian dynamics, orbital velocities would be expected to be inversely proportional to the square root of the radial distance from the galactic centre.

Observational studies show an inconsistency between theoretical and observed rotation curves. Rubin et al (1978) sampled ten high luminosity spiral galaxies with classifications Sa through Sc and obtained rotation curves which extended to approximately 80% of the de Vaucouleurs radii. All rotation curves were found to be approximately flat. A more recent study of 30 spiral galaxies in the local universe found 40% of rotation curves had mild declines, 50% were flat and 10% were rising (Yegorova et al., 2011). The contribution of stellar mass to rotation curves has been directly estimated. For example, in galaxy NGC 5005, the maximum stellar disk contribution to the total (flat) rotation curve was approximately 70% (Richards et al., 2015).

B2.2 – Gravitational lensing:

Applying the Theory of General Relativity to the deflection of electromagnetic radiation around an object allows the calculation of the gravitational potential of the same object. Significantly, the deflection of photons does not differentiate between DM and ordinary (baryonic) matter (Bartelmann & Schneider, 2001). Observational evidence from strong, weak and micro lensing is considered below.

B2.2.1 – Strong lensing:

Strong lensing produces multiple images, arcs or Einstein rings. Due to their compact and dense nature, elliptical galaxies can produce strong lensing effects. A study of 63 clear

lensing elliptical galaxies has shown the distribution of mass in elliptical galaxies extends beyond visible baryonic matter (Bolton et al., 2008)

B2.2.2 – Weak lensing:

In weak lensing, the density of the lens lies below a critical value where multiple images are no longer formed. Weak lensing tangentially shears background sources around foreground lensing objects. The degree of deformation is dependent on the foreground objects gravitational potential. Since the effect is weak, statistical analysis of the distortion of background galaxies around a foreground object is required (Bartelmann & Schneider, 2001). A study of faint galaxies utilising the William Herschel Telescope found evidence consistent with the dark matter hypothesis (Bacon et al., 2000). Galaxy-galaxy lensing data from the Canada-France-Hawaii Telescope Survey was used to determine the likely existence and shape of dark matter halos (Parker et al., 2007). Lastly, the use of the Hubble Space Telescope Cosmic Evolution images to develop gravitational potential contour maps is particularly striking since the centre of the contours is generally not over the centre of visible mass (Massey et al., 2007, p. 287).

B2.2.3 – Microlensing:

Microlensing occurs when the amount of displacement of light around a small gravitational potential cannot be resolved. The effect from microlensing is detected as a transient brightening of the combined signal from the source and lens as two objects pass in front of one another. As will be discussed, microlensing has been particularly effective at quantifying the potential contribution of Massive Compact Halo Objects to DM (Tisserand et al., 2007).

B2.3 – Galaxy and cluster collisions:

Galaxy and cluster collisions provide a unique test of the DM hypothesis. Baryonic material is subject to ram pressure during collisions. However, proposed models require DM to have a small cross-section for self-interaction and interaction with baryonic material. Thus gravitational lensing can be used in a merger to map the distribution of mass to test whether DM has become decoupled from baryonic material. An upper limit to self-interaction cross section can also be derived from merger studies (Kahlhoefer et al., 2014).

The ‘Bullet Cluster’, 1E0657-56, is an often-cited merger used as evidence for DM. Observations have found a DM ‘lump’ lying ahead of the baryonic material. DM in the Bullet cluster has been found to be non-fluid like, with an upper order of magnitude limit on DM collisional cross section of less than $1 \text{ cm}^2\text{g}^{-1}$ (Markevitch et al., 2004). Weak lensing observations of the cluster mergers 1E0657-558 ($z = 0.296$) (Clowe et al., 2006) and J0916.2+2951 ($Z = 0.53$) (Dawson et al., 2012) have also shown the decoupling of dark and baryonic matter. Finally, a study combining data from 72 major and minor mergers concluded the existence of DM was at a 7.6 standard deviation significance (Harvey et al., 2015).

B2.4 – Cosmic microwave background (CMB) and the Lyman-alpha forest constrain parameters of Λ CDM:

Around 400,000 years after the big bang, the universe had cooled enough to allow the recombination of electrons and protons. At this point, photons were able to decouple from ionised matter and travel freely through space. Due to the expansion of the universe, the photons from this time have red shifted and are observed today as the CMB at a temperature of 2.73 K. Anisotropies in the temperature of the CMB represent inhomogeneities in the early

universe and can be used to constrain cosmological parameters in cosmological models (Hu et al., 1997; Sachs et al., 2007). Similarly, the Lyman-alpha forest can be used to constrain cosmological models and is formed from spectroscopic observations of absorption lines arising from the electromagnetic excitation of neutral hydrogen in distant galaxies (Lee et al., 2014).

Increasingly better resolution observations of the CMB have been made over the last few decades. Initial computer modelling showed Λ CDM was consistent with early observations of the anisotropies in the CMB (de Bernardis et al., 2000). More recent studies using The Microwave Anisotropy Probe (WMAP) (Hinshaw et al., 2013) and the better resolution observations from the Planck Satellite (Ade et al., 2014) correlate well with Λ CDM. Significantly, Lyman-alpha forest studies agree with constraints obtained from WMAP data (Lee et al., 2014). Since the CMB data fits Λ CDM, for which CDM is a vital part, this is seen to provide significant evidence for the existence of CDM.

2.5 – Predicted structure of the universe from Λ CDM N-body simulations:

Since in Λ CDM, CDM is largely unaffected by radiation, small density inhomogeneities in the early universe are proposed to have been maintained by CDM. CDM density inhomogeneities could then act as gravitational potential wells for ordinary matter to gravitationally collapse into once the intensity of radiation in the early universe had sufficiently decreased. N-body simulations utilising Λ CDM generally correlate well with the universe's observed large-scale structure (Schaye et al., 2015; Springel et al., 2006; Vogelsberger et al., 2014).

B3 – Dark matter particle candidates:

The theoretical properties of DM can be inferred from the evidence of its existence outlined in section B2 above. The cross section for DM interaction with baryonic material and self-interaction should be extremely small. DM candidates would be expected to have a neutral charge and be undetectable by interaction with electromagnetic radiation (Bernabei, 2002).

The main DM candidates are assessed below.

B3.1 – The neutrino and the sterile neutrino:

Neutrinos are known to only interact with gravity and the weak force, making them DM candidates. Significantly, neutrinos have been proven to exist (Cowan et al., 1956).

Neutrinos are regarded as hot dark matter (HDM) candidates due to their low mass and long free streaming length. However, HDM is known to prevent the gravitational growth of small-scale structure by streaming out of it (Lesgourgues & Pastor, 2012). Early in the search for a DM particle, it was shown that the coherence length of the neutrino in the early universe was too large to be consistent with the clustering scale of galaxies (White et al., 1983).

Furthermore, it has also been shown that massive galactic halos cannot be composed of neutral leptons at the mass of a neutrino (Tremaine & Gunn, 1979). Thus, neutrino particles cannot form the bulk of DM mass.

Sterile neutrinos are theoretical particles with mass estimates of around 10 keV. Due to their larger mass relative to neutrinos, they have been suggested as a potential DM candidate.

However, no experimental evidence of their existence has been found (Kusenko, 2009; Naumov, 2019; Sharma et al., 2017).

B3.2 – Massive astrophysical compact halo objects (MACHOs):

Suggested MACHO's include neutron stars, black holes, brown dwarfs, or un-associated planets. Big Bang Nucleosynthesis (BBN) constrains baryons to $\sim 5\%$ of critical density (Iocco et al., 2009), which, excluding primordial black holes (discussed below), limits the potential mass contribution to DM from MACHOs. Microlensing has been particularly effective in showing galactic DM is not dominated by MACHOs. One study found MACHOs likely constituted 20% of the galactic DM halo (Alcock et al., 2000), whilst another study suggested MACHOs accounted for less than 8% of the galactic DM halo (Tisserand et al., 2007). Combining these observational studies with BBN provides strong evidence that MACHOs are not the primary DM constituent.

3.3 – Primordial black holes (PBHs):

PBHs were first suggested by Hawking (1971). Crucially, PBHs are not constrained by BBN since they are proposed to have formed in the radiation dominated era (Carr et al., 2016). Also, PBHs are subject to less robust constraints on their mass ranges when compared to other MACHOs and hence are considered here separately. However, even with these considerations, if PBHs exist, they are not likely to be the substantive component of DM since studies have shown the abundance of compact objects larger than ~ 0.01 solar masses to be constrained to less than 37.7% of the matter of the universe (Zumalacárregui & Seljak, 2018).

B3.4 – Weakly interacting massive particles (WIMPs):

WIMPs are theoretical stable and neutral particles outside the standard model of particle physics which could have masses of up to $\sim 9 \times 10^{29}$ eV. Generally, WIMPs are predicted to

have ‘frozen out’ of equilibrium with thermal plasma in the early universe when the temperature of the plasma dropped below the WIMPs mass (Gelmini & Gondolo, 2010).

WIMPs provide a potential source of DM.

WIMPs are predicted in supersymmetric particle models. Briefly, supersymmetry models postulate the existence of a supersymmetric partner for each particle in the standard particle model. Each partner pair would differ by a $\frac{1}{2}$ spin which means baryons would be paired with fermions and vice versa. The neutralino is one possible WIMP derived from supersymmetric theories (Jungman et al., 1996).

Another possible WIMP is the axion. Axions were proposed as a solution to the strong CP problem in quantum chromodynamics. The strong CP problem relates the unknown reason as to why quantum chromodynamics preserves charge-conjugation parity symmetry (Peccei & Quinn, 1977). Axions have been proposed as a CDM candidate (Preskill et al., 1983).

B3.4.1 – Experimental attempts to find WIMPs:

Search efforts for a DM candidate is currently focused on WIMPs. Experiments looking for WIMPs consist of three main types:

1. Production of particles in particle accelerators. Following formation, indirect detection of the particles may be made by observing ‘missing’ energy and momentum.
2. Direct detection which focuses on observations of particles scattering off a material.
3. Indirect detection which focuses on DM self-annihilations at locations where there is expected to be a high DM density.

(Giusarma et al., 2014; Undagoitia & Rauch, 2016).

B3.5 – Super heavy particles:

‘Superheavy’ particles have been theorised to form during inflation of the universe and in theory could be a constituent of DM. It has also been proposed that cosmic rays above the Greisen-Zatsepin-Kuzmin cut-off could be produced by decays of these superheavy particles (Kuzmin & Tkachev, 1998). However, no evidence of events above the Greisen-Zatsepin-Kuzmin cut-off have been found.

B4 – Challenges to Λ CDM:

The introduction to paper 2 in this dissertation has already described some challenges to Λ CDM. Other unresolved issues in Λ CDM include:

- The cosmological fine-tuning problem: The cosmological constant as predicted by Λ CDM is many magnitudes higher than observed values (Weinberg, 1989)
- Cosmic coincidence problem: Refers to the unexpected parity of the fractional densities of dark energy and dark matter energy (Sivanandam, 2013).
- There is tension between the 2013 Planck parameter, the Hubble parameter and supernovae 1A data. Furthermore, anomalies in the CMB (e.g. a cold spot and power hemispherical asymmetry) are unexplained (Popolo & Delliou, 2017)
- The angular momentum catastrophe: Simulations suggest dwarf galaxy disks with different angular momentum distributions in dark matter haloes and smaller galactic disk sizes from those observed (Cardone et al., 2009)

- Using observed levels of deuterium as input for BBN results in a three times or greater discrepancy in predicted over observed lithium-7 levels. The observation of trace amounts of lithium-6 is also unexplained (Iocco et al., 2009).

B4.1 – Proposed solutions to issues with Λ CDM:

Self-interacting dark matter (SIDM) has been proposed to solve both the missing satellite and the cuspy halo problems (Spergel & Steinhardt, 2000). However, inferred evidence from astronomical observations has shown DM to have smaller self-interaction cross sections than required for SIDM to account for flat galactic mass profiles (Markevitch et al., 2004).

WIMPs could provide a solution to the tension between the observed levels of element ratios and those predicted in Λ CDM (Iocco et al., 2009). Finally, some of the issues be may due to computational limits. When stars and gas are included in simulations, the predicted distribution of DM on small scales correlates better with observations (Pontzen & Governato, 2014).

B5 – Alternative theories of gravity. Modified Newtonian Dynamics Model (MOND) and its relativistic extension, Tensor-Vector-Scalar gravity (TeVeS):

Many different modified theories of gravity seek to eliminate or minimise the need for DM to explain observational evidence. MOND is an often-cited alternative theory of gravity, first proposed by Milgrom (1983). MOND significantly modifies Newtonian dynamics for very small accelerations, such as those provided in the outer regions of spiral galaxies. MOND assumes the acceleration ‘ a ’ of a particle, at a distance ‘ r ’ from a mass ‘ M ’, satisfies

$$\frac{a^2}{a_0} \approx MGr^{-2}$$

where G is the gravitational constant and a_0 is a constant of the dimensions of acceleration (Milgrom, 1983, p. 365). In particular, MOND modifies Newton's second law $m_g \mathbf{a} = \mathbf{F}$ with,

$$m_g \mu\left(\frac{a}{a_0}\right) \mathbf{a} = \mathbf{F}$$

$$\mu(x \gg 1) \approx 1, \quad \mu(x \ll 1) \approx x$$

where m_g is the gravitational mass of a body moving in a force field \mathbf{F} with acceleration \mathbf{a} , and μ is a function of a ($a=|\mathbf{a}|$) and a_0 . Orthodox Newtonian dynamics is restored when accelerations are much greater than a_0 (Milgrom, 1983, p. 366). MOND is claimed to mostly eliminate the need for DM and it still finds significant support for its explanatory power (Famaey & McGaugh, 2012). However, explaining all astronomical observations, particularly galaxy and cluster mergers, through the filter of MOND is challenging (Clowe et al., 2006). Other direct attacks on the validity of MOND include:

1. The holographic principle within the Λ CDM paradigm accounts for the MOND acceleration (Morgan, 2017)
2. It is argued MOND is equivalent to assuming an isothermal dark matter energy profile, with its density related to the enclosed total baryonic mass (Chan, 2013)

MOND has been extended to a relativistic generalisation, TeVeS (Bekenstein, 2004). Like MOND, TeVeS has significant challenges. It is not possible to simultaneously fit lensing and rotation curve data using the TeVeS model (Mavromatos et al., 2009). Also, TeVeS seems to produce unstable gravitational systems (Seifert, 2007).

B6 – The quantum dark matter (QDM) hypothesis:

Analogous to electrons held in eigenstates by the Coulomb potential in an atom, the QDM hypothesis postulates particles are held in gravitational eigenstates by deep gravitational wells (Ernest, 2001, 2004, 2006, 2009a, 2009b, 2012). Matter in Rydberg states (high n states) have previously been proposed as DM candidates due to their long radiative lifetimes and weak interacting nature (Badiei & Holmlid, 2002). Similarly, as reviewed below, particles held in gravitational eigenstates with high n and l quantum numbers have theoretical DM like properties.

B6.1 – Experimental proof of gravitational eigenstates:

Gravitational eigenstates have been demonstrated using a beam of ultracold neutrons projected above a horizontal mirror in a wedge-shaped gravitational potential. Notably, the reflecting mirror allowed the neutron wave to interfere with itself and create a standing wave. Neutrons were found to fall through quantised energy levels at the peV level (Nesvizhevsky et al., 2003; Nesvizhevsky et al., 2005; Nesvizhevsky et al., 2002). Possibly due to the technical challenges in performing gravitational eigenstate experiments, no other direct evidence of gravitational eigenstates is reported in the literature and there is controversy around whether gravitational eigenstates have been observed (Vankov, 2008). However, the criticisms of Nesvizhevsky and colleagues are argued to be based on a misunderstanding of the difference between classical and quantum behaviours of particles in classic gravitational potentials (Ignatovich, 2011). The experimental proof of the existence of eigenstates deems the development of the theory of gravitational eigenstates necessary whether the QDM hypothesis proves to be correct.

B6.2 – Foundations of QDM mathematical theory:

The mathematical theory relevant to QDM is outlined in detail in paper 1, and briefly again in paper 2. It is not necessary to introduce electrical terms into the Schrodinger equation for weak gravity as it has been shown the electrostatic potential of a typical proton is $\sim 10^{10}$ times smaller than its gravitational potential energy in regions of space considered here (Ernest, 2006, p. 9).

From (2.10) it can be shown the matrix dipole element Π_{if} is the crucial component in determining transition rate. The decrease in the radial component of Π_{if} , as the difference in the initial and final quantum number n becomes large, dominates any increase in angular frequency ω_{if} (Ernest, 2001, pp. 13–17). However, calculation of Π_{if} for high n and l states is problematic and is addressed in the following sections.

Ernest (2001, 2006, 2009a, 2009b) has shown the states of interest have low p values relative to n , and it is advantageous to express the formulae for the gravitational eigenstates in terms of p . Specifically, the value of p determines the spatial oscillatory behaviour of the eigenfunction and the value of p is directly correlated with the number of peaks and the number of zeros in the radial eigenfunction I_R (defined in section B6.3). The number of zeroes in the radial eigenfunction can be used to estimate the radial extent and thus overlap (Ernest, 2009a, 2009b).

B6.3 – The radial equation and its general solution:

From (1.17), the radial equation I_R is

$$I_R \equiv \int_0^\infty R_{n_f, l_f}^*(r) R_{n_i, l_i}(r) r^3 dr \quad (\text{B1}).$$

Ernest (2009a, p. 11) solved (B1) to try and reduce computation times for large quantum eigenvalues,

$$\begin{aligned} I_R &= \frac{2^{2n_i-2p+1} n_i n_f^2 b_0}{(n_i + n_f)^3} \left(\frac{n_i n_f}{(n_i + n_f)^2} \right)^{n_i-p} \\ &\times \left((p-1)! (2n_i - p)! (n_f + p - n_i)! (n_i + n_f - p - 1)! \right)^{1/2} \\ &\times \sum_{k_f=0}^{n_f+p-n_i} \left(\sum_{k_i=0}^{p-1} \left(\frac{(-2n_i)^{k_f} (-2n_f)^{k_i}}{(n_i + n_f)^{k_i+k_f} (p - k_i - 1)! k_i! (n_f + p - n_i - k_f)! k_f!} \right. \right. \\ &\times \left. \left. \frac{(2n_i - 2p + k_i + k_f + 2)!}{(2n_i - 2p + k_f - 1)! (2n_i - 2p + k_i + 1)!} \right) \right) \end{aligned} \quad (\text{B2}).$$

B6.4 – General and approximate solutions for state to state transition categories in figure 2.1

Transition categories for high n , low p states are shown in figure 2.1 in paper 2. General and approximate solutions for each category are presented below.

B6.4.1 – Transition category $\mathbf{B} \rightarrow \mathbf{A}$:

A transition along the $p = 1$ diagonal in figure 2.1 can be obtained by substituting $n_f = n_i - 1$ and $p = 1$ into (B2) to give

$$I_R = 2^{2n_i} b_0 \left(\frac{n_i(n_i - 1)}{(2n_i - 1)^2} \right)^{n_i+1} \sqrt{(2n_i - 1)^3(2n_i - 2)} \quad (\text{B3}).$$

For large n_i , this can be approximated to

$$I_R \approx b_0 n_i^2 \quad (\text{B4}).$$

It can be shown that for any transitions that occur along the same p -diagonal in figure 2.1 (i.e. p remains constant) where $n_f = n_i - 1$ and $l_f = l_i - 1$ the decay rate is $\sim b_0 n_i^2$ provided $n_i \gg p$ (Ernest, 2009a, p. 12).

B6.4.2 – Transition category $C \rightarrow A$:

Transitions like those of $C \rightarrow A$ in figure 1 are found from (B2) as

$$I_R = 2^{2n_i-2} b_0 \left(\frac{n_i(n_i - 2)}{(2n_i - 1)^2} \right)^{n_i+1} \sqrt{(2n_i - 1)^3(2n_i - 2)} \quad (\text{B5}).$$

When $n_i \gg p$, the B5 reduces to

$$I_R \approx \frac{b_0 n_i^{3/2}}{\sqrt{2}} \quad (\text{B6}).$$

Secondary to the shapes of the radial components of the wavefunction being significantly different, the overlap integral is smaller in (B5) relative to (B3), which is reflected in the approximations (B6) and (B4) respectively (Ernest, 2009a, p. 12).

B6.3.3 – Transition category $D \rightarrow A$:

Transitions like $D \rightarrow A$ in figure 2.1 represent the transition from an arbitrary p -turning point Laguerre polynomial state D ($n_i, l_i = n_i - p$) to an arbitrary 1-turning point state A on the left diagonal in figure 2.1 ($n_f = n_i - p, l_f = n_f - 1$). Provided $n_i \gg p$, it can be shown that even when p is substantially greater than 1, (B2) reduces to

$$\begin{aligned}
 I_R \approx & \frac{2^{2n_i-2p+1} n_i n_f^2 b_0}{(n_i + n_f)^3} \left(\frac{n_i n_f}{(n_i + n_f)^2} \right)^{n_i-p} \\
 & \times \left((p-1)! (2n_i - p)! (n_f + p - n_i)! (n_i + n_f - p - 1)! \right)^{\frac{1}{2}} \\
 & \times \sum_{k_i=0}^{p-1} \left(\frac{(2n_i - 2p + k_i + 2)!}{(n_i + n_f)^{k_i} (p - k_i - 1)! (2n_i - 2p + k_i + 1)!} \right. \\
 & \left. \times \frac{(-2n_f)^{k_i}}{k_i! (n_f + p - n_i)! (2n_i - 2p - 1)!} \right) \quad (B6).
 \end{aligned}$$

Equation (B6) can be written as

$$\begin{aligned}
 I_R \approx & \frac{b_0}{2} \sqrt{(p-1)!} \left(\frac{n_i n_f}{(n_i + n_f)^2} \right)^{(n_f+1)} 2^{2n_i-1} \left(\prod_{i=0}^p (n_i + n_f - i)^{\frac{1}{2}} \right) \\
 & \times \left(\sum_{i=1}^p \left((-1)^{i-1} \left(\frac{n_f}{(n_i + n_f)} \right)^i \frac{2^{i-2p+2} (2n_f + i + 1)}{(i-1)! (p-i)!} \right) \right) \quad (B7).
 \end{aligned}$$

If the summation in (B7) is carried out and the product simplified,

$$I_R \approx b_0 \left(\frac{4n_i n_f}{(n_i + n_f)^2} \right)^{(n_f+1)} \frac{p^{p-2} n_i n_f}{(n_i + n_f)^p} \sqrt{\frac{(n_i + n_f)!}{(p-1)! (2n_f - 1)!}} \quad (B8)$$

(Ernest, 2009a, pp. 12–13).

Equation (B8) is effectively approximated by using Stirling's formula,

$$I_R \approx e^{\log\left(\frac{b_0 p^{p/2} n_f^{9/4} (2n_f+2p)^2 (2n_f+p+1)^{p/2+1/4}}{(e^2 \pi p^7)^{1/4} (2n_f+p)^{2+p}}\right) + n_f \log\left(\frac{(2n_f+2p)(2n_f+p+1)}{(2n_f+p)^2}\right)} \quad (\text{B9}).$$

For large values of n_i and p , (B9) can be further estimated using $n_i \approx n_f (= n_i - p)$ and

$\lim_{n \rightarrow \infty} \left(\frac{(2n-p+1)}{2n-2p}\right)^n = e^{((p+1)/2)}$. The radial equation then becomes

$$I_R \approx b_0 n_i \left(\frac{2}{\pi p}\right)^{\frac{1}{4}} \left(\frac{e}{2}\right)^{\frac{p}{2}} \left(\frac{p}{n_i}\right)^{\frac{p-3}{2}} \quad (\text{B10})$$

provided $n_i \gg p \gg 1$ (Ernest, 2009a, p. 13).

In order to test the approximations of (B9) and (B10), Ernest (2009a, pp. 13–14) has compared results for values when (B2) can reasonably be used to calculate the radial integral directly. Equation (B9) performs better than (B10), though as expected the difference in performance decreases as n increases. Notably I_R approaches 0 as p increases, and this effect is greater for higher n states.

B6.5 – The effect of the radial eigenfunction components of the overlap integral on eigenstructure shape:

The width of a $p = 1$ eigenfunction is defined as the full width at zero concavity (FWZC).

Peak centre and FWZC of a $p = 1$ ($R_{n,l=n-1}$) eigenfunction are respectively given by

$$n(n-1)b_0 \sim n^2 b_0 \quad (\text{B11})$$

$$2n\sqrt{n-1} \sim 2n^{3/2}b_0 \quad (\text{B12}).$$

The outcome of (B11) and (B12) is that when two $p = 1$ radial eigenfunctions differ by $\sim n^{1/2}$ or more, the amplitude of one function drops rapidly at the peak position of the other.

Suppose two $p = 1$ eigenfunctions peaks are separated by w FWZCs, the ratio of the amplitude of one wavefunction at the position of the peak of the other, to the amplitude of the peak of the first is given by

$$e^{-2w\sqrt{n_i-1}} \left(\frac{n_i + 2w\sqrt{n_i-1}}{n_i} \right)^{n_i-1} \sim e^{-2w\sqrt{n_i}} \left(1 + \frac{2w}{\sqrt{n_i}} \right)^{n_i-1} \quad (\text{B13}).$$

And the radial dipole overlap I_R is estimated from:

$$I_R \approx b_0 \sqrt{\frac{2(n_i n_f)^{5/2}}{n_i + n_f}} \left(\frac{n_f}{n_i} \right)^{n_i - n_f} \quad (\text{B14})$$

for $n_i, n_f \gg 1$, where n_i and n_f are the initial and final n values (Ernest, 2009b, p. 9).

Equations (B13) and (B14) demonstrate how for large n , the initial and final states can almost completely overlap but due to an extremely low angular frequency, the dipole decay rate $A_{i,f}$ becomes negligible. Furthermore, it has been demonstrated that the interaction between two $p = 1$ states is effectively abolished as w increases (Ernest, 2009b, pp. 9–10). Analysis of $p = 2, 3, 4, \dots$ has similar outcomes except the value of Δn needed to provide distinct separation of states is increased as shown schematically in figure B1 (Ernest, 2009b, p. 11).

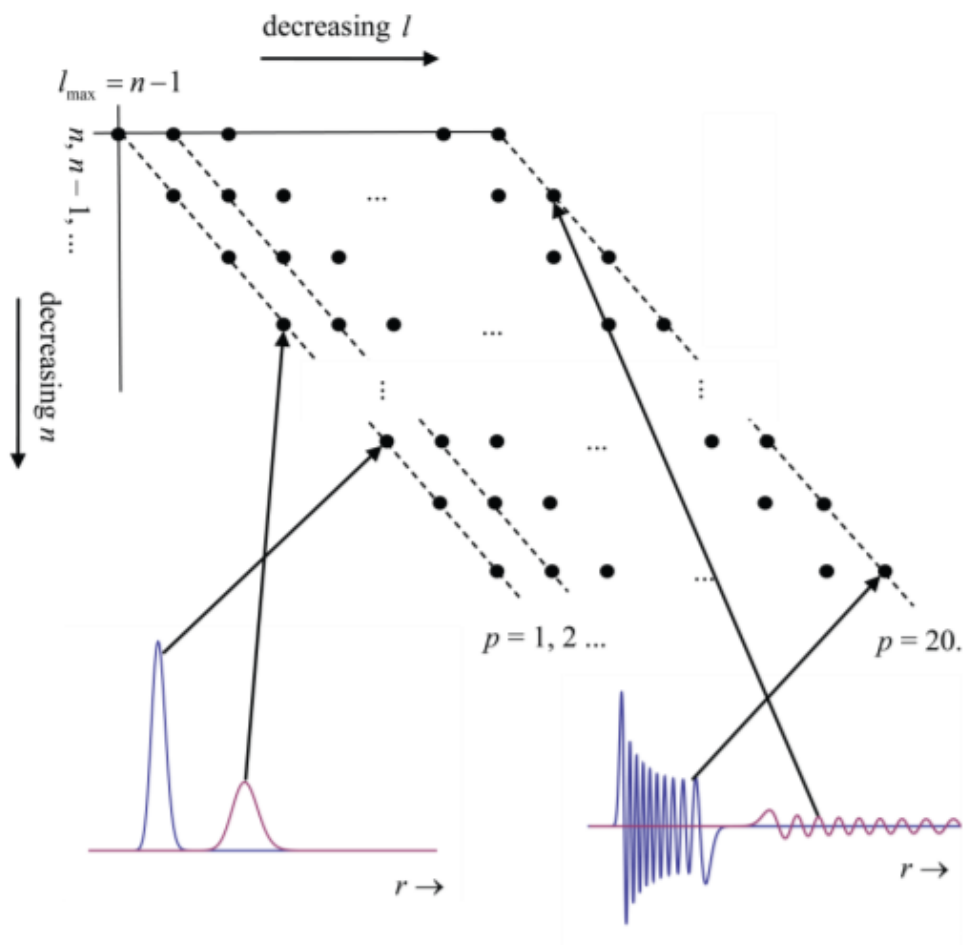


Figure B1. Schematic diagram showing changes in position of high- n , low- p , radial component eigenfunctions with n , and the significance of p in determining the change in n required for radial distinct radial separation of the eigenfunctions (Ernest, 2009b, p. 11).

B6.6 – Overlap integral values and the zeros of the radial eigenfunctions:

When a decay originates from a $p \gg 1$ state such as $D \rightarrow A$ transitions in figure 2.1, there is a high degree of overlap between the states. However, the transition rate remains low since the normalisation condition required by the initial state results in the average amplitude of the initial eigenfunction being small due to increased spread (Ernest, 2009b, p. 16). Another

factor maintaining a low transition rate as shown by Ernest (2009b, p. 16) is the cancellation effect that the oscillatory behaviour of the initial wavefunction has on the radial dipole integral, as shown in the approximate value of the integral formula given below

$$I_R = b_0 \left(\frac{2}{\pi p_i} \right)^{\frac{1}{4}} \left(\frac{e}{2} \right)^{\frac{p_i}{2}} \left(\frac{p_i}{n_i} \right)^{\frac{p_i-3}{2}} \approx 10^{-1 \times 10^{24}} b_0 \quad (\text{B15})$$

when $p_f = 1, n_i \approx 10^{34}, \Delta n = p_i \approx 10^{23}$.

B6.7 – The effect of the angular components of the overlap integral on eigenfunction shape:

The angular integrals of Π_{if} in (1.17) are (Ernest, 2009b, p. 5):

$$I_{\theta\phi x} = \int_0^\pi \int_0^{2\pi} Y_{lf,mf}^* Y_{li,mi} \sin(\theta) \cos(\phi) \sin(\theta) d\phi d\theta \quad (\text{B16})$$

$$I_{\theta\phi y} = \int_0^\pi \int_0^{2\pi} Y_{lf,mf}^* Y_{li,mi} \sin(\theta) \sin(\phi) \sin(\theta) d\phi d\theta \quad (\text{B17})$$

$$I_{\theta\phi z} = \int_0^\pi \int_0^{2\pi} Y_{lf,mf}^* Y_{li,mi} \cos(\theta) \sin(\theta) d\phi d\theta \quad (\text{B18}).$$

Though, the radial components of the interacting eigenfunctions often occupy distinct regions in space, angular components of the overlap integral always overlap. (Ernest & Collins, 2012, p. 243). The general solutions of the angular integrals depend on what value Δm and Δl take in the transition. The method for deriving general solutions for (B16), (B17) and (B18) for initial state $Y_{li,mi} = Y_{l,m}$ and final state $Y_{lf,mf} = Y_{l-l,m}$ is outlined by Ernest (2009a, pp. 8–9).

The discussion of the behaviour of the angular components of the overlap integral is limited here to high n -states. In the azimuthal direction, the probability density is uniform for all

states due to the azimuthal ϕ dependence for all spherical harmonics being of the form $e^{\pm im\phi}$. However, the spherical harmonic polar θ dependence varies with the value of l and m . Here m transitioning is analysed for large l ($l \rightarrow \infty$). It has been shown that when m is close to zero, the probability of the absolute value of m increasing or decreasing is equal. When m is large ($m \sim l$), m transitioning to a larger absolute value is favoured (Ernest, 2009b, p. 8).

Transitions to a larger l results in states with a higher z -component of angular momentum (i.e. more oblate). Transitions to a lower l results in states with a lower z -component of angular momentum (i.e. more spherical). The movement of l is paralleled with a respective movement in the value of n (Ernest, 2009b, p. 8).

B6.8 – Physical properties of gravitational eigenstates and QDM:

A free, well localised particle is a superposition of many eigenstates with non-stationary probability distributions. Gravitational eigenstates are relatively pure with stationary probability distributions and non-localised particles. Like the atomic case, it is reasonable to expect particles bound in eigenstates will have different properties to well localised free particles (Ernest, 2001, 2006).

However, the gravitational eigenstates presented here have unique properties due to the scale of quantum numbers required which leads to closer energy levels than the atomic case. This results in a very small angular frequency ω_{if} (1.16) which reduces the transition probability for radiative dipole decay A_{if} in equation (1.15) when Δn is small. However, when Δn is

large, the radial components of Π_{if} in equation (1.15) become extremely small which again leads to a low A_{if} . Low p states represent the states of most interest since there is a trend to lower transition rates with lower p states (Whinray & Ernest, 2018). By observation of the diagonals in figure 2.1, each increase in p results in an increase in available decay channels (Ernest, 2006, pp. 17–18).

The size of the change in p (i.e. Δp) is important in determining transition rates. The higher the Δp , the more effective the cancellation of the positive and negative regions of the overlap integral $\langle f | er | i \rangle$ in equation (1.15) (Ernest & Collins, 2012, p. 246). Ernest (2009b) showed the increase in spatial oscillation frequencies (SOF) of eigenfunctions is proportional to the square root of the Δp value. This relationship is independent of the interaction potential and the degree of state overlap and is the dominant reason why the radial overlap integral for high n , low p states decreases rapidly with increasing Δp . Due to SOF, high n transitions take place along diagonal lines of approximately constant p (see figure 2.1), and in high n , low p states the only possible transmission is to other low p states (i.e. those with the longest lifetimes) (Ernest, 2009b, pp. 34–35).

Critical to the QDM hypothesis, very high n , low p gravitational eigenstates have radiative lifetimes exceeding the age of the universe (Ernest, 2009a, 2009b). In particular, this is true for eigenstates representative of galactic scale masses and radial spreads (Ernest, 2006, p. 16). Crucial to DM properties, the interaction of the QDM halo with the CMB, stray galactic radiation, particles or elastic and inelastic scattering from photons is extremely small (Ernest, 2006, pp. 19–24).

Whilst QDM does not exclude the possibility of exotic particles, the lifetimes and interactions of gravitational eigenstates are independent of the inherent nature of a particle. This means DM can be made of ordinary matter. Whilst atomic hydrogen could be part of the DM halo, the lack of evidence for the attenuation of electromagnetic radiation matching the excitation of hydrogen suggests QDM would likely consist of elementary particles such as electrons and protons (Ernest, 2001, p. 22).

From the interactions and eigenstate lifetimes discussed here, a QDM matter halo would require a restriction on the n and p values to fulfill the properties required by DM. This limits the number of eigenstates and thus mass which could be held by the eigenstructure. However, despite these restrictions, sufficient eigenstates still exist to accommodate the mass of the DM galactic halo (Ernest, 2001, p. 28, 2006, pp. 12–13).

B6.9 – Speculated formation of the DM halo and Big Bang Nucleosynthesis (BBN):

The development of gravitational eigenstructures requires the existence of strong gravitational potential wells early in the history of the universe when the particle density in the region of the well would be high enough and the temperature low enough to allow decay into gravitational eigenstates (Ernest, 2009a, p. 15). Primordial black holes have been speculated to act as seed potentials in the formation of DM halo eigenstructures (Ernest, 2006, p. 27). Due to the preferential migration of eigenstates, low p states with their long radiative lifetimes and low interaction properties would ultimately be populated (Ernest, 2009a, p. 15).

BBN limits the amount of ordinary matter that can be accounted for after recombination and its results are constrained by observations in the CMB. Since the eigenstructures may have formed prior to recombination, BBN elemental abundances may not be significantly affected (Ernest, 2006, p. 31, 2004). However, the details of BBN need to be formally modelled using the limitations imposed by the QDM hypothesis.

B6.10 – Observations which support or refute the QDM hypothesis:

Theoretical eigenstates require empirical observations. Observation of any DM is difficult due to its inherent invisible nature. However, current and potential observations exist which may help support or refute the existence of QDM.

QDM is expected to have extremely long lifetimes so observations of gravitational eigenstate decay is expected to be infrequent. Ultrahigh energy cosmic rays (UHECRs) are defined by energies around or greater than 10^{19} eV and the origin of these rays is currently unknown (Watson et al., 2011). The decay of gravitational eigenstates has been speculated to be a possible source of UHECRs (Ernest, 2001, 2006, p. 35).

The relative interaction of QDM with particles is expected to be greater than with photons. Consequently, low p states may be transferred up to more visible interacting p states. Observed energies of hot ionised gas in the X-ray region of the galactic halo agree with theoretical halo eigenstate particles pushed to a higher p state (Ernest & Collins, 2012, p. 247).

Many other potential observations have been speculated as providing or could possibly provide evidence of QDM. Detection of enhanced radiation in the CMB at longer wavelengths than currently measured is one possible indicator of QDM. QDM speculated formation of the galactic eigenstructure suggests finding significant deviation from spherical DM halos would likely refute the QDM hypothesis, though the evolution scenario is theoretically incomplete. Finally, different BBN elemental ratios in smaller isolated galaxies may be significantly different due to the possibility the galaxy took longer to form (Ernest, 2006, p. 36).

B6.11 – Identified gaps in the theoretical framework for QDM:

In addition to gaps identified in papers 1 and 2, a well-developed galaxy and universe formation model which has been theoretically evaluated using computer simulations is absent. The outcomes of such computer simulations would allow evaluation of BBN elemental abundances and the anisotropies of the CMB. This is especially important in supporting the DM halo being composed primarily of baryonic matter.

B7 – Conclusion:

The observational evidence outlined in section B2 clearly illustrates a discrepancy between the quantity of observed gravitating matter and its gravitational effects. The two main competing explanations of these observations is DM and alternative theories of gravity. The mass of DM which can be accounted for from known particles and MACHOs is inadequate. Extensive efforts to find a theoretical exotic particle which could account for the substantive portion of DM have been unsuccessful, though experiments continue. Alternative theories of gravity face many difficulties in explaining all observed phenomena. The lack of direct

observational evidence for a DM particle, significant challenges to Λ CDM and the unresolved challenges faced by alternative theories of gravity invites the generation of alternative hypotheses and models.

QDM has the potential to account for the observed evidence in section B2. The extreme quantum numbers associated with deep gravity wells results in unique properties of gravitational eigenstates. Gravitational eigenstates with high n and low p quantum numbers have low interaction cross sections and are extremely stable with lifetimes exceeding that of the universe. The QDM hypothesis does not require the existence of any theoretical particles or the modification of established theories. Gravitational eigenstate theory and its postulated product QDM requires further development to fully investigate the trends in interaction cross sections and lifetimes for different quantum number scenarios. The QDM hypothesis also needs significant quantitative investigation into its potential role in the evolution of the universe and how it may affect BBN. However, given the experimental proof of the existence of gravitational eigenstates and the lack of any currently known limitation of the application of quantum physics to macroscopic states, continued development of the QDM hypothesis is warranted.

Appendix C: Extended Methods for paper 1

This section extends the methods for paper 1 provided in section 1.3.

C1 – Additional justification of choice of methods and data analysis:

Quantum states of particles in gravitational wells were predicted by the Schrödinger equation applied to gravity and then validated by the discovery of quantum eigenstates (Nesvizhevsky et al., 2003; Nesvizhevsky et al., 2005; Nesvizhevsky et al., 2002). Hence the methods in paper 1 follow this precedent and others (Ernest, 2009a, 2009b; Whinray & Ernest, 2018) by producing data for a series of state to state transitions utilising the Schrödinger equation for weak gravity. This data is then plotted to assess for any empirical trend which can be expressed as a mathematical relationship. Since the data produced is not subject to random interference, the statistical investigations applied in experimental fields are not usually relevant (e.g. confidence intervals, standard deviation etc). However, when looking at state lifetimes, it was found that the variation in state lifetimes had an approximate normal random distribution. Hence in the case of state lifetimes, standard deviation was used to indicate error.

C2 – Development of computer programs:

Appendix E, F, G and H contain the Mathematica programs used in paper 1. The programs in appendix E and appendix F were previously developed by Whinray (2013) and only minor modifications were made. The programs in appendix G and appendix H were heavily modified from Whinray (2013) to allow the calculation of state to state transition rates and state lifetimes for all Δm decay channels. After modification, program output was compared

against known values for a particular state to state transition rate or state lifetimes (depending on program) to check validity of calculations.

C3 – Exact values and computer programs/packages used for each state to state transition rate calculated in section 1.4.1:

This section required the use of the Mathematica program contained in appendix G which in turn used the Mathematica package contained in appendix E. Evaluated state to state transition rates in section 1.4.1 are represented by {initial state} to {final state} as shown below:

$$\{n_i, l_i, m_i\} \rightarrow \{n_f, l_f, m_f\}$$

C3.1 – State to State Decay Rates for $\Delta p = -5$:

- i. $\Delta p = -5$; $\Delta l = 1$; $p_i = 6$, $\Delta m = -1, 0, 1$:

$$\{150, 144, m_i\} \rightarrow \{146, 145, m_i - 1\}, m_i = -144, -138, -132, \dots, 132, 138, 144$$

$$\{150, 144, m_i\} \rightarrow \{146, 145, m_i\}, m_i = -144, -138, -132, \dots, 132, 138, 144$$

$$\{150, 144, m_i\} \rightarrow \{146, 145, m_i + 1\}, m_i = -144, -138, -132, \dots, 132, 138, 144$$

- ii. $\Delta p = -5$; $\Delta l = -1$; $p_i = 6$, $\Delta m = -1, 0, 1$:

$$\{150, 144, m_i\} \rightarrow \{144, 143, m_i - 1\}, m_i = -138, -132, 126, \dots, 126, 132, 138$$

$$\{150, 144, m_i\} \rightarrow \{144, 143, m_i\}, m_i = -138, -132, 126, \dots, 126, 132, 138$$

$$\{150, 144, m_i\} \rightarrow \{144, 143, m_i + 1\}, m_i = -138, -132, 126, \dots, 126, 132, 138$$

iii. $\Delta p = -5; \Delta l = 1; p_i = 120, \Delta m = -1, 0, 1$:

$$\{150, 30, m_i\} \rightarrow \{146, 31, m_i - 1\}, m_i = -30, -29, -28, \dots, 28, 29, 30$$

$$\{150, 30, m_i\} \rightarrow \{146, 31, m_i\}, m_i = -30, -29, -28, \dots, 28, 29, 30$$

$$\{150, 30, m_i\} \rightarrow \{146, 31, m_i + 1\}, m_i = -30, -29, -28, \dots, 28, 29, 30$$

iv. $\Delta p = -5; \Delta l = -1; p_i = 6, \Delta m = -1, 0, 1$:

$$\{150, 30, m_i\} \rightarrow \{144, 29, m_i - 1\}, m_i = -30, -29, -28, \dots, 28, 29, 30$$

$$\{150, 30, m_i\} \rightarrow \{144, 29, m_i\}, m_i = -30, -29, -28, \dots, 28, 29, 30$$

$$\{150, 30, m_i\} \rightarrow \{144, 29, m_i + 1\}, m_i = -30, -29, -28, \dots, 28, 29, 30$$

C3.2 – State to State Decay Rates for $\Delta p = -2$:

i. $\Delta p = -2; \Delta l = 1; p_i = 6, \Delta m = -1, 0, 1$:

$$\{150, 144, m_i\} \rightarrow \{149, 145, m_i - 1\}, m_i = -144, -138, -132, \dots, 132, 138, 144$$

$$\{150, 144, m_i\} \rightarrow \{149, 145, m_i\}, m_i = -144, -138, -132, \dots, 132, 138, 144$$

$$\{150, 144, m_i\} \rightarrow \{149, 145, m_i + 1\}, m_i = -144, -138, -132, \dots, 132, 138, 144$$

ii. $\Delta p = -2; \Delta l = -1; p_i = 6, \Delta m = -1, 0, 1:$

$$\{150, 144, m_i\} \rightarrow \{147, 143, m_i - 1\}, m_i = -144, -138, -132, \dots, 132, 138, 144$$

$$\{150, 144, m_i\} \rightarrow \{147, 143, m_i\}, m_i = -144, -138, -132, \dots, 132, 138, 144$$

$$\{150, 144, m_i\} \rightarrow \{147, 143, m_i + 1\}, m_i = -144, -138, -132, \dots, 132, 138, 144$$

iii. $\Delta p = -2; \Delta l = 1; p_i = 120, \Delta m = -1, 0, 1:$

$$\{150, 30, m_i\} \rightarrow \{149, 31, m_i - 1\}, m_i = -30, -29, -28, \dots, 28, 29, 30$$

$$\{150, 30, m_i\} \rightarrow \{149, 31, m_i\}, m_i = -30, -29, -28, \dots, 28, 29, 30$$

$$\{150, 30, m_i\} \rightarrow \{149, 31, m_i + 1\}, m_i = -30, -29, -28, \dots, 28, 29, 30$$

iv. $\Delta p = -2; \Delta l = -1; p_i = 6, \Delta m = -1, 0, 1:$

$$\{150, 30, m_i\} \rightarrow \{147, 29, m_i - 1\}, m_i = -30, -29, -28, \dots, 28, 29, 30$$

$$\{150, 30, m_i\} \rightarrow \{147, 29, m_i\}, m_i = -30, -29, -28, \dots, 28, 29, 30$$

$$\{150, 30, m_i\} \rightarrow \{147, 29, m_i + 1\}, m_i = -30, -29, -28, \dots, 28, 29, 30$$

C3.3 – State to State Decay Rates for $\Delta p = 0$:

i. $\Delta p = 0$; $\Delta l = -1$; $p_i = 6$, $\Delta m = -1, 0, 1$:

$$\{150, 144, m_i\} \rightarrow \{149, 143, m_i - 1\}, m_i = -144, -138, -132, \dots, 132, 138, 144$$

$$\{150, 144, m_i\} \rightarrow \{149, 143, m_i\}, m_i = -144, -138, -132, \dots, 132, 138, 144$$

$$\{150, 144, m_i\} \rightarrow \{149, 143, m_i + 1\}, m_i = -144, -138, -132, \dots, 132, 138, 144$$

v. $\Delta p = 0$; $\Delta l = -1$; $p_i = 6$, $\Delta m = -1, 0, 1$:

$$\{150, 30, m_i\} \rightarrow \{149, 29, m_i - 1\}, m_i = -30, -29, -28, \dots, 28, 29, 30$$

$$\{150, 30, m_i\} \rightarrow \{149, 29, m_i\}, m_i = -30, -29, -28, \dots, 28, 29, 30$$

$$\{150, 30, m_i\} \rightarrow \{149, 29, m_i + 1\}, m_i = -30, -29, -28, \dots, 28, 29, 30$$

C4 – Exact values and computer programs/packages used for each state to state transition rate calculated in section 1.4.2:

This section required the use of the Mathematica program found in appendix F which in turn used the Mathematica package contained in appendix E. Evaluated state to state transition rates in section 1.4.2 are represented by {initial state} to {final state} as shown below:

C4.1 – State to State Decay Rates for $\Delta p = -2$:

i. $\Delta p = -2$; $\Delta l = 1$; $\Delta m = -1, 0, 1$:

$$\{n_i, l_i, 0\} \rightarrow \{n_i - 1, l_i + 1, -1\}, n_i = 5, 10, 15, \dots, 100; l_i = n_i - 3, n_i - 4, n_i - 5, \dots, 0$$

$$\{n_i, l_i, 0\} \rightarrow \{n_i - 1, l_i + 1, 0\}, n_i = 5, 10, 15, \dots, 100; l_i = n_i - 3, n_i - 4, n_i - 5, \dots, 0$$

$$\{n_i, l_i, 0\} \rightarrow \{n_i - 1, l_i + 1, 1\}, n_i = 5, 10, 15, \dots, 100; l_i = n_i - 3, n_i - 4, n_i - 5, \dots, 0$$

ii. $\Delta p = -2$; $\Delta l = -1$; $\Delta m = -1, 0, 1$:

$$\{n_i, l_i, 0\} \rightarrow \{n_i - 3, l_i - 1, -1\}, n_i = 5, 10, 15, \dots, 100; l_i = n_i - 3, n_i - 4, n_i - 5, \dots, 1$$

$$\{n_i, l_i, 0\} \rightarrow \{n_i - 3, l_i - 1, 0\}, n_i = 5, 10, 15, \dots, 100; l_i = n_i - 3, n_i - 4, n_i - 5, \dots, 1$$

$$\{n_i, l_i, 0\} \rightarrow \{n_i - 3, l_i - 1, 1\}, n_i = 5, 10, 15, \dots, 100; l_i = n_i - 3, n_i - 4, n_i - 5, \dots, 1$$

C4.2 – State to State Decay Rates for $\Delta p = -1$:

i. $\Delta p = -1$; $\Delta l = -1$; $\Delta m = -1, 0, 1$:

$$\{n_i, l_i, 0\} \rightarrow \{n_i - 2, l_i - 1, -1\}, n_i = 5, 10, 15, \dots, 100; l_i = n_i - 2, n_i - 3, n_i - 4, \dots, 2$$

$$\{n_i, l_i, 0\} \rightarrow \{n_i - 2, l_i - 1, 0\}, n_i = 5, 10, 15, \dots, 100; l_i = n_i - 2, n_i - 3, n_i - 4, \dots, 2$$

$$\{n_i, l_i, 0\} \rightarrow \{n_i - 2, l_i - 1, 1\}, n_i = 5, 10, 15, \dots, 100; l_i = n_i - 2, n_i - 3, n_i - 4, \dots, 2$$

C4.3 – State to State Decay Rates for $\Delta p = 0$:

i. $\Delta p = 0; \Delta l = -1; \Delta m = -1, 0, 1$:

$$\{n_i, l_i, 0\} \rightarrow \{n_i - 1, l_i - 1, -1\}, n_i = 5, 10, 15, \dots, 100; l_i = n_i - 1, n_i - 2, n_i - 3, \dots, 2$$

$$\{n_i, l_i, 0\} \rightarrow \{n_i - 1, l_i - 1, 0\}, n_i = 5, 10, 15, \dots, 100; l_i = n_i - 1, n_i - 2, n_i - 3, \dots, 2$$

$$\{n_i, l_i, 0\} \rightarrow \{n_i - 1, l_i - 1, 1\}, n_i = 5, 10, 15, \dots, 100; l_i = n_i - 1, n_i - 2, n_i - 3, \dots, 2$$

C5 – Computer programs used for the evaluation of state lifetimes in section 1.3.7:

This section required the use of the Mathematica program found in appendix H which in turn used the Mathematica package contained in appendix E.

Appendix D: Extended Methods for paper 2

D1 – Additional justification of choice of methods and data analysis:

Please see appendix C1 since the argument to support the use of the Schrödinger equation applied to gravity is directly relevant to paper 2. Data produced in paper 2 is non-random due to the theoretical nature of this study; hence the usual methods of statistical analysis are irrelevant. The state to state transition rate was plotted as a function of central mass as the behaviour of gravitational eigenstates relative to central mass directly addresses the research question. Log-log plots of state to state transition rate as a function of central mass were used since they best demonstrated a relationship which could be extrapolated to higher central masses.

D2 – Development of computer programs:

Appendix I and J contain the Mathematica programs/packages used in paper 2. The Mathematica package in appendix I was developed from a previous package developed by Whinray (2013) (appendix E). In particular, the Mathematica package in appendix I can accept central mass as a variable. The program contained appendix J is a completely new program which uses the Mathematica package in appendix I to calculate state to state transition rates for gravitational eigenstates with different central masses. Following initial development, known state to state transition rates for a given set of values was compared against the values produced by the program in appendix J to check validity of calculations.

D3 – Exact values and computer programs/packages used for each state to state transition rate calculated in section 2.3.3:

This section required the use of the Mathematica program contained in appendix I which in turn used the Mathematica package contained in appendix J. The following subsections outline the evaluated transitions in detail. In all cases below, the transitions are represented by {initial state} to {final state} as shown below:

$$\{n_i, l_i, m_i\} \rightarrow \{n_f, l_f, m_f\}.$$

D3.1 – State to State Decay Rates for $p_i = 3$:

The following state to state decay rates were evaluated:

- ii. Binding energy = 172 eV; $\Delta p = -2$; $\Delta l = 1$; $\Delta m = -1, 0, 1$:

$$\{n_i, n_i - 3, 0\} \rightarrow \{n_i - 1, n_i - 2, -1\}, n_i = 50, 100, 150, \dots, 1000$$

$$\{n_i, n_i - 3, 0\} \rightarrow \{n_i - 1, n_i - 2, 0\}, n_i = 50, 100, 150, \dots, 1950$$

$$\{n_i, n_i - 3, 0\} \rightarrow \{n_i - 1, n_i - 2, 1\}, n_i = 50, 100, 150, \dots, 1000$$

- iii. Binding energy = 172 eV; $\Delta p = -2$; $\Delta l = -1$; $\Delta m = -1, 0, 1$:

$$\{n_i, n_i - 3, 0\} \rightarrow \{n_i - 3, n_i - 4, -1\}, n_i = 50, 100, 150, \dots, 1000$$

$$\{n_i, n_i - 3, 0\} \rightarrow \{n_i - 3, n_i - 4, 0\}, n_i = 50, 100, 150, \dots, 1950$$

$$\{n_i, n_i - 3, 0\} \rightarrow \{n_i - 3, n_i - 4, 1\}, n_i = 50, 100, 150, \dots, 1000$$

iv. Binding energy = 172 eV; $\Delta p = -1$; $\Delta l = -1$; $\Delta m = -1, 0, 1$:

$$\{n_i, n_i - 3, 0\} \rightarrow \{n_i - 2, n_i - 4, -1\}, n_i = 50, 100, 150, \dots, 1000$$

$$\{n_i, n_i - 3, 0\} \rightarrow \{n_i - 2, n_i - 4, 0\}, n_i = 50, 100, 150, \dots, 1950$$

$$\{n_i, n_i - 3, 0\} \rightarrow \{n_i - 2, n_i - 4, 1\}, n_i = 50, 100, 150, \dots, 1000$$

v. Binding energy = 172 eV; $\Delta p = 0$; $\Delta l = -1$; $\Delta m = -1, 0, 1$:

$$\{n_i, n_i - 3, 0\} \rightarrow \{n_i - 1, n_i - 4, -1\}, n_i = 50, 100, 150, \dots, 1000$$

$$\{n_i, n_i - 3, 0\} \rightarrow \{n_i - 1, n_i - 4, 0\}, n_i = 50, 100, 150, \dots, 1950$$

$$\{n_i, n_i - 3, 0\} \rightarrow \{n_i - 1, n_i - 4, 1\}, n_i = 50, 100, 150, \dots, 1000$$

vi. Binding energy = 344 eV; $\Delta p = -2$; $\Delta l = 1$:

$$\{n_i, n_i - 3, 0\} \rightarrow \{n_i - 1, n_i - 2, 0\}, n_i = 50, 100, 150, \dots, 1950$$

vii. Binding energy = 344 eV; $\Delta p = -2$; $\Delta l = -1$:

$$\{n_i, n_i - 3, 0\} \rightarrow \{n_i - 3, n_i - 4, 0\}, n_i = 50, 100, 150, \dots, 1950$$

viii. Binding energy = 344 eV; $\Delta p = -1$; $\Delta l = -1$:

$$\{n_i, n_i - 3, 0\} \rightarrow \{n_i - 2, n_i - 4, 0\}, n_i = 50, 100, 150, \dots, 1950$$

ix. Binding energy = 344 eV; $\Delta p = 0$; $\Delta l = -1$:

$$\{n_i, n_i - 3, 0\} \rightarrow \{n_i - 1, n_i - 4, 0\}, n_i = 50, 100, 150, \dots, 1950$$

D3.2 – State to State Decay Rates for $p_i = 10$:

The following state to state decay rates were evaluated:

i. Binding energy = 172 eV; $\Delta p = -5$; $\Delta l = 1$; $\Delta m = 0$:

$$\{n_i, n_i - 10, 0\} \rightarrow \{n_i - 4, n_i - 9, 0\}, n_i = 50, 100, 150, \dots, 1950$$

ii. Binding energy = 172 eV; $\Delta p = -5$; $\Delta l = -1$; $\Delta m = 0$:

$$\{n_i, n_i - 10, 0\} \rightarrow \{n_i - 6, n_i - 11, 0\}, n_i = 50, 100, 150, \dots, 1950$$

iii. Binding energy = 172 eV; $\Delta p = -4$; $\Delta l = 1$; $\Delta m = 0$:

$$\{n_i, n_i - 10, 0\} \rightarrow \{n_i - 3, n_i - 9, 0\}, n_i = 50, 100, 150, \dots, 1950$$

iv. Binding energy = 172 eV; $\Delta p = -4$; $\Delta l = -1$; $\Delta m = 0$:

$$\{n_i, n_i - 10, 0\} \rightarrow \{n_i - 5, n_i - 11, 0\}, n_i = 50, 100, 150, \dots, 1950$$

- v. Binding energy = 172 eV; $\Delta p = -3$; $\Delta l = 1$; $\Delta m = 0$:

$$\{n_i, n_i - 10, 0\} \rightarrow \{n_i - 2, n_i - 9, 0\}, n_i = 50, 100, 150, \dots, 1950$$

- vi. Binding energy = 172 eV; $\Delta p = -3$; $\Delta l = -1$; $\Delta m = 0$:

$$\{n_i, n_i - 10, 0\} \rightarrow \{n_i - 4, n_i - 11, 0\}, n_i = 50, 100, 150, \dots, 1950$$

- vii. Binding energy = 172 eV; $\Delta p = -2$; $\Delta l = 1$; $\Delta m = 0$:

$$\{n_i, n_i - 10, 0\} \rightarrow \{n_i - 1, n_i - 9, 0\}, n_i = 50, 100, 150, \dots, 1950$$

- viii. Binding energy = 172 eV; $\Delta p = -2$; $\Delta l = -1$; $\Delta m = 0$:

$$\{n_i, n_i - 10, 0\} \rightarrow \{n_i - 3, n_i - 11, 0\}, n_i = 50, 100, 150, \dots, 1950$$

- ix. Binding energy = 172 eV; $\Delta p = -1$; $\Delta l = -1$; $\Delta m = 0$:

$$\{n_i, n_i - 10, 0\} \rightarrow \{n_i - 2, n_i - 9, 0\}, n_i = 50, 100, 150, \dots, 1950$$

- x. Binding energy = 172 eV; $\Delta p = 0$; $\Delta l = -1$; $\Delta m = 0$:

$$\{n_i, n_i - 10, 0\} \rightarrow \{n_i - 1, n_i - 9, 0\}, n_i = 50, 100, 150, \dots, 1950$$

xi. Binding energy = 344 eV; $\Delta p = -2$; $\Delta l = 1$; $\Delta m = 0$:

$$\{n_i, n_i - 10, 0\} \rightarrow \{n_i - 1, n_i - 9, 0\}, n_i = 50, 100, 150, \dots, 1950$$

xii. Binding energy = 344 eV; $\Delta p = -2$; $\Delta l = -1$; $\Delta m = 0$:

$$\{n_i, n_i - 10, 0\} \rightarrow \{n_i - 3, n_i - 11, 0\}, n_i = 50, 100, 150, \dots, 1950$$

xiii. Binding energy = 344 eV; $\Delta p = -1$; $\Delta l = -1$; $\Delta m = 0$:

$$\{n_i, n_i - 10, 0\} \rightarrow \{n_i - 2, n_i - 9, 0\}, n_i = 50, 100, 150, \dots, 1950$$

xiv. Binding energy = 344 eV; $\Delta p = 0$; $\Delta l = -1$; $\Delta m = 0$:

$$\{n_i, n_i - 10, 0\} \rightarrow \{n_i - 1, n_i - 9, 0\}, n_i = 50, 100, 150, \dots, 1950$$

D3.3 – State to State Decay Rates for $p_i = 25$:

The following state to state decay rates were evaluated:

i. Binding energy = 172 eV; $\Delta p = -5$; $\Delta l = 1$; $\Delta m = 0$:

$$\{n_i, n_i - 25, 0\} \rightarrow \{n_i - 4, n_i - 24, 0\}, n_i = 50, 100, 150, \dots, 1950$$

ii. Binding energy = 172 eV; $\Delta p = -5$; $\Delta l = -1$; $\Delta m = 0$:

$$\{n_i, n_i - 25, 0\} \rightarrow \{n_i - 6, n_i - 26, 0\}, n_i = 50, 100, 150, \dots, 1950$$

iii. Binding energy = 172 eV; $\Delta p = -4$; $\Delta l = 1$; $\Delta m = 0$:

$$\{n_i, n_i - 25, 0\} \rightarrow \{n_i - 3, n_i - 24, 0\}, n_i = 50, 100, 150, \dots, 1950$$

iv. Binding energy = 172 eV; $\Delta p = -4$; $\Delta l = -1$; $\Delta m = 0$:

$$\{n_i, n_i - 25, 0\} \rightarrow \{n_i - 5, n_i - 26, 0\}, n_i = 50, 100, 150, \dots, 1950$$

v. Binding energy = 172 eV; $\Delta p = -3$; $\Delta l = 1$; $\Delta m = 0$:

$$\{n_i, n_i - 25, 0\} \rightarrow \{n_i - 2, n_i - 24, 0\}, n_i = 50, 100, 150, \dots, 1950$$

vi. Binding energy = 172 eV; $\Delta p = -3$; $\Delta l = -1$; $\Delta m = 0$:

$$\{n_i, n_i - 25, 0\} \rightarrow \{n_i - 4, n_i - 26, 0\}, n_i = 50, 100, 150, \dots, 1950$$

vii. Binding energy = 172 eV; $\Delta p = -2$; $\Delta l = 1$; $\Delta m = 0$:

$$\{n_i, n_i - 25, 0\} \rightarrow \{n_i - 1, n_i - 24, 0\}, n_i = 50, 100, 150, \dots, 1950$$

viii. Binding energy = 172 eV; $\Delta p = -2$; $\Delta l = -1$; $\Delta m = 0$:

$$\{n_i, n_i - 25, 0\} \rightarrow \{n_i - 3, n_i - 26, 0\}, n_i = 50, 100, 150, \dots, 1950$$

ix. Binding energy = 172 eV; $\Delta p = -1$; $\Delta l = -1$; $\Delta m = 0$:

$$\{n_i, n_i - 25, 0\} \rightarrow \{n_i - 2, n_i - 26, 0\}, n_i = 50, 100, 150, \dots, 1950$$

x. Binding energy = 172 eV; $\Delta p = 0$; $\Delta l = -1$; $\Delta m = 0$:

$$\{n_i, n_i - 25, 0\} \rightarrow \{n_i - 1, n_i - 26, 0\}, n_i = 50, 100, 150, \dots, 1950$$

D3.4 – State to State Decay Rates for $p_i = 50$:

The following state to state decay rates were evaluated:

i. Binding energy = 172 eV; $\Delta p = -5$; $\Delta l = 1$; $\Delta m = 0$:

$$\{n_i, n_i - 50, 0\} \rightarrow \{n_i - 4, n_i - 49, 0\}, n_i = 100, 150, 200, \dots, 1950$$

ii. Binding energy = 172 eV; $\Delta p = -5$; $\Delta l = -1$; $\Delta m = 0$:

$$\{n_i, n_i - 50, 0\} \rightarrow \{n_i - 6, n_i - 51, 0\}, n_i = 100, 150, 200, \dots, 1950$$

iii. Binding energy = 172 eV; $\Delta p = -4$; $\Delta l = 1$; $\Delta m = 0$:

$$\{n_i, n_i - 50, 0\} \rightarrow \{n_i - 3, n_i - 49, 0\}, n_i = 100, 150, 200, \dots, 1950$$

iv. Binding energy = 172 eV; $\Delta p = -4$; $\Delta l = -1$; $\Delta m = 0$:

$$\{n_i, n_i - 50, 0\} \rightarrow \{n_i - 5, n_i - 51, 0\}, n_i = 100, 150, 200, \dots, 1950$$

v. Binding energy = 172 eV; $\Delta p = -3$; $\Delta l = 1$; $\Delta m = 0$:

$$\{n_i, n_i - 50, 0\} \rightarrow \{n_i - 2, n_i - 49, 0\}, n_i = 100, 150, 200, \dots, 1950$$

vi. Binding energy = 172 eV; $\Delta p = -3$; $\Delta l = -1$; $\Delta m = 0$:

$$\{n_i, n_i - 50, 0\} \rightarrow \{n_i - 4, n_i - 51, 0\}, n_i = 100, 150, 200, \dots, 1950$$

vii. Binding energy = 172 eV; $\Delta p = -2$; $\Delta l = 1$; $\Delta m = 0$:

$$\{n_i, n_i - 50, 0\} \rightarrow \{n_i - 1, n_i - 49, 0\}, n_i = 100, 150, 200, \dots, 1950$$

viii. Binding energy = 172 eV; $\Delta p = -2$; $\Delta l = -1$; $\Delta m = 0$:

$$\{n_i, n_i - 50, 0\} \rightarrow \{n_i - 3, n_i - 51, 0\}, n_i = 100, 150, 200, \dots, 1950$$

ix. Binding energy = 172 eV; $\Delta p = -1$; $\Delta l = -1$; $\Delta m = 0$:

$$\{n_i, n_i - 50, 0\} \rightarrow \{n_i - 2, n_i - 49, 0\}, n_i = 100, 150, 200, \dots, 1950$$

x. Binding energy = 172 eV; $\Delta p = 0$; $\Delta l = -1$; $\Delta m = 0$:

$$\{n_i, n_i - 50, 0\} \rightarrow \{n_i - 1, n_i - 49, 0\}, n_i = 100, 150, 200, \dots, 1950$$

xi. Binding energy = 344 eV; $\Delta p = -2$; $\Delta l = 1$; $\Delta m = 0$:

$$\{n_i, n_i - 50, 0\} \rightarrow \{n_i - 1, n_i - 49, 0\}, n_i = 100, 150, 200, \dots, 1950$$

xii. Binding energy = 344 eV; $\Delta p = -2$; $\Delta l = -1$; $\Delta m = 0$:

$$\{n_i, n_i - 50, 0\} \rightarrow \{n_i - 3, n_i - 51, 0\}, n_i = 100, 150, 200, \dots, 1950$$

xiii. Binding energy = 344 eV; $\Delta p = -1$; $\Delta l = -1$; $\Delta m = 0$:

$$\{n_i, n_i - 50, 0\} \rightarrow \{n_i - 2, n_i - 49, 0\}, n_i = 100, 150, 200, \dots, 1950$$

xiv. Binding energy = 344 eV; $\Delta p = 0$; $\Delta l = -1$; $\Delta m = 0$:

$$\{n_i, n_i - 50, 0\} \rightarrow \{n_i - 1, n_i - 49, 0\}, n_i = 100, 150, 200, \dots, 1950$$

D3.5 – State to State Decay Rates for $p_i = 75$:

The following state to state decay rates were evaluated:

i. Binding energy = 172 eV; $\Delta p = -5$; $\Delta l = 1$; $\Delta m = 0$:

$$\{n_i, n_i - 75, 0\} \rightarrow \{n_i - 4, n_i - 74, 0\}, n_i = 100, 150, 200, \dots, 1950$$

ii. Binding energy = 172 eV; $\Delta p = -5$; $\Delta l = -1$; $\Delta m = 0$:

$$\{n_i, n_i - 75, 0\} \rightarrow \{n_i - 6, n_i - 76, 0\}, n_i = 100, 150, 200, \dots, 1950$$

iii. Binding energy = 172 eV; $\Delta p = -4$; $\Delta l = 1$; $\Delta m = 0$:

$$\{n_i, n_i - 75, 0\} \rightarrow \{n_i - 3, n_i - 74, 0\}, n_i = 100, 150, 200, \dots, 1950$$

iv. Binding energy = 172 eV; $\Delta p = -4$; $\Delta l = -1$; $\Delta m = 0$:

$$\{n_i, n_i - 75, 0\} \rightarrow \{n_i - 5, n_i - 76, 0\}, n_i = 100, 150, 200, \dots, 1950$$

v. Binding energy = 172 eV; $\Delta p = -3$; $\Delta l = 1$; $\Delta m = 0$:

$$\{n_i, n_i - 75, 0\} \rightarrow \{n_i - 2, n_i - 74, 0\}, n_i = 100, 150, 200, \dots, 1950$$

vi. Binding energy = 172 eV; $\Delta p = -3$; $\Delta l = -1$; $\Delta m = 0$:

$$\{n_i, n_i - 75, 0\} \rightarrow \{n_i - 4, n_i - 76, 0\}, n_i = 100, 150, 200, \dots, 1950$$

vii. Binding energy = 172 eV; $\Delta p = -2$; $\Delta l = 1$; $\Delta m = 0$:

$$\{n_i, n_i - 75, 0\} \rightarrow \{n_i - 1, n_i - 74, 0\}, n_i = 100, 150, 200, \dots, 1950$$

viii. Binding energy = 172 eV; $\Delta p = -2$; $\Delta l = -1$; $\Delta m = 0$:

$$\{n_i, n_i - 75, 0\} \rightarrow \{n_i - 3, n_i - 76, 0\}, n_i = 100, 150, 200, \dots, 1950$$

ix. Binding energy = 172 eV; $\Delta p = -1$; $\Delta l = -1$; $\Delta m = 0$:

$$\{n_i, n_i - 75, 0\} \rightarrow \{n_i - 2, n_i - 76, 0\}, n_i = 100, 150, 200, \dots, 1950$$

x. Binding energy = 172 eV; $\Delta p = 0$; $\Delta l = -1$; $\Delta m = 0$:

$$\{n_i, n_i - 75, 0\} \rightarrow \{n_i - 1, n_i - 76, 0\}, n_i = 100, 150, 200, \dots, 1950$$

D3.6 – State to State Decay Rates for $p_i = 100$:

The following state to state decay rates were evaluated:

i. Binding energy = 172 eV; $\Delta p = -5$; $\Delta l = 1$; $\Delta m = 0$:

$$\{n_i, n_i - 100, 0\} \rightarrow \{n_i - 4, n_i - 99, 0\}, n_i = 150, 200, 250, \dots, 1950$$

ii. Binding energy = 172 eV; $\Delta p = -5$; $\Delta l = -1$; $\Delta m = 0$:

$$\{n_i, n_i - 100, 0\} \rightarrow \{n_i - 6, n_i - 101, 0\}, n_i = 150, 200, 250, \dots, 1950$$

iii. Binding energy = 172 eV; $\Delta p = -4$; $\Delta l = 1$; $\Delta m = 0$:

$$\{n_i, n_i - 100, 0\} \rightarrow \{n_i - 3, n_i - 99, 0\}, n_i = 150, 200, 250, \dots, 1950$$

iv. Binding energy = 172 eV; $\Delta p = -4$; $\Delta l = -1$; $\Delta m = 0$:

$$\{n_i, n_i - 100, 0\} \rightarrow \{n_i - 5, n_i - 101, 0\}, n_i = 150, 200, 250, \dots, 1950$$

v. Binding energy = 172 eV; $\Delta p = -3$; $\Delta l = 1$; $\Delta m = 0$:

$$\{n_i, n_i - 100, 0\} \rightarrow \{n_i - 2, n_i - 99, 0\}, n_i = 150, 200, 250, \dots, 1950$$

vi. Binding energy = 172 eV; $\Delta p = -3$; $\Delta l = -1$; $\Delta m = 0$:

$$\{n_i, n_i - 100, 0\} \rightarrow \{n_i - 4, n_i - 101, 0\}, n_i = 150, 200, 250, \dots, 1950$$

vii. Binding energy = 172 eV; $\Delta p = -2$; $\Delta l = 1$; $\Delta m = 0$:

$$\{n_i, n_i - 100, 0\} \rightarrow \{n_i - 1, n_i - 99, 0\}, n_i = 150, 200, 250, \dots, 1950$$

viii. Binding energy = 172 eV; $\Delta p = -2$; $\Delta l = -1$; $\Delta m = 0$:

$$\{n_i, n_i - 100, 0\} \rightarrow \{n_i - 3, n_i - 101, 0\}, n_i = 150, 200, 250, \dots, 1950$$

ix. Binding energy = 172 eV; $\Delta p = -1$; $\Delta l = -1$; $\Delta m = 0$:

$$\{n_i, n_i - 100, 0\} \rightarrow \{n_i - 2, n_i - 99, 0\}, n_i = 150, 200, 250, \dots, 1950$$

x. Binding energy = 172 eV; $\Delta p = 0$; $\Delta l = -1$; $\Delta m = 0$:

$$\{n_i, n_i - 100, 0\} \rightarrow \{n_i - 1, n_i - 99, 0\}, n_i = 150, 200, 250, \dots, 1950$$

xi. Binding energy = 344 eV; $\Delta p = -2$; $\Delta l = 1$; $\Delta m = 0$:

$$\{n_i, n_i - 100, 0\} \rightarrow \{n_i - 1, n_i - 99, 0\}, n_i = 150, 200, 250, \dots, 1950$$

xii. Binding energy = 344 eV; $\Delta p = -2$; $\Delta l = -1$; $\Delta m = 0$:

$$\{n_i, n_i - 100, 0\} \rightarrow \{n_i - 3, n_i - 101, 0\}, n_i = 150, 200, 250, \dots, 1950$$

xiii. Binding energy = 344 eV; $\Delta p = -1$; $\Delta l = -1$; $\Delta m = 0$:

$$\{n_i, n_i - 100, 0\} \rightarrow \{n_i - 2, n_i - 99, 0\}, n_i = 150, 200, 250, \dots, 1950$$

xiv. Binding energy = 344 eV; $\Delta p = 0$; $\Delta l = -1$; $\Delta m = 0$:

$$\{n_i, n_i - 100, 0\} \rightarrow \{n_i - 1, n_i - 99, 0\}, n_i = 150, 200, 250, \dots, 1950$$

Appendix E: Newtonian (Mathematica Package)

This Mathematica package was developed by Whinray (2013) and is reproduced here.

Italic Text:	<i>denotes a comment</i>
Mathematica code:	denotes Mathematica code

Define start of enclosed package

BeginPackage["Newtonian`"]

GravRates calculates the transition rate from initial quantum state $\langle a_i, b_i, c_i \rangle == \langle n, \ell, m \rangle$ to final state $\langle a_f, b_f, c_f \rangle == \langle n, \ell, m \rangle$

If c_i equals c_f i.e. $\Delta m = 0$ only the z component of the overlap integral is evaluated

GravRates[ai_,bi_,ci_,af_,bf_,cf_] :=

Module[{ni0=ai,li0=bi,mi0=ci,nf0=af,lf0=bf,mf0=cf},

Compute radial (rad) and spherical (sph) components which are the same for all Δm & $\Delta \ell$ transitions rules

(rad=RadialInt[ni0,li0,nf0,lf0];

sph=SphericalProd[li0,mi0,lf0,mf0];

"!Allowed" function checks validity of transition and returns false if transition is valid

Which[!Allowed[ni0,li0,mi0,nf0,lf0,mf0], "Invalid Rules",

mi0==mf0,

Compute z component of overlap integral if $\Delta m = 0$

SetPrecision[Power[TEnergy[ni0,nf0],3]*Power[rad*GPZ[sph],2]/IntDem, sigfigs],

(mf0!=mi0),

Compute x & y component of overlap integral if $\Delta m \neq 0$

SetPrecision[Power[TEnergy[ni0,nf0],3]*Power[Sqrt[Power[rad*GPX[sph],2]+Power[rad*GPY[sph],2]],2]/IntDem, sigfigs],

True, "Default"]]);

Begin["Private`"] *Start encapsulation section of package*

Declare Private Functions

Reduced mass function

ReduceMass[a_,b_]:=a*b/(a+b);

Allowed Function tests whether a transition is valid by return true if found to be invalid and false if valid

Allowed[ni_,li_,mi_,nf_,lf_,mf_]:=Module[{ni0=ni,li0=li,mi0=mi,nf0=nf,lf0=lf,mf0=mf},

((ni0!=nf0) && (0<ni0) && (0<nf0) && (li0<ni0) && (lf0<nf0) && (li0>= 0) && (lf0

>= 0)

&& (mi0 <= li0) && (mf0 <= lf0) && (mi0 >= -li0) && (mf0 >= -lf0) &&

(lf0-li0==1 || lf0-li0==-1) && (Abs[mf0-mi0]<= 1));

Energy of bound particle for $n = a$

ELevels[a_]:=EFactor/Power[a, 2];

Transition Energies

TEnergy[a_,b_]:= (ELevels[a]-ELevels[b])/h;

Normalization constant for $n=a$, $\ell=b$

NormznConst[a_,b_]:=Sqrt[Power[(2/(a*b0)), 3]*(a-b-1)!/(2a*Power[(a+b)!, 3])];

Normalization of radial component for $n=a$, $\ell=b$

**Rad[a_,b_]:=NormznConst[a,b]*Exp[-r/(a*b0)]*Power[2r/(a*b0),
b]*(a+b)!*LaguerreL[a-b-1, 2b+1, 2r/(a*b0)]**

Integration of radial component where $n_i=ai$; $\ell_i=bi$; $n_f=af$; $\ell_f=bf$

**RadialInt[ai_,bi_,af_,bf_]:=Integrate[echarge*Conjugate[Rad[ai,bi]]*Rad[af,bf]*Power
[r,3], {r, 0, Infinity}];**

Spherical inner product where $\ell_i=bi$; $m_i=ci$; $\ell_f=bf$; $m_f>=cf$

**SphericalProd[bi_,ci_,bf_,cf_]:=Conjugate[SphericalHarmonicY[bi,ci,θ,φ]]*SphericalH
armonicY[bf,cf, θ,φ]**

X, Y, Z Spherical Product Integrals

GPX[prodX_]:=Integrate[prodX*Power[Sin[θ], 2]*Cos[φ], {φ, 0, 2Pi}, { θ, 0, Pi}]

GPY[prodY_]:=Abs[Integrate[prodY*Power[Sin[θ],2]*Sin[φ], { φ, 0, 2Pi}, { θ, 0, Pi}]]

GPZ[prodZ_]:=Integrate[prodZ*Sine[θ]*Cos[θ], { φ, 0, 2Pi}, { θ, 0, Pi}]

Declare Constants

Number of significant figures

sigfigs=400;

Electron mass in kilograms

(*ElectronMass=SetPrecision[9.10938188*10^-31, sigfigs];*)

Proton mass in kilograms

ProtonMass=SetPrecision[1.67262158*10⁻²⁷, sigfigs];

Central Mass

CentralMass=SetPrecision[6.4*10⁹, sigfigs];

Universal Gravitational constant in m³kg⁻¹s⁻²

G=SetPrecision[6.67398*10⁻¹¹, sigfigs];

h bar in Js

h=SetPrecision[1.05457148*10⁻³⁴, sigfigs];

Speed of Light (c) in ms⁻¹

c=SetPrecision[299792458, sigfigs];

Electron charge in C

echarge=SetPrecision[1.60217657*10⁻¹⁹, sigfigs];

Permittivity of space in Fm⁻¹

ε0=SetPrecision[8.854187817620*10⁻¹², sigfigs];

Assign Variables

Central mass M in kg

M=CentralMass;

m=ProtonMass;

Reduced mass: Evaluate as a constant and avoid recalculating it

rmass=ReduceMass[m, M];

$a0 = \text{Bohr radius}$

(*a0=SetPrecision[5.2917721092*10^-11, sigfigs];*)

b0 parameter: This parameter arises from Netwonian potential

b0=SetPrecision[Power[h, 2]/(G*rmass*m*M), sigfigs];

Energy level's constant factor

EFactor=SetPrecision[-(rmass*Power[G*m*M/h, 2])/2, sigfigs];

Overlap integral denominator constant factor

IntDem=SetPrecision[3*ε0*Pi*h*Power[c, 3], sigfigs];

End[] *End of private encapsulated section*

EndPackage[] *End of package*

Appendix F: Mathematica program for methods in section 1.3.6

This program contained minor modifications of the program originally developed by Whinray (2013). This program generates data output for a series of state to state transitions as a function of p for a given set of quantum eigenvalues. Output from this program is written to a text file in the form $\{n_f, l_f, m_f, \text{state to state transition rate}\}$.

Italic Text:	<i>denotes a comment</i>
Mathematica code:	denotes Mathematica code

Specify file path

```
fname="C:\\University\\Honours\\Formal delta m  
experiments\\Finalisation\\Transition15.txt";
```

Open file in append mode

```
file = OpenAppend[fname];
```

Import relevant package

```
Needs["Newtonian`"]
```

FnA generates sets of principle quantum numbers in increments of five to compute various transitions of the relevant form of Δp

```
FnA[sets_:1]:=(nvalue=Table[i*5, {i, sets}]; Map[FkB, nvalue];)
```

FkB generates a series of n_i, l_i, n_f, l_f quantum eigenvalues according to value of Δp . Range is manually modified as required for each series of transitions. $lis = lfs - 1$ is used for $\Delta l = -1$, and is manually replaced with $lis = lfs + 1$ for $\Delta l = 1$

```
FkB[n_]:= (niv=n; nvf= niv-2; lfs=Range[nvf-1, 1, -1]; len=Length[lfs]; lis=lfs-
```

```
1; nis=ConstantArray[niv, len]; nfs=ConstantArray[nvf, len]; ms=ConstantArray[0, len];
```

```
MapThread[FnC, {nis, lis, nfs, lfs}];)
```


FnC passes relevant quantum eigenvalues to the Newtonian package which returns state to state transition rate. The relevant quantum eigenvalues state to state transition rate are then written to the text file. m^ and m^+ were manually modified according to what m_i and Δm was being assessed.*

FnC[ni_,li_,nf_,lf_] := Write[file, {ni, li, m*, nf, lf, m+, GravRates[ni,li,m*,nf,lf,m+]}

Call FnA function for a run of up to $n_i = 100$.

Timing[FnA[20]]

Close file

Close[fname]

C:\University\Honours\Formal delta m experiments\Finalisation\Transition14.txt

Appendix G: Mathematica program for methods in section 1.3.5

This program contains major modifications of the program originally developed by Whinray (2013). Unlike the program in appendix F which generates data for state to state transitions as a function of p_i , this program generates data output for a series of state to state transitions as a function of m_i and Δm for a given set of quantum eigenvalues. Output from this program is written to a text file in the form $\{n_f, l_f, m_f, \text{state to state transition rate}\}$.

Italic Text:	<i>denotes a comment</i>
Mathematica code:	denotes Mathematica code

Specify file path

fname="C:\\University\\Honours\\Formal delta m experiments\\Finalisation\\DeltaM5.txt";

Open file in append mode

file = OpenAppend[fname];

Import relevant package

Needs["Newtonian`"]

FnA generates sets of principle quantum numbers in increments of five to compute various transitions for the relevant Δm decay channel

FnA[sets_:1]:=(mvalue=Table[i*6, {i, -sets,sets}]; Map[FnB, mvalue];)

FnB generates a series of m_i and m_f quantum eigenvalues according to value of Δm .

FnB[m_]:= (miv=m; mfv = Range[miv-1, miv+1, 1];

len = Length[mfv];

mis = ConstantArray[miv,len];

```
mfs = mfv;MapThread[FnC, {mis,mfs}];)(* Write[file,results];*)
```

FnC passes relevant quantum eigenvalues to the Newtonian package which returns state to state transition rate. The relevant quantum eigenvalues state to state transition rate are then written to the text file. n^ , l^* , n^+ and n^* were manually modified according to what l_i was being assessed.*

```
FnC[mi_, mf_] := Write[file, {n*, l*, mi, n+, l+, mf, GravRates[n*, l*, mi, n+, l+, mf]}]
```

Call FnA function for a run of $m_i = -144, -138, -132, \dots, 132, 238, 144$.

```
Timing[FnA[24]]
```

Close file

```
Close[fname]
```

C:\University\Honours\Formal delta m experiments\Finalisation\DeltaM2.txt

Appendix H: Mathematica program for methods in section 1.3.7

The basis for this program was originally developed by Whinray (2013) and underwent extensive modification to calculate the lifetimes of a state for all Δm decay channels.

Previously, this program only considered the $\Delta m = 0$ decay channel when calculating state lifetimes.

Italic Text:	<i>denotes a comment</i>
Mathematica code:	denotes Mathematica code

Specify file path

**fname="C:\\University\\Honours\\Formal delta m experiments\\Finalisation\\lifetimes
for n 110 to 200.txt"**

Open file in append mode

file=OpenAppend[fname];

Import relevant package

Needs["Newtonian`"]

Check validity of state to state transition – returns true if valid

Truth[_,_,,x_,y_,z_]:=x>y&& y>=z;

Calculate lifetime of state $\{n_i, l_i, m_i\}$

InitSate[ni_,li_,mi_] := (nfs=Range[li, ni-1]; lfs={li-1,li+1}; mfs = Range[-1,1];

trups=Tuples[{{ni}, {li},{mi}, nfs, lfs,mfs}];

tot=Total[Decays@ @ @Extract[trups,Position[Truth@ @ @trups, True]]];

Write initial state eigenvalues and state lifetime to file

Write[file,{ni,li,mi,1/tot}]

Function decays calculate decay rate of a state.

Decays[qni_,qli_,qmi_,qnf_,qlf_,qmf_]:=GravRates[qni,qli,qmi,qnf,qlf,qmf];

Call InitState function to perform calculations for initial quantum eigenvalues which are manually entered

Timing[InitSate@ @ @{{120,80,0},{120,85,0},{120,90,0}}]

Close file

Close[file];

Appendix I: NewtonianModified (Mathematica package)

The basis for this Mathematica was developed by Whinray (2013) and is contained in appendix E. This Mathematica package was substantially modified to be able to accept central mass as a variable when the function GravRates was called by the program in Appendix J.

Italic Text:	<i>denotes a comment</i>
Mathematica code:	denotes Mathematica code

Define start of enclosed package

BeginPackage["NewtonianVariableMass`"]

GravRates calculates the transition rate from initial quantum state $\langle a_i, b_i, c_i \rangle == \langle n, \ell, m \rangle$ to final state $\langle a_f, b_f, c_f \rangle == \langle n, \ell, m \rangle$ for a given central mass CM

If c_i equals c_f i.e. $\Delta m = 0$ only the z component of the overlap integral is evaluated

GravRates[ai_,bi_,ci_,af_,bf_,cf_,CM_] :=

Module[{ni0=ai,li0=bi,mi0=ci,nf0=af,lf0=bf,mf0=cf,M0=CM},

Compute radial (rad) and spherical (sph) components which are the same for all Δm & $\Delta \ell$ transitions rules

(rad=RadialInt[ni0,li0,nf0,lf0,M0]; sph=SphericalProd[li0,mi0,lf0,mf0];

“!Allowed” function checks validity of transition and returns false if transition is valid

Which[!Allowed[ni0,li0,mi0,nf0,lf0,mf0], "Invalid Rules",

mi0==mf0,

Compute z component of overlap integral if $\Delta m = 0$

```
SetPrecision[Power[TEnergy[ni0,nf0,M0],3]*Power[rad*GPZ[sph],2]/IntDem, sigfigs],  
  (mf0!=mi0),
```

Compute x & y component of overlap integral if $\Delta m \neq 0$

```
SetPrecision[Power[TEnergy[ni0,nf0,M0],3]*Power[Sqrt[Power[rad*GPX[sph],2]+Power[rad*GPY[sph],2]],2]/IntDem, sigfigs],  
  True, "Default")]);
```

Start encapsulation section of package

```
Begin["Private`"]
```

Declare Private Functions

Reduced Mass

```
ReduceMass[a_,b_]:=a*b/(a+b);
```

Allowed Function tests whether a transition is valid by return true if found to be invalid and false if valid

```
Allowed[ni_,li_,mi_,nf_,lf_,mf_]:=Module[{ni0=ni,li0=li,mi0=mi,nf0=nf,lf0=lf,mf0=mf},  
  ((ni0!=nf0) && (0<ni0) && (0<nf0) && (li0<ni0) && (lf0<nf0) && (li0>= 0) && (lf0  
>= 0)  
  && (mi0 <= li0) && (mf0 <= lf0) && (mi0 >= -li0) && (mf0 >= -lf0) &&  
  (lf0-li0==1 || lf0-li0== -1) && (Abs[mf0-mi0]<= 1))];
```

Energy of bound particle for $n = a$

```
ELevels[a_,M_]:=EFactor[M]/Power[a, 2];
```

Transition Energies

```
TEnergy[a_,b_,M_]:=(ELevels[a,M]-ELevels[b,M])/ħ;
```

Normalization constant for $n=a$, $\ell=b$

NormznConst[a_,b_,M_]:=Sqrt[Power[(2/(a*b0[M])), 3]*(a-b-1)/(2a*Power[(a+b)!, 3])];

Normalization of radial component for $n=a$, $\ell=b$

Rad[a_,b_,M_]:=NormznConst[a,b,M]*Exp[-r/(a*b0[M])]*Power[2r/(a*b0[M]), b]*(a+b)!*LaguerreL[a-b-1, 2b+1, 2r/(a*b0[M])]

Integration of radial component where $n_i=a_i$; $\ell_i=b_i$; $n_f=a_f$; $\ell_f=b_f$

RadialInt[ai_,bi_,af_,bf_,M_]:=Integrate[echarge*Conjugate[Rad[ai,bi,M]]*Rad[af,bf, M]*Power[r,3], {r, 0, Infinity}];

Spherical inner product where $\ell_i=b_i$; $m_i=c_i$; $\ell_f=b_f$; $m_f>=c_f$

SphericalProd[bi_,ci_,bf_,cf_]:=Conjugate[SphericalHarmonicY[bi,ci,0, φ]]*SphericalHarmonicY[bf,cf,0, φ]

X, Y, Z Spherical Product Integrals

GPX[prodX_]:=Abs[Integrate[prodX*Power[Sin[0], 2]*Cos[φ], { φ , 0, 2Pi}, {0, 0, Pi}]]

GPY[prodY_]:=Abs[Integrate[prodY*Power[Sin[0],2]*Sin[φ], { φ , 0, 2Pi}, {0, 0, Pi}]]

GPZ[prodZ_]:=Abs[Integrate[prodZ*Sine[0]*Cos[0], { φ , 0, 2Pi}, {0, 0, Pi}]]

Reduced mass

rmass[M_]:=SetPrecision[ReduceMass[m, M],400]

b0 parameter

b0[M_]:=SetPrecision[Power[\hbar , 2]/(G*rmass[M]*m*M), 400];

Energy level's constant factor

EFactor[M_]:=SetPrecision[-(rmass[M]*Power[G*m*M/ \hbar , 2])/2, 400];

Declare Constants

Number of significant figures

sigfigs=400;

Electron mass in kg

(*ElectronMass=SetPrecision[9.10938188*10⁻³¹, sigfigs];*)

Proton mass in kilograms

ProtonMass=SetPrecision[1.67262158*10⁻²⁷, sigfigs];

Universal Gravitational constant in m³kg⁻¹s⁻²

G=SetPrecision[6.67398*10⁻¹¹, sigfigs];

h bar in Js

ħ=SetPrecision[1.05457148*10⁻³⁴, sigfigs];

Speed of Light (c) in ms⁻¹

c=SetPrecision[299792458, sigfigs];

Electron charge in C

echarge=SetPrecision[1.60217657*10⁻¹⁹, sigfigs];

Permittivity of space in Fm⁻¹

ε0=SetPrecision[8.854187817620*10⁻¹², sigfigs];

Assign Variables

Proton mass

m=ProtonMass;

Overlap integral denominator constant factor

IntDem=SetPrecision[3*ε0*Pi*ħ*Power[c, 3], sigfigs];

End private encapsulated section

End[]

End of package

EndPackage[]

Appendix J: Mathematica program for methods in section 2.3.3

This program calculates state to state transition rate as a function of central mass.

Italic Text:	<i>denotes a comment</i>
Mathematica code:	denotes Mathematica code

Specify file path

**fname="C:\\University\\Honours\\Deacy rates scaling with central mass\\Data and
analysis\\CentralMass18.txt";**

Open file in append mode

file = OpenAppend[fname];

Import relevant package

Needs["NewtonianVariableMass`"]

The niValues function maps a set of values of n_i to the centralMass function.

niValues[n_]:= (ni = Table[i, {i,50,n,50}]; Map[centralMass,ni];)

The centralMass function calculates required central mass for a given n level and binding energy PLUS checks whether relativistic regions of gravity are avoided by calling the checkRelativity function. If the gravitational eigenstate is found to lie within a relativistic region of gravity, "Failed relativity assumption" is returned

**centralMass[n_] := (SetPrecision[mass=((2*bindEn* \hbar^2 *n^2)/(μ *G^2*m^2))^(1/2),
prec];Which[checkRelativity[n,mass]=True,
main[n,mass],checkRelativity[n,mass]=False, "Failed relativity assumption"])**

The checkRelativity function checks average radius of an eigenstate is > 1000 radius of Schwarchild Radius for a given central mass

checkRelativity [n_,M_]:= (n^2*ħ^2/(μ*G*M*m))>(1000*(2*G*M)/(c^2))

The main function calls the GravRates function in the NewtonianModified Package which then return the state to state transition rate. Initial and final quantum eigenvalues are then written to the text file along with the relevant state to state decay rate

main[ni_,mass_]:=Write[file, {ni, ni-50,0, ni-3, ni-51,0,mass, GravRates[ni,ni-50,0,ni-3,ni-51,0,mass]]]

Set variables

Set precision

prec = 1000;

Mass of charged particle, proton in kg

m = SetPrecision[1.67262158*10^(-27),prec];

Gravitational constant

G = SetPrecision[6.67398*10^-11, prec];

Binding energy – was manually altered for evaluation of different binding energies

bindEn = SetPrecision[2.76*10^-17,prec];

h bar value

ħ = SetPrecision[1.05457148*10^-34,prec];

Reduced mass

μ = SetPrecision[1.67262158*10^-27,prec];

Boltzman constant

k = SetPrecision[1.38064852*10^-23,prec];

Speed of light

c = SetPrecision[2.99792458*10^8,prec];

Call niValues to start calculation up to relevant n_i . Here, the final n_i is 1950. Can manually change for higher or larger values of n_i

Timing[niValues[1950]]

Close file

Close[fname]

Appendix K: Examples of python code used for data analysis

Italic Text:	<i>denotes a comment</i>
Mathematica code:	denotes Mathematica code

K1 – Importation of data from text file

Use the decimal class to be able to handle arbitrary precision. Import decimal from Decimal module

from decimal import Decimal

Function parse_number breaks up data types from text file (produced from Mathematica programs)

def parse_number(number):

Test for integer and return value if integer

try:

return int(number)

except ValueError:

pass

Remove precision definitions and whitespaces from Mathematica output. Return cleaned data

try:

return Decimal(number.replace("`100.", "").replace("`400.", "").replace('*^', 'e'))

except ValueError:

pass

Raise exception if unknown number format within text file

raise ValueError("Unknown number format: " + number)

Function read_clean_data parses the test file into a list of lists

def read_clean_data(filename):

```
data = []
```

Open file in read mode

```
text = f.read()
```

Remove all line continuations (backslash-newline)

```
text = text.replace('\\n', '')
```

Split text at curly braces – if data isn't contained in curly braces, raise exception

```
if text[0] != '{' or text[-2:] != '}\n':
```

```
    raise ValueError("Data is not wrapped in curly braces")
```

```
text = text[1:-2]
```

Join data which is split over multiple lines and then split data in braces separated by a comma

```
for brace in text.split('}\n{'):
```

```
    brace = ''.join(brace.splitlines())
```

```
    numbers = brace.split(',')
```

Parse all the numbers

```
numbers = [parse_number(number) for number in numbers]
```

Append to data variable as a list of lists

```
data.append(numbers)
```

```
return data
```

Call function to import data

```
data = read_clean_data("DeltaM8.txt")
```

K2 – Sample code for results in section 1.4.1

Import relevant sections of modules

```
from pylab import plot, show, xlabel, ylabel, scatter, yscale, legend, rc, title
```

Create empty list

```
mi_q_mneg1_m0_m1 = []
```

Loop over data to extract relevant information and store in nested list

```
for num in range(-30,30,1): change range to fit text file
```

Create empty list then append data

```
line = []
```

```
line.append(num)
```

```
line.append(31-abs(num)) replace integer with relevant pi value
```

```
for row in data:
```

```
    if row[2] == num:
```

```
        line.append(row[6])
```

```
mi_q_mneg1_m0_m1.append(line)
```

Create empty lists

```
mi = []
```

```
q = []
```

```
mneg1 = []
```

```
m0 = []
```

```
m1 = []
```

```
tot_decay = []
```

```
avg_decay = []
```

```
m0_vs_total = []
```

```
m_0x3 = []
```

```
q_div_l = []
```

```
mi_div_qi = []
```

Loop over nested list with relevant data and create lists for later plots

```
for row in mi_q_mneg1_m0_m1:
    mi.append(row[0])
    q.append(row[1])
    mneg1.append(row[2])
    m0.append(row[3])
    m1.append(row[4])
    tot_decay.append(row[2]+row[3]+row[4])
    avg_decay.append((row[2]+row[3]+row[4])/3)
    m0_vs_total.append((row[2]+row[3]+row[4]-3*row[3])/(row[2]+row[3]+row[4])*100)
    m_0x3.append(3*row[3])
    q_div_l.append(row[1]/97)
```

Create plot

```
plot(q,mneg1, label='$\Delta\$\it{m}\$ = -1 or 1', color = 'magenta')
plot(q,m0, label='$\Delta\$\it{m}\$ = 0')
plot(q,m1, color = 'magenta')
plot(q,tot_decay, label = 'Sum total for all $\Delta\$\it{m}\$')
plot(q, m_0x3, label = 'Estimated sum total using only $\Delta\$\it{m}\$ = 0')
```

Set x and y labels

```
xlabel('$\it{q_i}\$ ($\Equiv\$\it{l_i}\$ - |\it{m_i}\$|)')
ylabel('State to state transition rate ($s^{-1}\$)')
```

Position legend box

```
legend(bbox_to_anchor = (1, 0.5), loc = 'center left')
```

Title graph

```
title('$\it{n_i}\$ = 150, $\it{l_i}\$ = 30, $\Delta\$\it{l}\$ = -1, $\it{p_i}\$ = 120,
$\Delta\$\it{p}\$ = -2')
```

Use show to end plotting on same graph

```
show()
```


K3 – Sample code for results in section 1.4.2

Import relevant sections from pylab module

```
from pylab import plot,show,xlabel,ylabel,scatter,yscale,legend, xscale, subplot, yticks,
xticks,title
```

Plot state to state transition rate for $\Delta m = 0$

```
for num in range(5,105,5):
```

Create empty lists

```
ni = []
```

```
pi = []
```

```
rate_m0 = []
```

Append values from data file containing state transition rates for $\Delta m = 0$

```
for row in data_0:
```

```
    if row[0] == num:
```

```
        pi.append(row[0]-row[1])
```

```
        rate_m0.append(row[6])
```

Plot state to state transition rate as a function of p_i

```
plot(pi,rate_m0, label = num)
```

Set y-axis to log scale

```
yscale('log')
```

Set x and y labels

```
ylabel('State to state transition rate  $(s^{-1})$ ')
```

```
xlabel(''$\it{p_i}$')
```

Title graph

```
title(''$\Delta$\it{p}$ = -2, $\Delta$\it{m}$ = 0, $\Delta$\it{l}$ = 1')
```

Set legend box to right side of graph

```
legend(bbox_to_anchor = (1, 0.5), loc = 'center left', ncol=4, title = 'Initial principle
quantum number '$\it{n_i}$')
```

```
show()
```

Plot state to state transition rate for $\Delta m = -1/1$

for num in range(5,105,5):

Create empty lists

ni = []

pi = []

rate_m1 = []

Append values from data file containing state transition rates for $\Delta m = \pm 1$

for row in data_1:

if row[0] == num:

pi.append(row[0]-row[1])

rate_m1.append(row[6])

Plot state to state transition rate as a function of p_i

plot(pi,rate_m1, label = num)

Set y axis scale to logarithmic

yscale('log')

Set x and y labels

ylabel('State to state transition rate (s^{-1}) ')

xlabel('' p_i '')

Title graph

title('' $\Delta p = -2, \Delta m = \pm 1, \Delta l = 1$ '')

Set location of legend

legend(bbox_to_anchor = (1, 0.5), loc = 'center left', ncol=4, title = 'Initial principle quantum number n_i '')

Use show function to end plotting on graph

show()

Plot difference between decay rates for $\Delta m = 0$ and $\Delta m = \pm 1$

Start index counter

r = 0

Add decay rate from data_0 to data_1 to allow comparison of decay rates

for row in data_0:

row.append(data_1[r][6])

r += 1

Plot difference in state to state decay rate between decay channels $\Delta m = 0$ and $\Delta m = \pm 1$

for num in range(5,105,5):

ni = []

pi = []

difference = []

Append relevant data to empty lists

for row in data_0:

if row[0] == num:

pi.append(row[0]-row[1])

difference.append(row[6]-row[7])

Plot difference between state to state decay rate for different Δm decay channels as a function of p_i

plot(pi,difference, label = num)

Set y axis scale to logarithmic

yscale('log')

Label x and y axis

ylabel('Difference in state to state transtion rate (s^{-1}) ')

xlabel(' p_i ')

Title graph

title(' $\Delta p = -2$, $\Delta l = 1$ ')

Set location of legend

legend(bbox_to_anchor = (1, 0.5), loc = 'center left', ncol=4, title = 'Initial principle quantum number n_i ')

Use show function to end plotting of graph

show()

Plot percentage of decay rate for $\Delta m = \pm 1$ over decay rate for $\Delta m = 0$

for num in range(5,105,5):

Create empty lists

ni = []

pi = []

percentage_difference = []

Append relevant data to empty lists

for row in data_0:

if row[0] == num:

pi.append(row[0]-row[1])

percentage_difference.append(row[6]/row[7]*100)

Plot percentage difference between state to state transition rate for different Δm decay channels and a function of p_i

plot(pi,percentage_difference, label = num)

Label x and y axis

ylabel('Percentage (%)')

xlabel('\$\it{p_i}\$')

Title graph

title('\$\Delta\it{p} = -2, \Delta\it{l} = 1\$')

Set location of legend

legend(bbox_to_anchor = (1, 0.5), loc = 'center left', ncol=4, title = 'Initial principle quantum number \$\it{n_i}\$')

K4 – Sample code for results in section 1.4.3

Plot state lifetimes calculated using all Δm decay channels as a function of p_i

for num in range(15,105,5):

Create empty lists

```
n = []
```

```
l = []
```

```
p = []
```

```
lifetime = []
```

Loop over data for lifetimes of states calculated using all Δm decay channels and append relevant data to empty lists

```
for row in data_mAll:
```

```
    if row[0] == num:
```

```
        n.append(row[0])
```

```
        l.append(row[1])
```

```
        p.append(row[0]-row[1])
```

```
        lifetime.append(row[3])
```

plot state lifetime as a function of l

```
plot(l,lifetime, label= n[0])
```

Make log-log plot by setting x and y axis scales to logarithmic

```
xscale('log')
```

```
yscale('log')
```

Label x and y axis

```
xlabel('$_{l}$')
```

```
ylabel('Lifetime (s)')
```

Title graph

```
title(' (b) Estimate obtained using all  $\Delta m$  channels')
```

Set location of legend

```
legend(title = 'Principle quantum number  $n$ ', ncol = 6, loc = 'lower center',  
bbox_to_anchor=(0.5, -0.5))
```

K5 – Sample code for results in section 2.4

K5.1 – Sample code for state to state transition rate as a function of central mass

Read in all 78 data files. Assign each read in file as a list of lists to the dictionary 'data'

```
data = {}
```

Start index counter

r = 0

for i in range(78):

r += 1

Create file name to open in steps

name = 'CentralMass'

file = 'CentralMass'

name += str(r)

file += str(r)

file += '.txt'

Open and read in relevant file using program in K1

data[name] = read_clean_data(file)

Create empty lists

mass_53 = []

decay_rate_53 = []

Read over relevant data file and append data points to relevant lists

for row in data['CentralMass53']:

mass_53.append(row[6])

decay_rate_53.append(row[7])

Create empty lists

mass_59 = []

decay_rate_59 = []

Read over relevant data file and append data points to relevant lists

for row in data['CentralMass59']:

mass_59.append(row[6])

decay_rate_59.append(row[7])

Create empty lists

mass_55 = []

```
decay_rate_55 = []
```

Read over relevant data file and append data points to relevant lists

```
for row in data['CentralMass55']:
```

```
    mass_55.append(row[6])
```

```
    decay_rate_55.append(row[7])
```

Create empty lists

```
mass_69 = []
```

```
decay_rate_69 = []
```

Read over relevant data file and append data points to relevant lists

```
for row in data['CentralMass69']:
```

```
    mass_69.append(row[6])
```

```
    decay_rate_69.append(row[7])
```

Create empty lists

```
mass_57 = []
```

```
decay_rate_57 = []
```

Read over relevant data file and append data points to relevant lists

```
for row in data['CentralMass57']:
```

```
    mass_57.append(row[6])
```

```
    decay_rate_57.append(row[7])
```

Plot each state to state decay rate for each individual p_i

```
plot(mass_53,decay_rate_53, label='$p_{i}$ = 10')
```

```
plot(mass_59,decay_rate_59, label='$p_{i}$ = 25')
```

```
plot(mass_55,decay_rate_55, label='$p_{i}$ = 50')
```

```
plot(mass_69,decay_rate_69, label='$p_{i}$ = 75')
```

```
plot(mass_57,decay_rate_57, label='$p_{i}$ = 100')
```

Label x and y axis

```
xlabel('Central Mass (kg)')
```

```
ylabel('State to state transition rate ( $s^{-1}$ )')
```

Set scale of x and y axis to logarithmic

```
xscale('log')
```

```
yscale('log')
```

Title graph

```
title('(a) -172 eV,  $\Delta\epsilon_p = -5$ ,  $\Delta\epsilon_l = 1$ )
```

```
legend(loc='center left', bbox_to_anchor=(1,0.5), ncol = 1)
```

Use show to end plotting on graph

```
show()
```

K5.2 – Sample code for gradients as a function of p_i

Import relevant sections of pylab and math modules

```
from pylab import plot, show, scatter, xlabel, ylabel, xscale, yscale, legend, title
```

```
from math import log10
```

Read in all 78 data files. Assign each read in file as a list of lists to the dictionary 'data'

```
data = {}
```

Start index counter

```
r = 0
```

```
for i in range(78):
```

```
    r += 1
```

Create file name to open in steps

```
name = 'CentralMass'
```

```
file = 'CentralMass'
```

```
name += str(r)
```

```
file += str(r)
```

```
file += '.txt'
```

Open and read in relevant file using program in K1

```
data[name] = read_clean_data(file)
```


Create empty list

```
gradientListofListsList = []
```

Extract relevant list of lists for gradient analysis

```
for i in [54, 60,56,70,58]:
```

```
    name = 'CentralMass'
```

```
    name += str(i)
```

Create empty lists

```
    gradient = []
```

```
    mass = []
```

```
    rate = []
```

```
    n = []
```

```
    t = 1
```

```
    pi = data[name][0][0]-data[name][0][1]
```

Define lineLegend variable to use in legend when creating plot

```
    lineLegend = '$\it{p_i}$ = '+ str(pi)
```

Loop of data contained in list of lists and append relevant information to empty lists above

```
    for row in data[name]:
```

```
        if row[0] < 1901:
```

```
            n.append(row[0])
```

```
            mass.append(row[6]/(10**11))
```

```
            rate.append(row[7])
```

```
            rateChange = log10(data[name][t][7])-log10(row[7])
```

```
            massChange = log10(data[name][t][6])-log10(row[6])
```

```
            gradient.append(rateChange/massChange)
```

```
            t += 1
```

Plot gradient as a function of the central mass

```
plot(mass, gradient, label = lineLegend)
```

Set x and y labels

```
xlabel('Mass ($x10^{11}$ kg)')
```

```
ylabel('Gradient')
```

Title graph

title('(c) -172 eV, $\Delta p = -5$, $\Delta l = -1$)

Define location of legend

legend(loc='center left', bbox_to_anchor=(1.5,0.5), ncol = 1)

Use show function to end plotting of graph

show()

Appendix L: References included in sections outside of paper 1 and paper 2

- Ade, P., Aghanim, N., Alves, M., Armitage-Caplan, C., Arnaud, M., Ashdown, M., Atrio-Barandela, F., Aumont, J., Aussel, H., Baccigalupi, C., Banday, A. J., Barreiro, R., Barrena, R., Bartelmann, M., Bartlett, J., Bartolo, N., Basak, S., Battaner, E., Battye, R., ... Zonca, A. (2014). Planck 2013 results. I. Overview of products and scientific results. *Astronomy and Astrophysics*, 571(7). <https://doi.org/10.1051/0004-6361/201321529>
- Alcock, C., Allsman, R., Alves, D., Axelrod, T., Becker, A., Bennett, D., Cook, K., Dalal, N., Drake, A., Freeman, K., Geha, M., Griest, K., Lehner, M., Marshall, S., Minniti, D., Nelson, C., Peterson, B., Popowski, P., Pratt, M., ... Welch, D. (2000). The MACHO project: Microlensing results from 5.7 years of Large Magellanic Cloud observations. *The Astrophysical Journal*, 542(1), 281–307. <https://doi.org/10.1086/309512>
- Badiei, S., & Holmlid, L. (2002). Rydberg matter in space: Low-density condensed dark matter. *Monthly Notices of the Royal Astronomical Society*, 333(2), 360–364. <https://doi.org/10.1046/j.1365-8711.2002.05399.x>
- Bartelmann, M., & Schneider, P. (2001). Weak gravitational lensing. *Physics Reports*, 340(4–5), 291–472. [https://doi.org/10.1016/S0370-1573\(00\)00082-X](https://doi.org/10.1016/S0370-1573(00)00082-X)
- Bacon, D. , Refregier, A., & Ellis, R. (2000). Detection of weak gravitational lensing by large-scale structure. *Monthly Notices of the Royal Astronomical Society*, 318(2), 625–640. <https://doi.org/10.1046/j.1365-8711.2000.03851.x>
- Bekenstein, J. (2004). Relativistic gravitation theory for the modified Newtonian dynamics paradigm. *Physical Review D*, 70(8), 1–34. <https://doi.org/10.1103/PhysRevD.70.083509>

- Bernabei, R. (2002). Dark matter search. *Progress in Particle and Nuclear Physics*, 48(1), 263–282. [https://doi.org/10.1016/S0146-6410\(02\)00132-1](https://doi.org/10.1016/S0146-6410(02)00132-1)
- Bolton, A., Burles, S., Koopmans, L., Treu, T., Gavazzi, R., Moustakas, L., Wayth, R., & Schlegel, D. (2008). The Sloan Lens ACS survey. V. The full ACS strong-lens sample. *The Astrophysical Journal*, 682(2), 964–984. <https://doi.org/10.1086/589327>
- Cardone, V., Popolo, A., & Kroupa, P. (2009). Angular momentum transfer and the size–mass relation in early-type galaxies. *Monthly Notices of the Royal Astronomical Society*, 400(2), 766–774. <https://doi.org/10.1111/j.1365-2966.2009.15450.x>
- Carr, B., Kühnel, F., & Sandstad, M. (2016). Primordial black holes as dark matter. *Physical Review D*, 94(8). <https://doi.org/10.1103/PhysRevD.94.083504>
- Chan, M. (2013). Reconciliation of modified Newtonian dynamics and dark matter theory. *Physical Review D*, 88(10). <https://doi.org/10.1103/PhysRevD.88.103501>
- Clowe, D., Bradac, M., Gonzalez, A., Markevitch, M., Randall, S., Jones, C., & Zaritsky, D. (2006). A direct empirical proof of the existence of dark matter. *The Astrophysical Journal*, 648(2), L109–L113. <https://doi.org/10.1086/508162>
- Cowan, C., Reines, F., Harrison, F., Kruse, H., & McGuire, A. (1956). Detection of the free neutrino: A confirmation. *Science*, 124(3212), 103–104.
- Dawson, W., Wittman, D., Jee, M., Gee, P., Hughes, J., Tyson, J., Schmidt, S., Thorman, P., Bradač, M., Miyazaki, S., Lemaux, B., Utsumi, Y., & Margoniner, V. (2012). Discovery of a dissociative galaxy cluster merger with large physical separation. *The Astrophysical Journal*, 747(2), 1–6. <https://doi.org/10.1088/2041-8205/747/2/L42>
- de Bernardis, P., Ade, P. A. R., Bock, J. J., Bond, J. R., Borrill, J., Boscaleri, A., Coble, K., Crill, B. P., De Gasperis, G., Farese, P. C., Ferreira, P. G., Ganga, K., Giacometti, M.,

- Hivon, E., Hristov, V. V., Iacoangeli, A., Jaffe, A. H., Lange, A. E., Martinis, L., ... Vittorio, N. (2000). A flat Universe from high-resolution maps of the cosmic microwave background radiation. *Nature*, 404(6781), 955–959.
<https://doi.org/10.1038/35010035>
- Ernest, A. (2001). Dark matter and galactic halos—A quantum approach. *arXiv.org*.
<https://arxiv.org/abs/astro-ph/0108319>.
- Ernest, A. (2004). Can quantum theory explain dark matter? *arXiv.org*.
<https://arxiv.org/abs/astro-ph/0310897>
- Ernest, A. (2006). A quantum approach to dark matter. In J. V. Blain (Ed.), *Dark matter: New Research* (4th ed., pp. 91–147). Nova Science Publishers.
- Ernest, A. (2009a). Gravitational eigenstates in weak gravity: I. Dipole decay rates of charged particles. *Journal of Physics A: Mathematical and Theoretical*, 42(11), 1–25.
<https://doi.org/10.1088/1751-8113/42/11/115207>
- Ernest, A. (2009b). Gravitational eigenstates in weak gravity: II. Further approximate methods for decay rates. *Journal of Physics A: Mathematical and Theoretical*, 42(11), 1–36. <https://doi.org/10.1088/1751-8113/42/11/115208>
- Ernest, A. (2012). Gravitational quantisation and dark matter. In I. Cotaescu (Ed.), *Advances in Quantum Theory* (pp. 221–248). IntechOpen. <https://doi.org/10.5772/34922>
- Ernest, A., & Collins, M. (2012). Structural features of high-n gravitational eigenstates. *Gravitation and Cosmology*, 18(4), 242–248.
<https://doi.org/10.1134/S0202289312040056>

- Famaey, B., & McGaugh, S. (2012). Modified Newtonian Dynamics (MOND): Observational phenomenology and relativistic extensions. *Living Reviews in Relativity*, 15(1), 1–159. <https://doi.org/10.12942/lrr-2012-10>
- Gelmini, G., & Gondolo, P. (2010). DM production mechanisms. In G. Bertone (Ed.), *Particle Dark Matter: Observations, Models and Searches* (pp. 121–141). Cambridge University Press.
- Giusarma, E., Lattanzi, M., Melchiorri, A., & Mena, O. (2014). Axion cold dark matter: Status after Planck and BICEP2. *Physical Review D*, 90(4) <https://doi.org/10.1103/PhysRevD.90.043534>
- Harvey, D., Massey, R., Kitching, T., Taylor, A., & Tittley, E. (2015). The nongravitational interactions of dark matter in colliding galaxy clusters. *Science*, 347(6229), 1462–1465. <https://doi.org/10.1126/science.1261381>
- Hawking, S. (1971). Gravitationally collapsed objects of very low mass. *Monthly Notices of The Royal Astronomical Society*, 152(1), 75–78. <https://doi.org/10.1093/mnras/152.1.75>
- Hinshaw, G., Larson, D., Komatsu, E., Spergel, D., Bennett, C., Dunkley, J., Nolte, M., Halpern, M., Hill, R., Odegard, N., Page, L., Smith, K., Weiland, J., Gold, B., Jarosik, N., Kogut, A., Limon, M., Meyer, S., Tucker, G., ... Wright, E. (2013). Nine-year Wilkinson Microwave Anisotropy Probe (WMAP) observations: Cosmological parameter results. *The Astrophysical Journal*, 208(2). <https://doi.org/10.1088/0067-0049/208/2/19>
- Hu, W., Sugiyama, N., & Silk, J. (1997). The physics of microwave background anisotropies. *Nature*, 386(6620), 37–43. <https://doi.org/10.1038/386037a0>

- Ignatovich, V. (2011). Comment On “On observation of neutron quantum states in the Earth’s gravitational field.” *arXiv.org*. <https://arxiv.org/abs/1101.0888>
- Iocco, F., Mangano, G., Miele, G., Pisanti, O., & Serpico, P. (2009). Primordial nucleosynthesis: From precision cosmology to fundamental physics. *Physics Reports*, 472(1), 1–76. <https://doi.org/10.1016/j.physrep.2009.02.002>
- Jungman, G., Kamionkowski, M., & Griest, K. (1996). Supersymmetric dark matter. *Physics Reports*, 267(5), 195–373. [https://doi.org/10.1016/0370-1573\(95\)00058-5](https://doi.org/10.1016/0370-1573(95)00058-5)
- Kahlhoefer, F., Schmidt-Hoberg, K., Frandsen, M., & Sarkar, S. (2014). Colliding clusters and dark matter self-interactions. *Monthly Notices of The Royal Astronomical Society*, 437(3), 2865–2881. <https://doi.org/10.1093/mnras/stt2097>
- Kusenko, A. (2009). Sterile neutrinos: The dark side of the light fermions. *Physics Reports*, 481(1), 1–28. <https://doi.org/10.1016/j.physrep.2009.07.004>
- Kuzmin, V., & Tkachev, I. (1998). Ultrahigh-energy cosmic rays, superheavy long-lived particles, and matter creation after inflation. *Journal of Experimental and Theoretical Physics Letters*, 68(4), 271–275. <https://doi.org/10.1134/1.567858>
- Lee, K., Hennawi, J., Stark, C., Prochaska, J., White, M., Schlegel, D., Eilers, A., Arinyo-i-Prats, A., Suzuki, N., Croft, R., Caputi, K., Cassata, P., Ilbert, O., Garilli, B., Koekemoer, A., Le Brun, V., Le Fèvre, O., Maccagni, D., Nugent, P., ... Zucca, E. (2014). Ly α forest tomography from background galaxies: The first megaparsec-resolution large-scale structure map at $z > 2$. *The Astrophysical Journal Letters*, 795(1). <https://doi.org/10.1088/2041-8205/795/1/L12>
- Lesgourgues, J., & Pastor, S. (2012). Neutrino mass from cosmology. *Advances in High Energy Physics*, 2012. <https://hal.archives-ouvertes.fr/hal-01121776>

- Markevitch, M., Gonzalez, A., Clowe, D., Vikhlinin, A., Forman, W., Jones, C., Murray, S., & Tucker, W. (2004). Direct constraints on the dark matter self-interaction cross section from the merging galaxy cluster 1E 0657-56. *The Astrophysical Journal*, 606(2), 819–824. <https://doi.org/10.1086/383178>
- Massey, R., Rhodes, J., Ellis, R., Scoville, N., Leauthaud, A., Finoguenov, A., Capak, P., Bacon, D., Aussel, H., Kneib, J., Koekemoer, A., McCracken, H., Mobasher, B., Pires, S., Refregier, A., Sasaki, S., Starck, J., Taniguchi, Y., Taylor, A., & Taylor, J. (2007). Dark matter maps reveal cosmic scaffolding. *Nature*, 445(7125), 286–290. <https://doi.org/10.1038/nature05497>
- Mavromatos, N., Sakellariadou, M., & Yusaf, M. (2009). Can the relativistic field theory version of modified Newtonian dynamics avoid dark matter on galactic scales? *Physical Review D*, 79(8). <https://doi.org/10.1103/PhysRevD.79.081301>
- Milgrom, M. (1983). A modification of the Newtonian dynamics as a possible alternative to the hidden mass hypothesis. *The Astrophysical Journal*, 270, 365–370. <https://doi.org/10.1086/161130>
- Mongan, T. R. (2017). MOND is unnecessary. *ArXiv.Org*. <http://arxiv.org/abs/1703.06028>
- Naumov, D. (2019). The sterile neutrino: A short introduction. *EPJ Web Conf.*, 207. <https://doi.org/10.1051/epjconf/201920704004>
- Nesvizhevsky, V., Börner, H., Gagarski, A., Petoukhov, A., Petrov, G., Abele, H., Baebler, S., Divkovic, G., Rueb, F., Stöferle, T., Westphal, A., Strelkov, A., Protasov, K., & Voronin, A. Yu. (2003). Measurement of quantum states of neutrons in the Earth's gravitational field. *Physical Review D*, 67(10), 1–9. <https://doi.org/10.1103/PhysRevD.67.102002>

- Nesvizhevsky, V., Petukhov, A., Börner, H., Baranova, T., Gagarski, A., Petrov, G., Protasov, K., Voronin, A., Baebler, S., Abele, H., Westphal, A., & Lucovac, L. (2005). Investigation of the neutron quantum states in the Earth's gravitational field. *Journal of Research of the National Institute of Standards and Technology*, 110(3), 263–267. <https://doi.org/10.6028/jres.110.036>
- Nesvizhevsky, V., Börner, H., Petukhov, A., Abele, H., Baebler, S., Rueb, F., Stöferle, T., Westphal, A., Gagarski, A., Petrov, G., & Strelkov, A. (2002). Quantum states of neutrons in the Earth's gravitational field. *Nature*, 415(6869), 297–299. <https://doi.org/10.1038/415297a>
- Parker, L., Hoekstra, H., Hudson, M., Waerbeke, L., & Mellier, Y. (2007). The masses and shapes of dark matter halos from galaxy-galaxy lensing in the CFHT legacy survey. *The Astrophysical Journal*, 669(1), 21–31. <https://doi.org/10.1086/521541>
- Peccei, R., & Quinn, H. (1977). CP Conservation in the Presence of Pseudoparticles. *Physical Review Letters*, 38(25), 1440–1443. <https://doi.org/10.1103/PhysRevLett.38.1440>
- Pontzen, A., & Governato, F. (2014). Cold dark matter heats up. *Nature*, 506(7487), 171–178. <https://doi.org/10.1038/nature12953>
- Popolo, A., & Delliou, M. (2017). Small scale problems of the Λ CDM model: A short review. *Galaxies*, 5(1), 1–46. <https://doi.org/10.3390/galaxies5010017>
- Preskill, J., Wise, M., & Wilczek, F. (1983). Cosmology of the invisible axion. *Physics Letters B*, 120(1), 127–132. [https://doi.org/10.1016/0370-2693\(83\)90637-8](https://doi.org/10.1016/0370-2693(83)90637-8)
- Richards, E., van Zee, L., Barnes, K., Staudaher, S., Dale, D., Braun, T., Wavle, D., Calzetti, D., Dalcanton, J., Bullock, J., & Chandar, R. (2015). Baryonic distributions in the

- dark matter halo of NGC 5005. *Monthly Notices of The Royal Astronomical Society*, 449(4), 3981–3996. <https://doi.org/10.1093/mnras/stv568>
- Rubin, V., Ford, W., & Thonnard, N. (1978). Extended rotation curves of high-luminosity spiral galaxies. IV. Systematic dynamical properties, Sa \rightarrow Sc. *The Astrophysical Journal*, 225, L107–L111. <https://doi.org/10.1086/182804>
- Sachs, R., Wolfe, A., Ellis, G., Ehlers, J., & Krasiński, A. (2007). Republication of: Perturbations of a cosmological model and angular variations of the microwave background (By R.K. Sachs and A.M. Wolfe). *General Relativity and Gravitation*, 39(11), 1929–1961. <https://doi.org/10.1007/s10714-007-0448-9>
- Schaye, J., Crain, R., Bower, R., Furlong, M., Schaller, M., Theuns, T., Dalla Vecchia, C., Frenk, C., McCarthy, I., Helly, J., Jenkins, A., Rosas-Guevara, Y., White, S., Baes, M., Booth, C., Camps, P., Navarro, J., Qu, Y., Rahmati, A., ... Trayford, J. (2015). The EAGLE project: Simulating the evolution and assembly of galaxies and their environments. *Monthly Notices of The Royal Astronomical Society*, 446(1), 521–554. <https://doi.org/10.1093/mnras/stu2058>
- Seifert, M. (2007). Stability of spherically symmetric solutions in modified theories of gravity. *Physical Review D*, 76(6). <https://doi.org/10.1103/PhysRevD.76.064002>
- Sharma, G., Chauhan, A., & Chauhan, B. (2017). Dark matter and neutrinos. *ArXiv.Org*. <https://arxiv.org/pdf/1711.10564.pdf>
- Sivanandam, N. (2013). Is the cosmological coincidence a problem? *Physical Review D*, 87(8). <https://doi.org/10.1103/PhysRevD.87.083514>

- Spergel, D., & Steinhardt, P. (2000). Observational evidence for self-interacting cold dark matter. *Physical Review Letters*, 84(17), 3760–3763.
<https://doi.org/10.1103/PhysRevLett.84.3760>
- Springel, V., Frenk, C., & White, S. (2006). The large-scale structure of the Universe. *Nature*, 440(7088), 1137–1144. <https://doi.org/10.1038/nature04805>
- Tisserand, P., Le Guillou, L., Afonso, C., Albert, J., Andersen, J., Ansari, R., Aubourg, É., Bareyre, P., Beaulieu, J., Charlot, X., Coutures, C., Ferlet, R., Fouqué, P., Glicenstein, J., Goldman, B., Gould, A., Graff, D., Gros, M., Haissinski, J., ... EROS-2 Collaboration. (2007). Limits on the MACHO content of the galactic halo from the EROS-2 survey of the Magellanic Clouds. *Astronomy and Astrophysics*, 469(2), 387–404. <https://doi.org/10.1051/0004-6361:20066017>
- Tremaine, S., & Gunn, J. (1979). Dynamical role of light neutral leptons in cosmology. *Physical Review Letters*, 42(6), 407–410. <https://doi.org/10.1103/PhysRevLett.42.407>
- Undagoitia, T., & Rauch, L. (2016). Dark matter direct-detection experiments. *Journal of Physics G: Nuclear and Particle Physics*, 43(1), 1–78. <https://doi.org/10.1088/0954-3899/43/1/013001>
- Vankov, A. (2008). On observation of neutron quantum states in Earth gravitational field at Laue-Langevin Institute, Grenoble. *ArXiv.Org*. <http://arxiv.org/abs/0808.136>
- Vogelsberger, M., Genel, S., Springel, V., Torrey, P., Sijacki, D., Xu, D., Snyder, G., Nelson, D., & Hernquist, L. (2014). Introducing the Illustris Project: Simulating the coevolution of dark and visible matter in the Universe. *Monthly Notices of The Royal Astronomical Society*, 444(2), 1518–1547. <https://doi.org/10.1093/mnras/stu1536>

- Watson, L., Mortlock, D., & Jaffe, A. (2011). A Bayesian analysis of the 27 highest energy cosmic rays detected by the Pierre Auger Observatory. *Monthly Notices of the Royal Astronomical Society*, 418(1), 206–213. <https://doi.org/10.1111/j.1365-2966.2011.19476.x>
- Weinberg, S. (1989). The cosmological constant problem. *Reviews of Modern Physics*, 61(1), 1–23. <https://doi.org/10.1103/RevModPhys.61.1>
- Whinray, T. (2013). *Gravitational Eigenstates, a Baryonic Explanation for the Dark Matter Hypothesis* [Honours Thesis]. Charles Sturt University.
- Whinray, T., & Ernest, A. (2018). Relations between transition rates and quantum numbers in gravitational potentials. *Gravitation and Cosmology*, 24(1), 97–102. <https://doi.org/10.1134/S0202289318010152>
- White, S., Frenk, C., & Davis, M. (1983). Clustering in a neutrino-dominated universe. *Astrophysical Journal*, 274, L1–L5. <https://doi.org/10.1086/184139>
- Yegorova, I., Babic, A., Salucci, P., Spekkens, K., & Pizzella, A. (2011). Rotation curves of luminous spiral galaxies. *Astronomische Nachrichten*, 332(8), 846–853. <https://doi.org/10.1002/asna.201111582>
- Zumalacárregui, M., & Seljak, U. (2018). Limits on stellar-mass compact objects as dark matter from gravitational lensing of type Ia supernovae. *Physical Review Letters*, 121(14). <https://doi.org/10.1103/PhysRevLett.121.141101>
- Zwicky, F. (1937). *On the Masses of Nebulae and of the Clusters of Nebulae*. *Astrophysical Journal*, vol.86, p.217. DOI:10.1086/143864